Karlsruhe Institute of Technology

Annual Report 2021

Institute for Pulsed Power and Microwave Technology

Institut für Hochleistungsimpuls- und Mikrowellentechnik

John Jelonnek (ed)

Annual Report 2021

Institute for Pulsed Power and Microwave Technology
Institut für Hochleistungsimpuls- und Mikrowellentechnik

John Jelonnek (ed)

Part of this work was supported by ITER Organization under the task agreement C52TD53FE. The views and opinions expressed herein reflect only the authors views. The ITER Organization is not liable for any use that may be made of the information contained therein.

Part of this work is supported by Fusion for Energy (F4E) under Grants F4E-GRT-553 and within the European GYrotron Consortium (EGYC). EGYC is a collaboration among SPC, Switzerland; KIT, Germany; HELLAS, Greece; IFP-CNR, Italy. The views expressed in this publication do not necessarily reflect the views of the European Commission.

Part of this work has been carried out within the framework of the EUROfusion Consortium, funded by the European Union via the Euratom Research and Training Programme (Grant Agreement No 101052200 — EUROfusion). Views and opinions expressed are however those of the author(s) only and do not necessarily reflect those of the European Union or the European Commission. Neither the European Union nor the European Commission can be held responsible for them.

Part of the simulations presented in this work have been carried out by using the HELIOS supercomputer at IFERC-CSC.

Impressum

Karlsruher Institut für Technologie (KIT)

KIT – Die Forschungsuniversität in der Helmholtz-Gemeinschaft

Institute for Pulsed Power and Microwave Technology (IHM)

Institut für Hochleistungsimpuls- und Mikrowellentechnik (IHM)

Director: Prof. Dr.-Ing. John Jelonnek

The Institute for Pulsed Power and Microwave Technology (Institut für Hochleistungsimpuls- und Mikrowellentechnik, IHM) is working in the areas of pulsed power and high-power microwave technologies. Both, research and development of high power sources as well as related applications are in the focus. Applications for pulsed power technologies are ranging from materials processing to bioelectrics. High power microwave technologies are focusing on microwave sources (gyrotrons) for electron cyclotron resonance heating of magnetically confined plasmas and on applications for materials processing at microwave frequencies.

IHM is doing research, development, academic education, and, in close collaboration with the KIT division IMA and industrial partners, technology transfer. The R&D focus is on the long-term goals of the Helmholtz Association of German Research Centres (HGF). By begin of 2021, the new program-oriented period of the HGF (POF4) started. During this POF4 period, IHM is continuing its research work in the HGF programs "Nuclear Fusion (FUSION)" and "Nuclear Waste Management, Safety and Radiation Research (NUSAFE)" while the team members that were working in the HGF programs "Energy Efficiency, Materials and Resources (EMR)" and "Renewable Energies (RE)" during POF3 period are now working in the new HGF program "Materials and Technologies for the Energy Transition (MTET)". It includes the new research focus on liquid metals as advanced heat-transfer (HTM) and storage media for CSP and other high temperature technologies. Additionally, the research on industrial microwave processes shifts towards the research field of power-based fuels and chemicals. Here the focus is on microwave plasma chemistry such as CO_2 dissociation and H_2 production respectively by use of atmospheric plasmas sustained by high power microwaves and generated by innovative solid-state power amplifiers. Additionally, in 2021 the highly multidisciplinary Helmholtz IVF project CORAERO (Airborne Transmission of SARS Coronavirus, https://www.coraero.de/) started, which brings together scientists from virus biology, medicine, applied physics, chemistry, and engineering to understand virus spreading through aerosols and designing technical and administrative measures for mitigation and virus control. IHM is involved in the design and investigation of microwave-based concepts for inactivation of coronavirus.

Projects funded by third-parties complement significantly the research work within all the different HGF programs. This report puts a specific focus on those third-party. Considering the pulsed power technology and related applications, that includes the research on e. g. microalgae processing at large-scale relevant for industrial processes, the PEF-assisted extraction of valuable compounds and the development of powerful semiconductor-based marx-type pulse generators. Additionally, it includes the development of new materials that mitigate corrosion while being in contact with liquid metals and salts as required for

future liquid metal batteries and the technical feasibility and scaling of CO_2-free methane pyrolysis in liquid high-temperature Sn respectively. Considering the application of high-power microwaves to new and innovative energy-efficient industrial processes, in 2021 third-party projects include the research on e. g. energy efficient carbon fiber production. Further activities investigate the microwave assisted intermittent pultrusion of CFRP profiles, microwave assisted additive manufacturing with continuous carbon fiber reinforced thermoplastic filaments and the lamination of synthetic textiles for automotive industries by energy efficient selective microwave heating.

All research areas are strongly interdisciplinary and require the profound knowledge on modern electron beam optics, high power micro- and millimeter waves, sub-THz technologies, vacuum electronics, material technologies, high voltage technologies and high voltage measurement techniques.

Table of Contents

Institute for Pulsed Power and Microwave Technology (IHM)
Institut für Hochleistungsimpuls- und Mikrowellentechnik (IHM) i

Director: Prof. Dr.-Ing. John Jelonnek i

Table of Contents iii

1 Nuclear Fusion (FUSION): Plasma Heating Systems - Microwave Plasma Heating & Current Drive Systems - 5

1.1 Gyrotron Development for W7-X 6
1.2 Long Pulse operation with the 1 MW, 170 GHz refurbrished CW Gyrotron for ITER 8
1.3 EUROfusion ENR Project 10
1.4 New Interaction Code SimpleRick 12
1.5 Development of Multistage Depressed Collectors 13
1.6 Quasi-Optical Mode Converter, Broadband Window and Matching Optical Unit (MOU) 14
1.7 Plasma stabilization for DEMO 16
1.8 Frequency-Stabilization of MW-Class Gyrotrons at W7-X 18
1.9 Theoretical Studies on Performance Improvement of MW-Class Gyrotrons by External Signal Injection 19
Journal Publications 20

2 Materials and Technologies for the Energy Transition (MTET): - Bioenergy, Concentrated Solar Power and High Temperature Storage - 31

2.1 PEF-Processing of Microbial Biomass 32
2.1.1 SABANA-Project: Adaption of the KEA-facility to Microalgae Processing 32
2.1.2 PEF-Assisted Extraction of Valuable Compounds from Chicory 33
2.1.3 PEF Treatment Extracts a Cell-Death Inducing Factor from Chlorella Vulgaris in Stationary Phase 34
2.1.4 Impact of Incubation Time on Availability of Total Organic Carbon with PEF-Treated Microalgae *Auxenochlorella Protothecoides* for Final Anaerobic Digestion (AD) 35
2.1.5 Energetic Valorization of Microalgae by Combination of PEF Treatment and Direct Transesterification 37
2.2 Components and Electroporation Processes 39
2.2.1 Semiconductor-Based Marx-Type Pulse Generator for PEF-treatment of Potatoes 39
2.2.2 Fast SiC-MOSFET Switch 40
2.3 Concentrating Solar Power (CSP) and High Temperature Thermal Storage / Liquid Metal – Material Compatibility 42
2.3.1 CSP – Simulation of Transient Heat Loads 42
2.3.2 Material Development 43
2.3.3 Liquid metal battery 45
Journal Publications 47

3 Safety Research for Nuclear Reactors (NUSAFE): Transmutation - Liquid Metal Technology - 49

3.1 Material development and advanced corrosion mitigation strategies for heavy liquid metal-cooled nuclear systems 50
3.1.1 GESA 50
3.1.2 Erosion corrosion experiments in the CORELLA facility 51
3.1.3 Material development to mitigate corrosion 52
Journal Publications 53

4 Materials and Technologies for the Energy Transition (MTET): Power-based Fuels and Chemicals - Microwave Process Technology - 55

4.1 Plasma Chemistry 56
4.2 Energy-Efficient Laminating Technology with Optimized, Innovative Microwave Technology for 3-Dimensional Form Parts (e-KOMFORT) 57
4.3 Energy-Efficient Production of Robust Carbon Fibers (REINFORCE) 58
4.4 Smart Tomographic Sensors for Advanced Industrial Process Control (TOMOCON) 59
4.5 Innovative Microwave Pultrusion for the Cycle Controlled Sequential Curing of Fiber Reinforced Plastics for Modular Automated Manufacture of Complex Components (IMPULS) 60
4.6 3D Microwave Printing of Composites 61
4.7 Airborne Transmission of SARS Coronavirus (CORAERO) 62
Journal Publications 63

Appendix 65

Equipment, Teaching Activities and Staff 65
Strategical Events, Scientific Honors and Awards 65
Longlasting Co-operations with Industries, Universities and Research Institutes 66

1 Nuclear Fusion (FUSION): Plasma Heating Systems - Microwave Plasma Heating & Current Drive Systems -

Contact: Dr. Gerd Gantenbein

The Department for High Power Microwave Technologies focuses on the research and development of high power microwave sources based on vacuum electronics (gyrotrons) and related components for Electron Cyclotron Resonance Heating and Current Drive (ECRH & CD) of magnetically confined nuclear fusion plasmas. This research on high power microwaves is complemented by the research and development on applications of high power microwaves to chemical processes, materials and composites.

In particular the following major activities have been carried out in 2021:

- Gyrotron development for W7-X, targeting at 1.5 MW RF power at 140 GHz, the short pulse gyrotron has been further optimized towards a parasitic free operation with an output power of up to 1.6 MW.
- Long pulse operation with the 1 MW, 170 GHz refurbished CW gyrotron for ITER, showed an output power of up to 1044 kW for 40 s and 470 kW for 1600 s.
- An Enabling Research Project (ENR) funded by EUROfusion focusing on new concepts for highly efficient megawatt-class fusion gyrotrons has been started.
- A new, PIC-based, interaction code (SimpleRick) has been extended to include a 3D beam of macroparticles for simulation of gyrotrons with classical hollow cavities as well as gyrotrons with coaxial cavities.
- Manufacturing and assembling of a multi-staged depressed collector, which is supposed to push the gyrotron efficiency beyond 60 %, has been initiated.
- Considering the development of quasi-optical components a launcher design for co- and counter-rotating modes has been studied and properties of broadband windows have been investigated.
- Plasma stabilisation with ECCD is an important topic for current and future fusion devices. IHM is contributing to this field with simulations on stabilisation of neoclassical tearing modes for DEMO.
- Advanced application of gyrotrons for plasma diagnostics, e.g. collective Thomson scattering, call for very stable oscillating frequencies. Experiments have been conducted to stabilize the frequency of megawatt class gyrotrons.
- Theoretical studies studies on performance improvement of MW-class gyrotrons by external signal injection have been started.

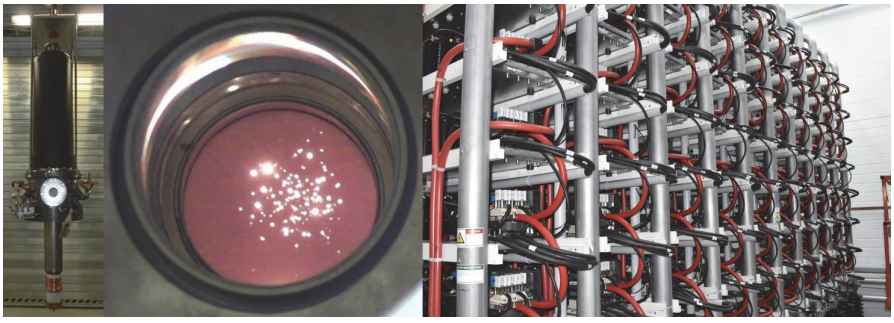

1.1 Gyrotron Development for W7-X

Contact: Dr. Tomasz Rzesnicki

The development of a Continuous-Wave (CW) 1.5 MW, 140 GHz prototype gyrotron for the upgrade of the ECRH system at W7-X has been ongoing, within a contract between IPP and the industrial partner (Thales, Vélizy-Villacoublay, France). KIT/IHM is involved in this development within the framework of EUROfusion Work Package W7-X (WPS1). In parallel to the CW prototype, KIT developed a short-pulse (ms) pre-prototype gyrotron, which was successfully tested during a first experimental campaign back in 2020, providing a first validation of the RF design and the electron beam optics design of the CW gyrotron. The validation was completed in 2021, after extensive theoretical investigations on the experimental results: a very good simulation/experiment agreement was achieved (Fig. 1.1.1), confirming also an excellent gyrotron construction.

In order to test an alternative configuration of the gyrotron beam tunnel, theoretically foreseen to enlarge the parasitic-free operational area, the gyrotron was reassembled with a modified, in terms of absorbing material, beam tunnel. In a second experimental campaign, an excellent parasitic-free performance was again demonstrated with the modified gyrotron. In particular, 1.6 MW at 43 % efficiency in ~1 ms pulses with depressed collector was achieved. Using high-power measurements, the Gaussian mode content of the output RF beam was calculated to be higher than 97.7 %. Moreover, the modified beam tunnel exhibited some enlargement of the parasitic-free operational area at the current values of interest (i.e. 50 - 60 A), as shown in Fig. 1.1.2.

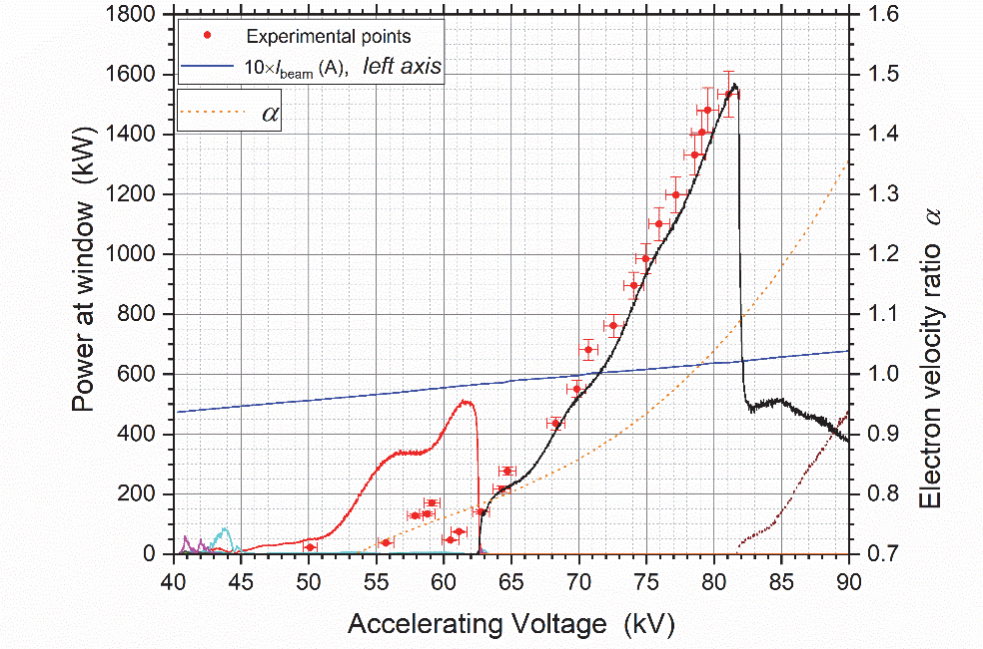

Fig. 1.1.1: Simulation/experiment comparison for the output power of the 1.5 MW short-pulse gyrotron. The black curve corresponds to the operating $TE_{28,10}$ mode.

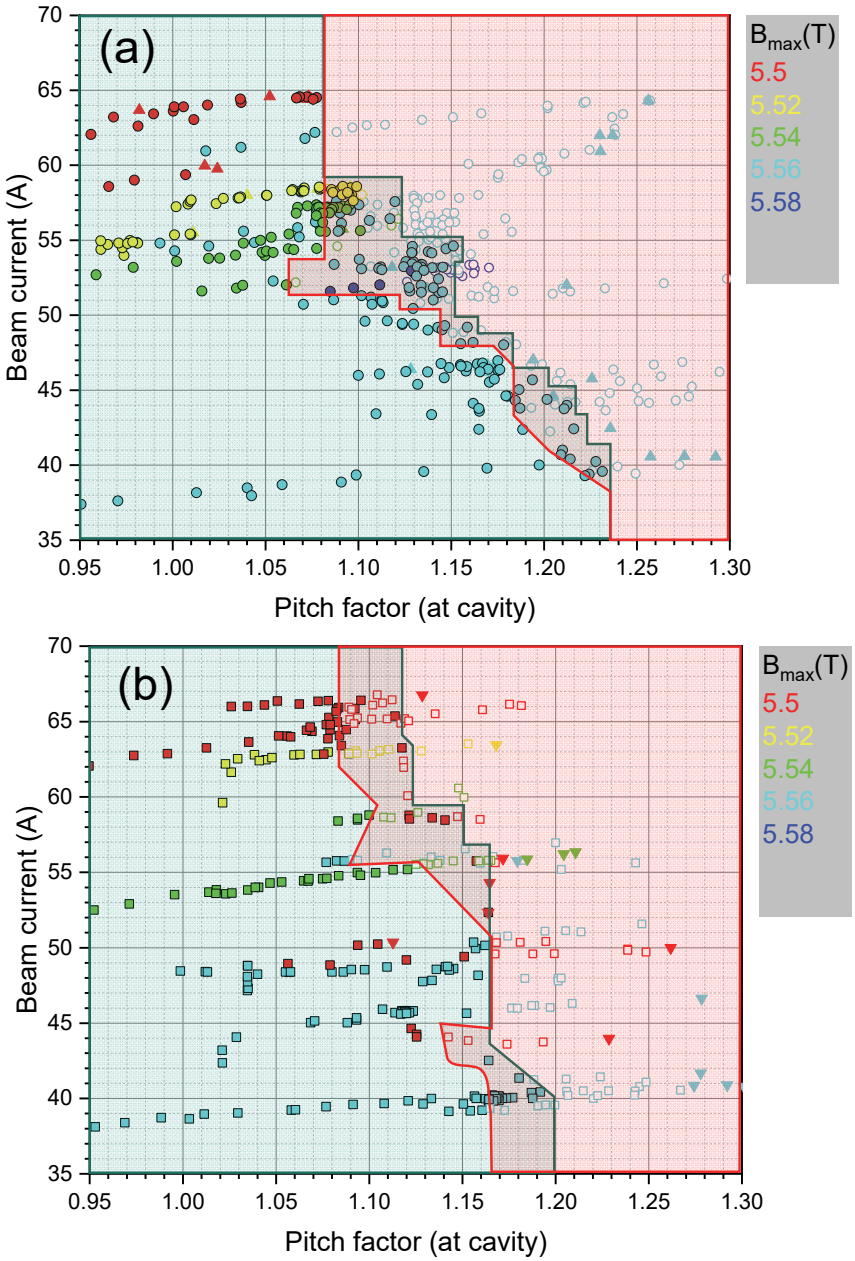

Fig. 1.1.2: Experimental pulses with the 1.5 MW short-pulse gyrotron placed on the current – electron velocity ratio (pitch factor α) operational space. The green container includes all parasitic-free pulses, whereas the red container includes all pulses with parasitics. (a) 1st campaign with baseline beam tunnel. (b) 2nd campaign with alternative beam tunnel.

Following the successful second experimental campaign, a complementary Critical Design Review (CDR) meeting took place in May 2021, at which the design of the CW gyrotron was finalized, including the alternative beam tunnel and an advanced cavity-cooling circuit. This cooling circuit was verified by a series of multi-physics studies, jointly performed by IHM and Politecnico di Torino. The CW tube delivery is foreseen for January 2022 and the Site Acceptance Tests will take place at KIT. A significant effort on preparing the KIT gyrotron test stand for these tests is ongoing, encompassing preparations for the installation of the cryo-free magnet, the interface between the gyrotron and the microwave box, the cooling circuit and the control system.

1.2 Long Pulse operation with the 1 MW, 170 GHz refurbished CW Gyrotron for ITER

Contact: Dr. Tomasz Rzesnicki

The experimental tests performed at KIT in 2020 in short-pulse operation regime showed a very high potential of the refurbished European 170 GHz, 1 MW CW gyrotron (Fig. 1.2.1). Due to the introduced improvements on the tube, in contrast to the very first campaign in 2016, it was now possible to demonstrate the required power level in a long pulse operation regime. With accelerating voltage V_{acc} = 84.5 kV (collector depression voltage V_{body} = 30.7 kV) and I_{beam} = 44.9 A beam current, the maximum achieved power (towards the end of the pulse) was 920 kW with a total efficiency of 38 %, at 180 s pulse length, which is the maximum possible pulse length with the KIT test stand. By further reducing the electron beam current below 30 A it was possible to extend the pulse length to 1600 s with accelerating voltage Vacc = 78.5 kV (depression voltage Vbody = 31.7 kV). At these operating conditions the generated output power was 470 kW, which corresponds to a total efficiency of 35 %. By increasing the depression voltage by 2 kV the efficiency was further improved to 42 %. With further optimization of the magnetic field profile, motivated by recent theoretical findings from the interaction code, an even better performance was achieved. With accelerating voltage Vacc = 86.4 kV (depression voltage Vbody = 26 kV) and beam current Ibeam = 45.7 A, the average output power at the window surpassed for the first time 1 MW (1044 kW) in long pulse operation, with a total efficiency of 38 %.

Fig. 1.2.1: EU ITER 170 GHz, 1 MW CW gyrotron installed in the test stand at IHM/KIT.

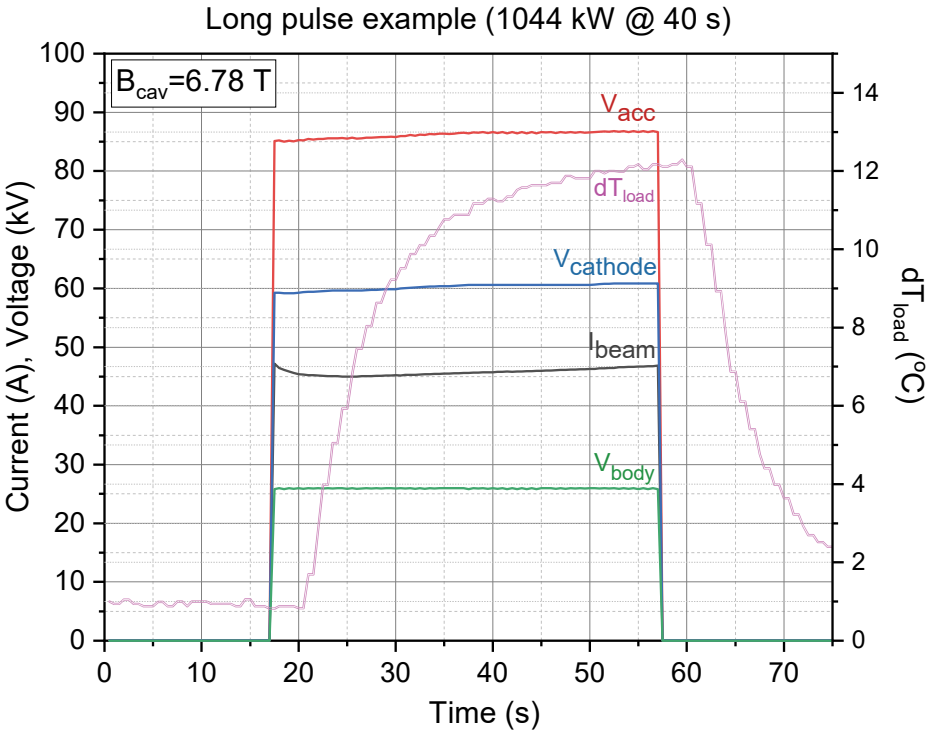

Fig. 1.2.2: Example of a 40 s pulse with 1044 kW peak power and 38 % efficiency (depressed collector operation).

The most interesting gyrotron parameter and their characteristic during the pulse are presented in Fig. 1.2.2. Due to a problem with the cooling system of the KIT gyrotron test stand, the maximal pulse length at 1044 kW was limited to 40 s only. The power balance in the system during the pulses was at the very high level of level of 99.1 %. No further steps towards improving the efficiency, i.e. by increasing the depression voltage were performed, due to lack of time because of the very tight experimental schedule of the test stand. After finalisation of the experimental campaign at KIT the 170 GHz, 1 MW CW prototype gyrotron was transported to EPFL in Lausanne in order to continue with the long-pulse experiments, where further optimization of the gyrotron operating parameters, targeting at higher efficiency of the tube, and finally CW operation up to 1000 s are expected.

.

1.3 EUROfusion ENR Project

Contact: Dr. Stefan Illy

In 2021 a new EUROfusion Enabling Research Project (ENR) has been initiated in collaboration with the National and Kapodistrian University of Athens (NKUA), Greece. The project focuses on new concepts for highly efficient, megawatt-class fusion gyrotron systems that will operate at the second harmonic of the electron cyclotron frequency. This will reduce the required magnetic flux density by a factor of two and therefore will lead to more compact and cost-efficient gyrotron systems at DEMO relevant and sub-THz frequencies.

To form a basis for efficient and stable operation at the 2nd harmonic, the following theoretical investigations have been performed from mid-2021:

- Operation at second harmonic for two different high-order operation modes based on single-mode and multi-mode simulations; the latter directly indicate that 2nd harmonic operation without additional means is not possible due to the dominating first harmonic oscillation.
- The possibility to stabilize 2nd harmonic operation by injection locking; here the obtained results showed that a stable operation is difficult to reach, even at high levels of injected power. One major outcome of these investigations is the fact that relative high-power loading on the gyrotron resonator wall has to be expected caused by the injected signal.
- To overcome the stability/concurrency problems, the application of outer corrugations on the resonator wall has been suggested and initial investigations have been performed to find a sufficient design strategy connected to the outer corrugations (based on the analysis of eigenvalue-curves).
- A possible technical solution for the coupling in of the injected driving power has been investigated based on a proposed dual-beam quasi-optical output system; in addition, the KIT in-house code KarLESSS has been enhanced to support this.

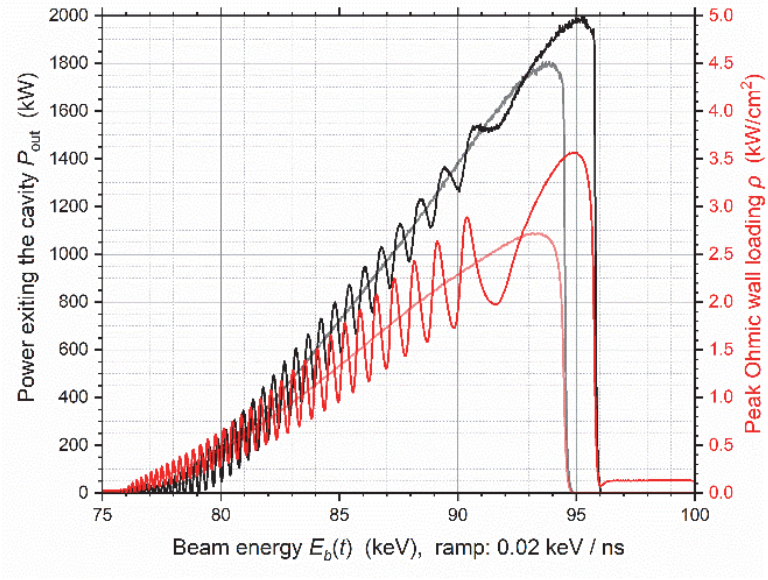

Fig. 1.3.1: Start-up scenario for the $TE_{40,23}$ mode operating at the 2nd harmonic at 204 GHz driven with 180 kW of injected power (black curve: output power, red curve: peak Ohmic wall loading). The results for the free running case are shown by the pale curves for comparison.

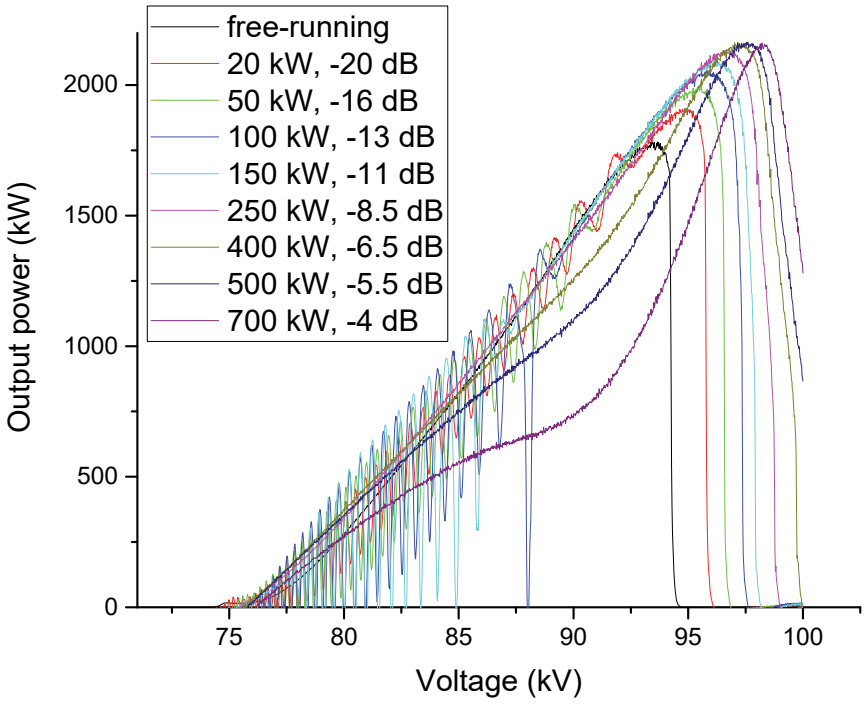

Fig. 1.3.2: Start-up scenarios for the $TE_{34,19}$ mode operating at the 2nd harmonic at 170 GHz for different levels of injected power.

Fig. 1.3.1 and Fig. 1.3.2 illustrate so called start-up scenarios showing the output power vs. the acceleration voltage for different operation modes taking injection locking into account.

.

1.4 New Interaction Code SimpleRick

Contact: M.Sc. Alexander Marek

In the frame of a doctoral thesis at KIT, a new simulation tool, named “SimpleRick”, for the simulation of the electron-wave interaction in gyro devices is developed. The main propose for SimpleRick is the simulation of devices with helically corrugated interaction regions, e.g. helical gyro-TWTs. However, during the last year, the new simulation model was extended and carefully verified to enable the simulation of gyrotrons with classical hollow cavities as well as gyrotrons with coaxial cavities.

In contrast to common gyrotron simulation models, the new model includes a 3D beam of macro-particles (PIC approach) and a source term derived for an arbitrary electron beam without restriction of the generality. This provides a number of advantages: It allows the simulation of electron beams with arbitrary particle distributions e.g. velocity spread, energy spread, offset of the guiding center from the symmetry axis of the device, etc. In addition, the consideration of inhomogeneities or misalignment of the static magnetic field is possible. A direct usage of simulation results from electron gun simulations is possible and it simplifies the interface to specialized simulation tools for the simulation of the electron beam behavior in the structures following the interaction space, namely the collector. A further advantage of the individual handling of macro particles is the possibility to include additional physical effects such as influences of space-charge fields. Last but not least, the general formulation of the source term allows an electron-wave interaction at arbitrary harmonics which can be important for the investigation of parasitic mode excitation.

A further difference of SimpleRick compared to classical gyrotron simulation models is the optional fast time-scale simulation. In classical transient gyrotron simulations, the electric field description is based on the slowly varying amplitudes approach to simplify and speed up the simulation. This approach is sufficient for the description of processes with a narrow bandwidth. However, it leads to significant inaccuracies if broadband effects should be simulated. In SimpleRick, the full Helmholtz equation can be used for simulations which allows a correct modeling of broadband effects. In future, this feature should be used for a detailed investigation of after cavity interactions (ACI).

Compared to full-wave PIC simulations, the SimpleRick retains a significant gain of simulation speed and it still allows a detailed investigation and separation of the involved physical effects.

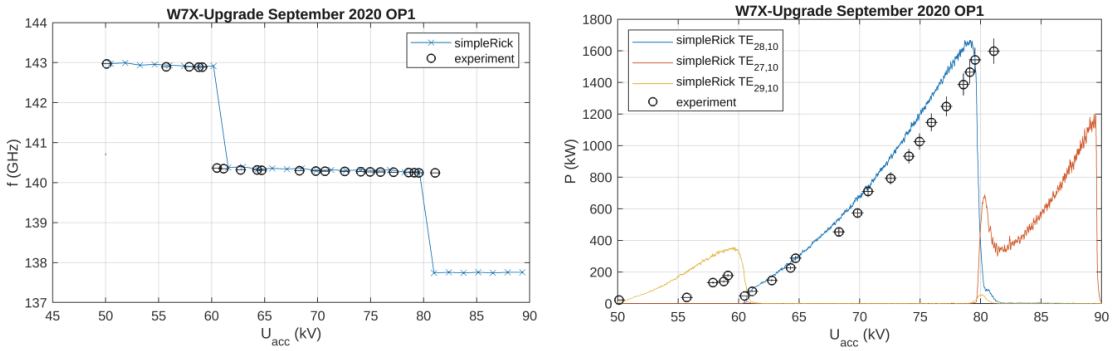

Fig. 1.4.1: Comparison of experimental and simulation results of the RF frequency (left) and power (right) at the gyrotron window for the pre-prototype 1.5-MW gyrotron for the upgrade of the electron cyclotron resonance heating system at the stellarator W7-X.

1.5 Development of Multistage Depressed Collectors

Contact: M.Sc. Benjamin Ell

Multistage Depressed Collector (MDC) technology is one of the key components for continuous wave (CW) gyrotrons operating at megawatt-class output power to achieve a significant increase in the overall efficiency of the vacuum tube. A target for the gyrotron efficiency of ≥ 60 % is planned for the compact *E*×*B* MDC prototype for the first short pulse experiments. The manufacturing of the first prototype MDC at KIT is in the final steps and the assembly will start in the near future. The main limitation of the short pulse prototype for experiments with long pulses or continuous wave operation is the high density of the power loading at the collector surface. The theoretical studies related to the development of the continuous wave compatible design approach were continued. A comparison in size between the short pulse MDC and the continuous wave compatible design is shown in Fig. 1.5.1. An alternative concept to distribute the power loading of the spent electron beam on the first collector stage to a larger surface is studied with a periodic variation of the voltage operation point of the collector system. The collector efficiency was slightly improved compared with a pure magnetic field sweeping system, which was implemented only for the second collector stage of the continuous wave MDC. However, the requirements of the power supplies and the reflected current are increased with the variable depression potentials. The thermal expansion of the continuous wave compatible MDC design is studied and is considered in a future design concept. The position where the second collector stage is mounted is most critical when thermal expansion is considered.

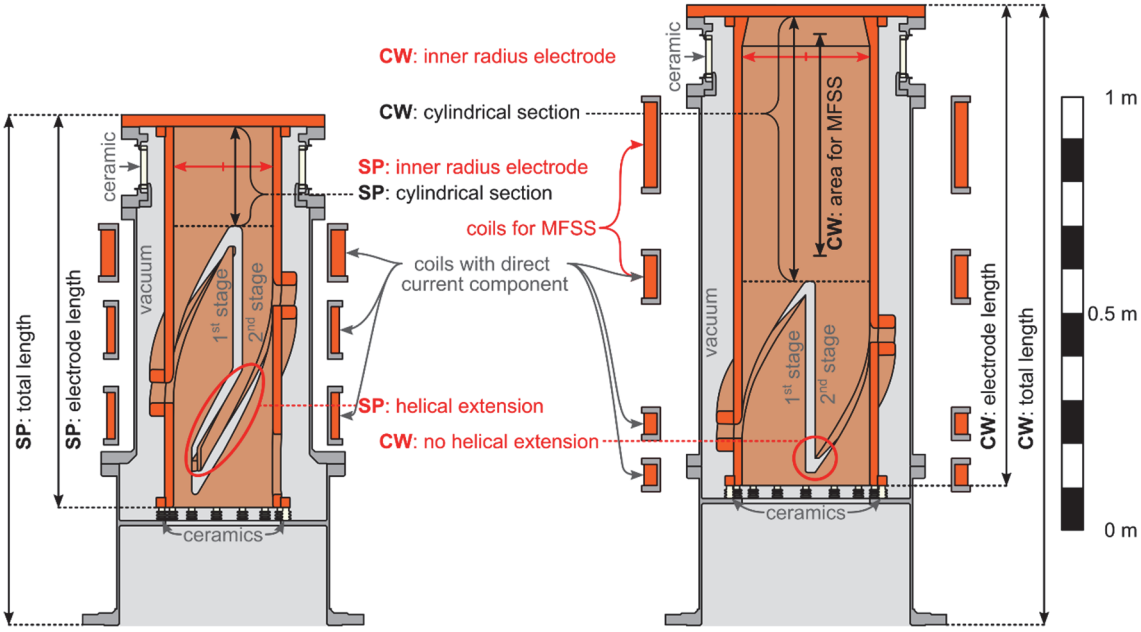

Fig. 1.5.1: Comparison between the short pulse MDC prototype (left) and the MDC design approach for continuous wave operation (right).

1.6 Quasi-Optical Mode Converter, Broadband Window and Matching Optical Unit (MOU)

Contact: Dr. Jianbo Jin

In 2021, the work on the simulation of quasi-optical components for gyrotrons focused on:

1) the development of launchers for co- and counter-rotating modes
2) the application of simulation tools to achieve a proper simulation of EM resonances in broadband windows
3) the design of a Matching Optical Unit (MOU) as an interface between the gyrotron output and the HE_{11}-waveguide that is capable to operate at two frequencies.

Launcher for co- and counter-rotating modes

A new type of launcher with Denisov-type perturbation has been designed for conversion of co- and counter-rotating modes. As an example, a launcher operating at 170 GHz has been designed to convert the $TE_{32,9}$ and $TE_{-32,9}$ modes into Gaussian-like modes. The parameters of the new launcher have been optimized to provide the following RF beams with Gaussian mode contents of 96.65 % at the launcher aperture.

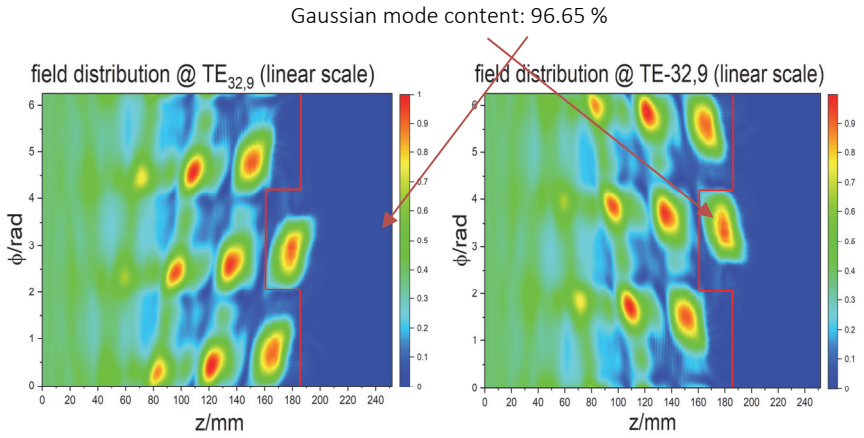

Fig. 1.6.1: Field distributions on the launcher wall and aperture @$TE_{32,9}$ mode (left) and $TE_{-32,9}$ mode (right).

Initial application of simulation tools to achieve a proper simulation of EM resonances in broadband windows

The in-house computer code which is used to calculate the reflection of Gaussian beams on window disks has been improved to include the gradients of wavefronts of Gaussian beams on window disks. Fig. 1.6.2(a) shows the reflections of the Gaussian modes with beam waists of 20 mm operating in the frequency band from 167 GHz to 173 GHz with different disk thicknesses d ranging from 1.850 mm up to 1.853 mm. The Rayleigh length is about 725 mm. Comparing Fig. 1.6.2(b) to Fig. 1.6.2(a), one can see the reflection curves are in good agreement in the case that the window surface are close to the location of beam waists. In Fig. **1.6.2** (b), z_0 represent the distance between the window and the location of beam waists. In case that z_0 = -360 mm, the distance is nearly half of the Rayleigh length, the change in the direction of the vectors of the gradient of the wavefront distributed on the window plane are very small. Hence, the curve shown in Fig. 1.6.2(b) is very close to that with z_0 = 0 mm. When the distance z_0=730 mm, the reflection curve looks quite strange indicating a numerical problem which needs further investigation.

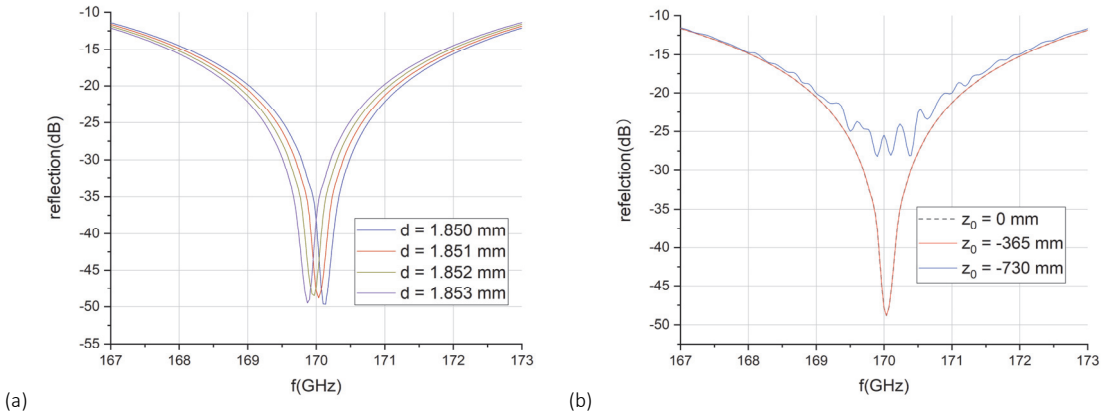

Fig. 1.6.2: Reflections of Gaussian beams on the diamond window: (a) without and (b) with gradient variation of wavefronts on the window disk.

The upgrade of the KarLESSS code to solve MFIE has been started. Subroutines for generating meshes on waveguide and window surfaces have been developed. The curl-conforming basis functions will be used in the MFIE. A subroutine to generate the curl-conforming RWG basis function $\hat{n} \times$ RWG functions has been developed and has been integrated into the KarLESSS code.

Two-frequency MOU for HE_{11} waveguide

An MOU has been designed to transform gyrotron output beams into the HE_{11} waveguide mode operating at either of both DEMO relevant frequencies of 170 GHz and 204 GHz. The field patterns at the entry of the HE_{11} waveguide are shown in Fig. 1.6.3. The simulation results show the HE_{11} mode contents and power transmission efficiencies are estimated as 96.57 % and 95.5 % (170 GHz), 88.23 % and 98.18 % (204 GHz), respectively.

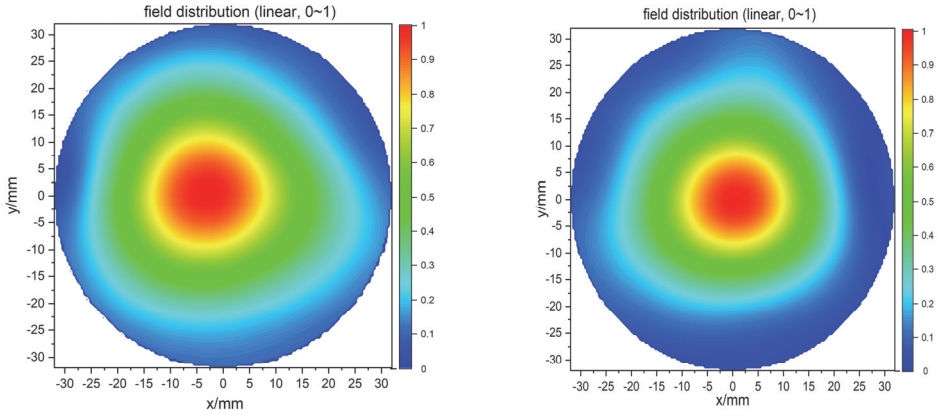

Fig. 1.6.3: Field distributions at the entry of the HE_{11} waveguide: 170 GHz (left) and 204 GHz (right).

1.7 Plasma stabilization for DEMO

Contact: Dr. Chuanren Wu

The study on the application of DEMO gyrotrons for the Neoclassical Tearing Mode (NTM) stabilization in the latest DEMO scenario is continued. After revising the previous implementation of the modified Rutherford equation and the stabilization effect by Electron Cyclotron Resonance Current Drive (ECCD), the impact of the recent changes on the model are evaluated. The estimated growing speed of NTMs may be slower than the previous estimation, as shown in Fig. 1.7.1 (top); however, when using numerically simulated realistic ECCD deposition profiles instead of the previous analytical scaling, it was found that the stabilization effect by ECCD should also be noticeably weaker. Both effects cancel each other so that the required injection power fortunately does not change significantly. Based on the recent model, the feasibility by using tunable-frequency EC system is studied. Fig. 1.7.1 (bottom) shows the case of searching and stabilizing the 2/1 NTM using tunable frequency EC wave beams with 19 MW injected microwave power. Until now, all studies were on the few reference scenarios. In order to consider the evolution of plasma, also to include the dynamical influences from the other subsystems, and to prepare the model of a full-featured EC system control loop, so-called flight-simulator is required to take them into account altogether. Such a flight simulator was under development at IPP, where the proof-of-concept stage has been reached for DEMO and ASDEX-Upgrade.

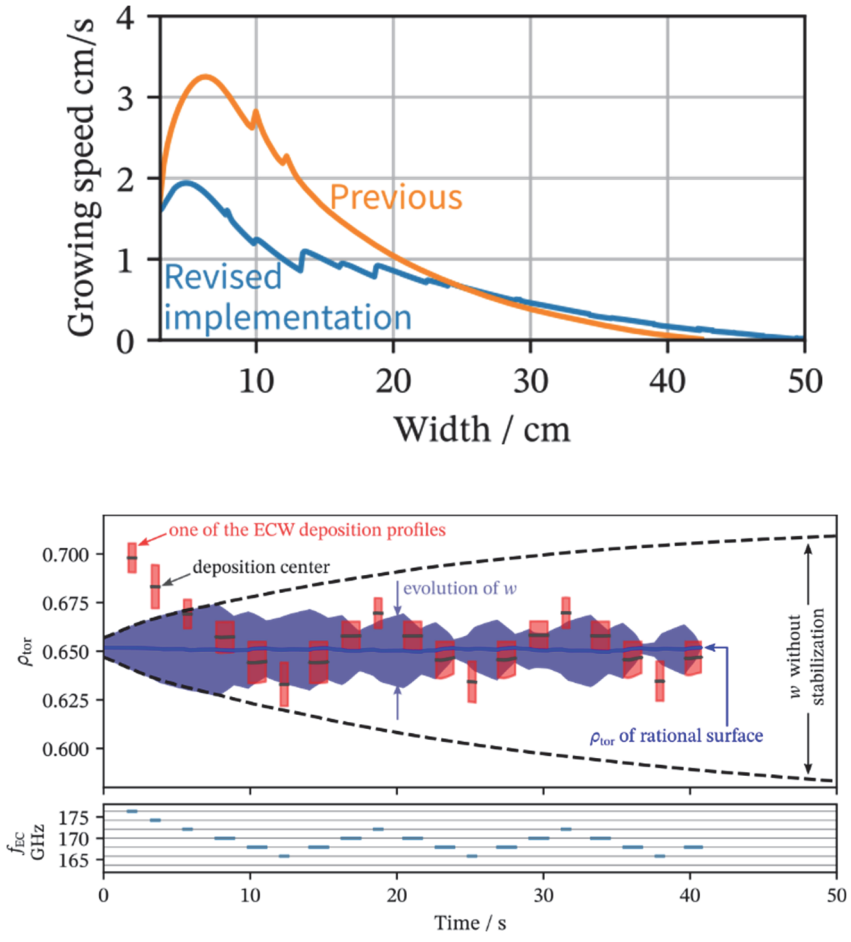

Fig. 1.7.1: Revised implementation of the modified Rutherford equation (top) and simulation of NTM control with tunable gyrotron frequency (bottom).

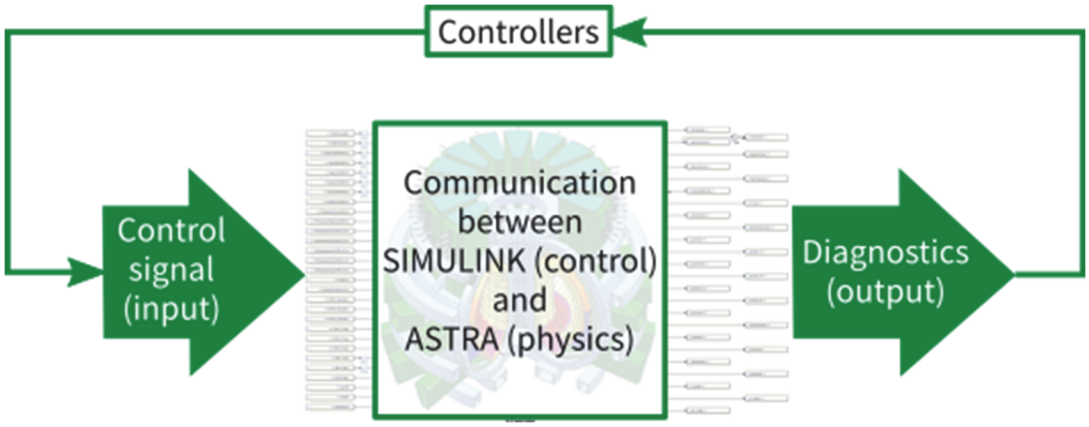

Fig. 1.7.2: The communication module in the DEMO flight simulator infrastructure.

In the year 2021, KIT contributed to one of the core elements in the infrastructure, which is the communication module for the physics co-simulation, as shown in **Fehler! Verweisquelle konnte nicht gefunden werden.**. The mechanisms in the communication with the physics simulation have been overhauled and several critical bugs have been fixed, both for ASDEX-Upgrade and DEMO. A clean refactorization is foreseen at the beginning of the year 2022 for hugely increasing its flexibility and also to reduce the maintenance efforts, then a full-featured Electron Cyclotron Heating and Current Drive system model for DEMO can be introduced.

1.8 Frequency-Stabilization of MW-Class Gyrotrons at W7-X

Contact: M.Sc. Laurent Krier

Based on the theoretical analysis about Phase-Locked Loop (PLL) stabilization of gyrotrons from last year, first experiments were conducted to stabilize the frequency of the heating gyrotrons at W7-X with an off-the-shelf PLL system.

The conducted experiments show that the PLL-system significantly increases the stability of the gyrotron output frequency. In Fig. 1.8.1, the spectra of a free-running and a PLL-stabilized gyrotron are compared. The spectrum of the free-running operation has multiple peaks at different frequencies, while for the PLL-stabilized operation a clear single peak at the desired frequency is visible. However, for the PLL-stabilized operation, several sidepeaks are still present in the spectrum. These sidepeaks coincide with noise observed in the gyrotron power supplies. To further improve the gyrotron output frequency, the noise level of the power supply needs to be reduced.

These first experiment with the off-the-shelf PLL system show the potential of such control systems for high-power gyrotrons. However, the used PLL system was an analogue system and was not flexible to test different gyrotron operations or to be integrated into the W7-X control system. Therefore, a new digital PLL system was designed and implemented on an FPGA board.

Finally, the new digital PLL system was used in new frequency stabilization experiments with the W7-X gyrotrons and showed similar results than the previous off-the-shelf system. The new digital system can be fully integrated into the W7-X control system and is beneficial for applications such as Collective Thomson Scattering diagnostic or direct ion heating with beat waves from two gyrotrons.

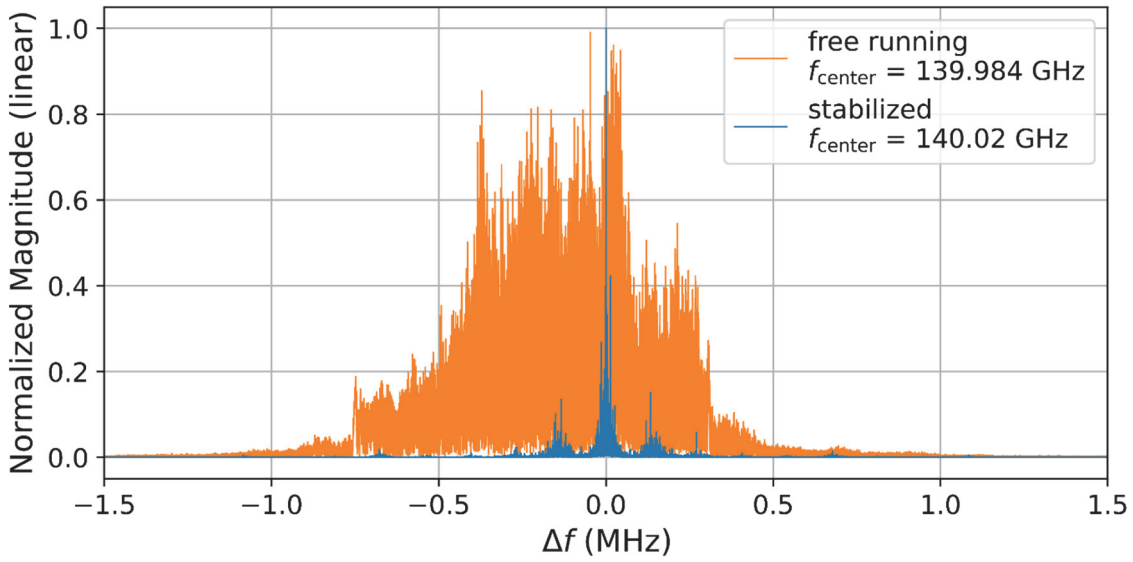

Fig. 1.8.1: Comparison of a free-running and PLL-stabilized gyrotron operation at W7-X.

1.9 Theoretical Studies on Performance Improvement of MW-Class Gyrotrons by External Signal Injection

Contact: Dr. Tomasz Rzesnicki

By injecting a low-power signal, of the order of -20 dB below the nominal output power, it is possible to lock the gyrotron frequency to that of the external signal, provided that the frequency of the signal stays within a specific locking bandwidth around the operating frequency of the free-running gyrotron. In this way, full control of the gyrotron frequency can be achieved opening new possibilities in fusion diagnostics, spectroscopy, radar etc. Using the in-house code-package EURIDICE, recently upgraded to address external signal injection, detailed studies on injection locking of the 170 GHz 2 MW coaxial-cavity gyrotron at KIT have been carried out. It was shown that the locking bandwidth is in proper agreement with the model of Kurokawa. It was also found that injection locking improves the interaction efficiency and the range of mode excitation. However, given that the coaxial gyrotron is already operating close to the optimum regime, this improvement is noticeable albeit not remarkable (see Fig. 1.9.1). On the other hand, it was discovered that an injection signal containing competing modes can lock these modes to frequencies that prevent them from being excited at high power. This idea could be a breakthrough with respect to mode competition control in high-power gyrotrons.

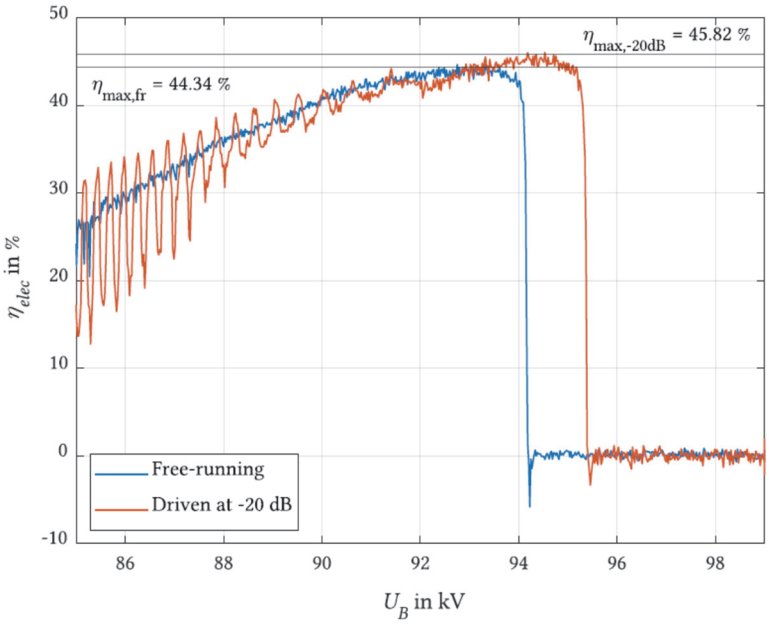

Fig. 1.9.1: Electronic efficiency versus beam voltage (increasing at a rate of ~0.03 kV/ns) for the 170 GHz 2 MW coaxial gyrotron. In the driven case, a 30 kW external signal at 169.972 GHz is used. The oscillations appearing below 92 kV in the driven case reflect the non-locked regime. From 92 kV onwards, the frequency of the operating mode is locked to the injected frequency.

Involved Staff:

KIT/IHM: D. Albert, Dr. K. Avramidis, B. Ell, **Dr. G. Gantenbein, Dr. S. Illy**, Dr. Z. Ioannidis, Prof. J. Jelonnek, Dr. J. Jin, Th. Kobarg, D. Kranz, L. Krier , R. Lang, W. Leonhardt, A. Marek, D. Mellein, Dr. I. Pagonakis, A. Papenfuß, T. Ruess, **Dr. T. Rzesnicki**, M. Schmid, Dr. S. Stanculovic, Prof. M. Thumm, J. Weggen, N. Wirth, Dr. Ch. Wu, **IGVP (University of Stuttgart): Dr. C. Lechte**, **IPP (Greifswald/Garching):** Dr. H. Braune, **Dr. H.Laqua**, Dr. S. Marsen, F. Noke, Dr. T. Stange

Journal Publications

W7-X Team; Puig Sitjes, A.; Jakubowski, M.; Naujoks, D.; Gao, Y.; Drewelow, P.; Niemann, H.; Fellinger, J.; Moncada, V.; Pisano, F.; Belafdil, C.; Mitteau, R.; Aumeunier, M.-H.; Cannas, B.; Casas, J. R.; Salembier, P.; Clemente, R.; Fischer, S.; Winter, A.; Laqua, H.; Bluhm, T.; Brandt, K.; Gantenbein, G.; Huber, M.; Illy, S.; Jelonnek, J.; Kobarg, T.; Lang, R.; Leonhardt, W.; Mellein, D.; Papenfuß, D.; Thumm, M.; Wadle, S.; Weggen, J. (2021). Real-Time Detection of Overloads on the Plasma-Facing Components of Wendelstein 7-X. Applied Sciences, 11 (24), Article no: 11969. doi:10.3390/app112411969

Becker, S.; Beckmann, J.; Cojocari, O.; Feige, V.; Fischer, B.; Frank, S. van; Friederich, F.; Globisch, B.; Hechtfischer, G.; Hens, K.; Hubers, H.-W.; Jelonnek, J.; Jonuscheit, J.; Kehrt, M.; Keil, A.; Kleine-Ostmann, T.; Liebermeister, L.; Mayr, M.; Nusler, D.; Peichl, M.; Peters, O.; Schur, J.; Sprenger, T.; Steiger, A.; Vieweg, N.; Wilk, R. (2021). New Series of Standards VDI/VDE 5590 on Terahertz Systems. 2021 46th International Conference on Infrared, Millimeter and Terahertz Waves (IRMMW-THz), 1–2, Institute of Electrical and Electronics Engineers (IEEE). doi:10.1109/IRMMW-THz50926.2021.9566934

Ruess, T.; Gantenbein, G.; Ioannidis, Z.; Rzesnicki, T.; Wagner, D.; Thumm, M.; Jelonnek, J. (2021). Frequency and mode measurement techniques for megawatt-class gyrotrons. Technisches Messen. doi:10.1515/teme-2021-0039

Brücker, P. T.; Avramidis, K. A.; Marek, A.; Thumm, M.; Jelonnek, J. (2021). Theoretical Investigation on Injection Locking of the EU 170 GHz 2 MW TE34,19-Mode Coaxial-Cavity Gyrotron. 2021 46th International Conference on Infrared, Millimeter and Terahertz Waves (IRMMW-THz), 1–2, Institute of Electrical and Electronics Engineers (IEEE). doi:10.1109/IRMMW-THz50926.2021.9567563

Krier, L.; Avramidis, K. A.; Braune, H.; Gantenbein, G.; Illy, S.; Ioannidis, Z.; Jelonnek, J.; Laqua, H. P.; Marsen, S.; Moseev, D.; Noke, F.; Pagonakis, I. G.; Ruess, T.; Rzesnicki, T.; Stange, T.; Thumm, M.; Wolf, R. C. (2021). Frequency Stabilization of Megawatt-Class 140 GHz Gyrotrons at W7-X Using an Off-the-Shelf PLL System. 2021 46th International Conference on Infrared, Millimeter and Terahertz Waves (IRMMW-THz), 1–2, Institute of Electrical and Electronics Engineers (IEEE). doi:10.1109/IRMMW-THz50926.2021.9566847

Wagner, D.; Kasparek, W.; Leuterer, F.; Monaco, F.; Ruess, T.; Stober, J.; Thumm, M. (2021). Two-Frequency Notch Filters for Sub-THz Plasma Diagnostics. 2021 46th International Conference on Infrared, Millimeter and Terahertz Waves (IRMMW-THz), 1–2, Institute of Electrical and Electronics Engineers (IEEE). doi:10.1109/IRMMW-THz50926.2021.9567148

Savoldi, L.; Avramidis, K. A.; Albajar, F.; Alberti, S.; Leggieri, A.; Sanchez, F. (2021). A validation roadmap of multi-physics simulators of the resonator of mw-class cw gyrotrons for fusion applications. Energies, 14 (23), 8027. doi:10.3390/en14238027

W7-X Team; Mayer, M.; Balden, M.; Brezinsek, S.; Dhard, C. P.; Elgeti, S.; Fajardo, D.; Fellinger, J.; Guitart Corominas, M.; Hiret, P.; Kandler, M.; Krause, M.; Loesser, D.; Lumsdaine, A.; Naujoks, D.; Neilson, H.; Neu, R.; Oelmann, J.; Ruset, C.; Schmidt-Dencker, J.-H.; Gantenbein, G.; Huber, M.; Illy, S.; Jelonnek, J.; Kobarg, T.; Lang, R.; Leonhardt, W.; Mellein, D.; Papenfuß, D.; Scherer, T.; Thumm, M.; Wadle, S.; Weggen, J. (2021). Erosion of tungsten marker layers in W7-X. Physica scripta, 96 (12), Article no: 124070. doi:10.1088/1402-4896/ac3b68

W7-X Team; Dhard, C. P.; Brezinsek, S.; Mayer, M.; Naujoks, D.; Masuzaki, S.; Zhao, D.; Yi, R.; Oelmann, J.; Schmid, K.; Romazanov, J.; Pardanaud, C.; Kandler, M.; Kharwandikar, A. K.; Schlisio, G.; Volzke, O.; Grote,

H.; Gao, Y.; Rudischhauser, L.; Goriaev, A.; Wauters, T.; Kirschner, A.; Sereda, S.; Wang, E.; Rasinski, M.; Dittmar, T.; Motojima, G.; Hwangbo, D.; Kajita, S.; Balden, M.; Burwitz, V. V.; Neu, R.; Linsmeier, C.; Gantenbein, G.; Huber, M.; Illy, S.; Jelonnek, J.; Kobarg, T.; Lang, R.; Leonhardt, W.; Mellein, D.; Papenfuß, D.; Scherer, T.; Thumm, M.; Wadle, S.; Weggen, J. (2021). Plasma-wall interaction studies in W7-X: main results from the recent divertor operations. Physica scripta, 96 (12), Article no: 124059. doi:10.1088/1402-4896/ac35c0

Wu, C.; Aiello, G.; Avramidis, K. A.; Bruschi, A.; Fable, E.; Franke, T.; Gantenbein, G.; Garavaglia, S.; Granucci, G.; Illy, S.; Janky, F.; Jelonnek, J.; Kudláček, O.; Moro, A.; Poli, E.; Ruess, T.; Scherer, T.; Schramm, R.; Siccinio, M.; Snicker, A.; Strauß, D.; Suárez López, G.; Tardini, G.; Thumm, M.; Tran, M. Q.; Zohm, H. (2021). Basic design considerations for a frequency step-tunable electron cyclotron wave system to suppress NTMs in DEMO. Fusion engineering and design, 173, Art.-Nr.: 112931. doi.org/10.1016/j.fusengdes.2021.112931

W7-X Team; Dinklage, A.; Fuchert, G.; Wolf, R. C.; Alonso, A.; Andreeva, T.; Beidler, C. D.; Baar, M. de; Gao, Y.; Geiger, J.; Jakubowski, M.; Laqua, H.; Marushchenko, N.; Neuner, U.; Pablant, N.; Pavone, A.; Rahbarnia, K.; Schmitt, J.; Smith, H. M.; Stange, T.; Turkin, Y.; Gantenbein, G.; Illy, S.; Jelonnek, J.; Krier, L.; Thumm, M. (2021). Validation of theory-based models for the control of plasma currents in W7-X divertor plasmas. Nuclear fusion, 61 (12), Art.Nr.: 126022. doi:10.1088/1741-4326/ac2d58

W7-X Team; Zhang, D.; Burhenn, R.; Feng, Y.; König, R.; Buttenschön, B.; Beidler, C. D.; Hacker, P.; Reimold, F.; Thomsen, H.; Laube, R.; Klinger, T.; Giannone, L.; Penzel, F.; Pavone, A.; Krychowiak, M.; Beurskens, M.; Bozhenkov, S.; Brunner, J. K.; Effenberg, F.; Fuchert, G.; Gao, Y.; Geiger, J.; Hirsch, M.; Höfel, U.; Jakubowski, M.; Knauer, J.; Kwak, S.; Laqua, H. P.; Niemann, H.; Otte, M.; Pedersen, T. S.; Pasch, E.; Pablant, N.; Rahbarnia, K.; Svensson, J.; Blackwell, B.; Drews, P.; Endler, M.; Rudischhauser, L.; Wang, E.; Weir, G.; Winters, V.; Gantenbein, G.; Huber, M.; Illy, S.; Jelonnek, J.; Kobarg, T.; Lang, R.; Leonhardt, W.; Mellein, D.; Papenfuß, D.; Scherer, T.; Thumm, M.; Wadle, S.; Weggen, J. (2021). Plasma radiation behavior approaching high-radiation scenarios in W7-X. Nuclear fusion, 61 (12), Art.-Nr.: 126002. doi:10.1088/1741-4326/ac2b75

W7-X Team; Beurskens, M. N. A.; Bozhenkov, S. A.; Ford, O.; Xanthopoulos, P.; Zocco, A.; Turkin, Y.; Alonso, A.; Beidler, C.; Calvo, I.; Carralero, D.; Estrada, T.; Fuchert, G.; Grulke, O.; Hirsch, M.; Ida, K.; Jakubowski, M.; Killer, C.; Krychowiak, M.; Kwak, S.; Lazerson, S.; Langenberg, A.; Lunsford, R.; Pablant, N.; Pasch, E.; Pavone, A.; Reimold, F.; Romba, T.; Stechow, A. von; Smith, H. M.; Windisch, T.; Yoshinuma, M.; Zhang, D.; Wolf, R. C.; Gantenbein, G.; Huber, M.; Illy, S.; Jelonnek, J.; Kobarg, T.; Lang, R.; Leonhardt, W.; Mellein, D.; Papenfuß, D.; Scherer, T.; Thumm, M.; Wadle, S.; Weggen, J. (2021). Ion temperature clamping in Wendelstein 7-X electron cyclotron heated plasmas. Nuclear fusion, 61 (11), 116072. doi:10.1088/1741-4326/ac1653

W7-X Team; Velasco, J. L.; Calvo, I.; Mulas, S.; Sánchez, E.; Parra, F. I.; Cappa, Á.; Gantenbein, G.; Huber, M.; Illy, S.; Jelonnek, J.; Kobarg, T.; Lang, R.; Leonhardt, W.; Mellein, D.; Papenfuß, D.; Scherer, T.; Thumm, M.; Wadle, S.; Weggen, J. (2021). A model for the fast evaluation of prompt losses of energetic ions in stellarators. Nuclear fusion, 61 (11), Art.-Nr.: 116059. doi:10.1088/1741-4326/ac2994

W7-X Team; Zanini, M.; Buttenschön, B.; Laqua, H. P.; Thomsen, H.; Stange, T.; Brandt, C.; Braune, H.; Brunner, K. J.; Dinklage, A.; Gao, Y.; Hirsch, M.; Höfel, U.; Knauer, J.; Marsen, S.; Marushchenko, N.; Pavone, A.; Rahbarnia, K.; Schilling, J.; Turkin, Y.; Wolf, R. C.; Zocco, A.; Gantenbein, G.; Huber, M.; Illy, S.; Jelonnek, J.; Kobarg, T.; Lang, R.; Leonhardt, W.; Mellein, D.; Papenfuß, D.; Scherer, T.; Thumm, M.; Wadle, S.; Weggen, J. (2021). Confinement degradation and plasma loss induced by strong sawtooth crashes at W7-X. Nuclear fusion, 61 (11), Art.-Nr.: 116053. doi:10.1088/1741-4326/ac2870

W7-X Team; Zhang, D.; Burhenn, R.; Beidler, C. D.; Feng, Y.; Thomsen, H.; Brandt, C.; Buller, S.; Reimold, F.; Hacker, P.; Laube, R.; Geiger, J.; Regaña, J. M. G.; Smith, H. M.; König, R.; Giannone, L.; Penzel, F.; Klinger, T.; Baldzuhn, J.; Bozhenkov, S.; Bräuer, T.; Brunner, J. K.; Buttenschön, B.; Damm, H.; Endler, M.; Effenberg, F.; Fuchert, G.; Gao, Y.; Jakubowski, M.; Knauer, J.; Kremeyer, T.; Krychowiak, M.; Kwak, S.; Laqua, H. P.; Langenberg, A.; Otte, M.; Pablant, N.; Pasch, E.; Rahbarnia, K.; Pavone, A.; Rudischhauser, L.; Svensson, J.; Killer, C.; Windisch, T.; Gantenbein, G.; Huber, M.; Illy, S.; Jelonnek, J.; Kobarg, T.; Lang, R.; Leonhardt, W.; Mellein, D.; Papenfuß, D.; Scherer, T.; Thumm, M.; Wadle, S.; Weggen, J. (2021). Bolometer tomography on Wendelstein 7-X for study of radiation asymmetry. Nuclear fusion, 61 (11), Art.-Nr.: 116043. doi:10.1088/1741-4326/ac2778

W7-X Team; Gradic, D.; Perseo, V.; Kriete, D. M.; Krychowiak, M.; König, R.; Feng, Y.; Otte, M.; Pedersen, T. S.; Gao, Y.; Jakubowski, M.; Schlisio, G.; Warmer, F.; Gantenbein, G.; Huber, M.; Illy, S.; Jelonnek, J.; Kobarg, T.; Lang, R.; Leonhardt, W.; Mellein, D.; Papenfuß, D.; Scherer, T.; Thumm, M.; Wadle, S.; Weggen, J. (2021). 2D coherence imaging measurements of C ion temperatures in the divertor of Wendelstein 7-X. Nuclear fusion, 61 (10), 106041. doi:10.1088/1741-4326/ac25bf

W7-X Team; Velasco, J. L.; Calvo, I.; Parra, F. I.; d'Herbemont, V.; Smith, H. M.; Carralero, D.; Estrada, T.; Gantenbein, G.; Huber, M.; Illy, S.; Jelonnek, J.; Kobarg, T.; Lang, R.; Leonhardt, W.; Mellein, D.; Papenfuß, D.; Scherer, T.; Thumm, M.; Wadle, S.; Weggen, J. (2021). Fast simulations for large aspect ratio stellarators with the neoclassical code KNOSOS. Nuclear fusion, 61 (11), Article no: 116013. doi:10.1088/1741-4326/ac1dc7

W7-X Team; Langenberg, A.; Wegner, T.; Marchuk, O.; García-Regaña, J. M.; Pablant, N. A.; Fuchert, G.; Bozhenkov, S.; Damm, H.; Pasch, E.; Brunner, K.-J.; Knauer, J.; Beurskens, M.; Reimold, F.; Wolf, R. C.; Gantenbein, G.; Huber, M.; Illy, S.; Jelonnek, J.; Kobarg, T.; Lang, R.; Leonhardt, W.; Mellein, D.; Papenfuß, D.; Scherer, T.; Thumm, M.; Wadle, S.; Weggen, J. (2021). Impurity transport in ion- and electron-root confinement scenarios at Wendelstein 7-X. Nuclear fusion, 61 (11), Article no: 116018. doi:10.1088/1741-4326/ac24d4

W7-X Team; Vécsei, M.; Anda, G.; Asztalos, O.; Dunai, D.; Hegedűs, S.; Nagy, D.; Otte, M.; Pokol, G. I.; Zoletnik, S.; Gantenbein, G.; Huber, M.; Illy, S.; Jelonnek, J.; Kobarg, T.; Lang, R.; Leonhardt, W.; Mellein, D.; Papenfuß, D.; Scherer, T.; Thumm, M.; Wadle, S.; Weggen, J. (2021). Swift evaluation of electron density profiles obtained by the alkali beam emission spectroscopy technique using linearized reconstruction. Review of scientific instruments, 92 (11), 113501. doi:10.1063/5.0057158

W7-X Team; Perseo, V.; Winters, V.; Feng, Y.; Reimold, F.; Ford, O. P.; König, R.; Bozhenkov, S. A.; Brunner, K. J.; Burhenn, R.; Drewelow, P.; Ennis, D. A.; Gao, Y.; Gradic, D.; Hacker, P.; Hergenhahn, U.; Jakubowski, M. W.; Knauer, J.; Kremeyer, T.; Kriete, D. M.; Krychowiak, M.; Kwak, S.; Niemann, H.; Pavone, A.; Pisano, F.; Puig Sitjes, A.; Schlisio, G.; Svensson, J.; Zhang, D.; Sunn Pedersen, T.; Gantenbein, G.; Huber, M.; Illy, S.; Jelonnek, J.; Kobarg, T.; Lang, R.; Leonhardt, W.; Mellein, D.; Papenfuß, D.; Scherer, T.; Thumm, M.; Wadle, S.; Weggen, J. (2021). 2D measurements of parallel counter-streaming flows in the W7-X scrape-off layer for attached and detached plasmas. Nuclear fusion, 61 (11), 116039. doi:10.1088/1741-4326/ac277a

W7-X Team; Jakubowski, M.; Endler, M.; Feng, Y.; Gao, Y.; Killer, C.; König, R.; Krychowiak, M.; Perseo, V.; Reimold, F.; Schmitz, O.; Pedersen, T. S.; Brezinsek, S.; Dinklage, A.; Drewelow, P.; Niemann, H.; Otte, M.; Gruca, M.; Hammond, K.; Kremeyer, T.; Kubkowska, M.; Jabłoński, S.; Pandey, A.; Wurden, G.; Zhang, D.; Bozhenkov, S.; Böckenhoff, D.; Dhard, C. P.; Baldzuhn, J.; Gradic, D.; Effenberg, F.; Kornejew, P.; Lazerson, S.; Lore, J.; Naujoks, D.; Puig Sitjes, A.; Schlisio, G.; Ślęczka, M.; Wenzel, U.; Winters, V.; Gantenbein, G.; Huber, M.; Illy, S.; Jelonnek, J.; Kobarg, T.; Lang, R.; Leonhardt, W.; Mellein, D.; Papenfuß, D.; Scherer, T.; Thumm, M.; Wadle, S.; Weggen, J. (2021). Overview of the results from divertor experiments with attached and detached plasmas at Wendelstein 7-X and their implications for steady-state operation. Nuclear fusion, 61 (10), Artk.Nr.: 106003. doi:10.1088/1741-4326/ac1b68

W7-X Team; Laqua, H. P.; Baldzuhn, J.; Braune, H.; Bozhenkov, S.; Brunner, K.; Hirsch, M.; Hoefel, U.; Knauer, J.; Langenberg, A.; Marsen, S.; Moseev, D.; Pasch, E.; Rahbarnia, K.; Stange, T.; Wolf, R. C.; Pablant, N.; Grulke, O.; Gantenbein, G.; Huber, M.; Illy, S.; Jelonnek, J.; Kobarg, T.; Lang, R.; Leonhardt, W.; Mellein, D.; Papenfuß, D.; Scherer, T.; Thumm, M.; Wadle, S.; Weggen, J. (2021). High-performance ECRH at W7-X: experience and perspectives. Nuclear fusion, 61 (10), Artk.Nr.: 106005. doi:10.1088/1741-4326/ac1a1b

W7-X Team; Yamaguchi, H.; Satake, S.; Nakata, M.; Shimizu, A.; Suzuki, Y.; Gantenbein, G.; Huber, M.; Illy, S.; Jelonnek, J.; Kobarg, T.; Lang, R.; Leonhardt, W.; Mellein, D.; Papenfuß, D.; Scherer, T.; Thumm, M.; Wadle, S.; Weggen, J. (2021). Optimization of modular and helical coils applying genetic algorithm and fully-three-dimensional B-spline curves. Nuclear fusion, 61 (10), Artikl.Nr.: 106004. doi:10.1088/1741-4326/ac1ae2

W7-X Team; Vuoriheimo, T.; Hakola, A.; Likonen, J.; Brezinsek, S.; Dittmar, T.; Mayer, M.; Prakash Dhard, C.; Naujoks, D.; Tuomisto, F.; Gantenbein, G.; Huber, M.; Illy, S.; Jelonnek, J.; Kobarg, T.; Lang, R.; Leonhardt, W.; Mellein, D.; Papenfuß, D.; Scherer, T.; Thumm, M.; Wadle, S.; Weggen, J. (2021). Deposition of 13C tracer and impurity elements on the divertor of Wendelstein 7-X. Physica scripta, 96 (12), Artkl.Nr.: 124023. doi:10.1088/1402-4896/ac2381

W7-X Team; Feng, Y.; Gao, Y.; Kremeyer, T.; Gradic, D.; Rudischhauser, L.; Fuchert, G.; Bozhenkov, S.; Endler, M.; Jakubowski, M.; Koenig, R.; Krychowiak, M.; Pasch, E.; Hammond, K. C.; Gantenbein, G.; Huber, M.; Illy, S.; Jelonnek, J.; Kobarg, T.; Lang, R.; Leonhardt, W.; Mellein, D.; Papenfuß, D.; Scherer, T.; Thumm, M.; Wadle, S.; Weggen, J. (2021). First attempt to quantify W7-X island divertor plasma by local experiment-model comparison. Nuclear fusion, 61 (10), ArtNr.: 106018. doi:10.1088/1741-4326/ac2025

Shcherbinin, V. I.; Avramidis, K. A.; Pagonakis, I. G.; Thumm, M.; Jelonnek, J. (2021). Large Power Increase Enabled by High-Q Diamond-Loaded Cavities for Terahertz Gyrotrons. Journal of Infrared, Millimeter, and Terahertz Waves, 42, 863–877. doi:10.1007/s10762-021-00814-6

Ell, B.; Pagonakis, I. G.; Wu, C.; Albert, D.; Gantenbein, G.; Illy, S.; Kobarg, T.; Rzesnicki, T.; Thumm, M.; Jelonnek, J. (2021). Mechanical Design Study for Gyrotron E×B Drift Two-Stage Depressed Collector. 2020 IEEE 21st International Conference on Vacuum Electronics (IVEC): 19-22 October 2020, Monterey, CA, USA (online), 187–188, Institute of Electrical and Electronics Engineers (IEEE). doi:10.1109/IVEC45766.2020.9520565

Wagner, D.; Thumm, M. (2021). Improvement of the Output Mode Purity of a Complex-Cavity Resonator for a Frequency-Tunable Sub-THz Gyrotron. IEEE Transactions on Electron Devices, 68 (10), 5220–5226. doi:10.1109/TED.2021.3105955

W7-X Team; Merlo, A.; Böckenhoff, D.; Schilling, J.; Höfel, U.; Kwak, S.; Svensson, J.; Pavone, A.; Lazerson, S. A.; Pedersen, T. S.; Gantenbein, G.; Huber, M.; Illy, S.; Jelonnek, J.; Kobarg, T.; Lang, R.; Leonhardt, W.; Mellein, D.; Papenfuß, D.; Scherer, T.; Thumm, M.; Wadle, S.; Weggen, J. (2021). Proof of concept of a fast surrogate model of the VMEC code via neural networks in Wendelstein 7-X scenarios. Nuclear fusion, 61 (9), Art.-Nr.: 096039. doi:10.1088/1741-4326/ac1a0d

W7-X Team; Killer, C.; Narbutt, Y.; Grulke, O.; Gantenbein, G.; Huber, M.; Illy, S.; Jelonnek, J.; Kobarg, T.; Lang, R.; Leonhardt, W.; Mellein, D.; Papenfuß, D.; Scherer, T.; Thumm, M.; Wadle, S.; Weggen, J. (2021). Turbulent transport in the scrape-off layer of Wendelstein 7-X. Nuclear fusion, 61 (9), Art.-Nr.: 096038. doi:10.1088/1741-4326/ac1ae3

Aiello, G.; Avramidis, K. A.; Franke, T.; Gantenbein, G.; Jelonnek, J.; Meier, A.; Scherer, T.; Schreck, S.; Strauss, D.; Thumm, M.; Tran, M. Q.; Wild, C.; Woerner, E. (2021). Large Area Diamond Disk Growth Experiments and Thermomechanical Investigations for the Broadband Brewster Window in DEMO. IEEE Transactions on Electron Devices, 68 (9), 4669–4674. doi:10.1109/TED.2021.3088077

Girka, I. O.; Thumm, M. (2021). Azimuthal surface waves in low-density plasma loaded, coaxial helix traveling-wave-tube-like waveguides. Voprosy atomnoj nauki i techniki, 134 (4), 24–29. doi:10.46813/2021-134-024

W7-X Team; Lunsford, R.; Killer, C.; Nagy, A.; Gates, D. A.; Klinger, T.; Dinklage, A.; Satheeswaran, G.; Kocsis, G.; Lazerson, S. A.; Nespoli, F.; Pablant, N. A.; Stechow, A. von; Alonso, A.; Andreeva, T.; Beurskens, M.; Biedermann, C.; Brezinsek, S.; Brunner, K. J.; Buttenschön, B.; Carralero, D.; Cseh, G.; Drewelow, P.; Effenberg, F.; Estrada, T.; Ford, O. P.; Grulke, O.; Hergenhahn, U.; Höefel, U.; Knauer, J.; Krause, M.; Krychowiak, M.; Kwak, S.; Langenberg, A.; Neuner, U.; Nicolai, D.; Pavone, A.; Puig Sitjes, A.; Rahbarnia, K.; Schilling, J.; Svensson, J.; Szepesi, T.; Thomsen, H.; Wauters, T.; Windisch, T.; Winters, V.; Zhang, D.; Zsuga, L.; Gantenbein, G.; Huber, M.; Illy, S.; Jelonnek, J.; Kobarg, T.; Lang, R.; Leonhardt, W.; Mellein, D.; Papenfuß, D.; Scherer, T.; Thumm, M.; Wadle, S.; Weggen, J. (2021). Characterization of injection and confinement improvement through impurity induced profile modifications on the Wendelstein 7-X stellarator. Physics of plasmas, 28 (8), Art.-Nr.: 082506. doi:10.1063/5.0047274

W7-X Team; Beidler, C. D.; Smith, H. M.; Alonso, A.; Andreeva, T.; Baldzuhn, J.; Beurskens, M. N. A.; Borchardt, M.; Bozhenkov, S. A.; Brunner, K. J.; Damm, H.; Drevlak, M.; Ford, O. P.; Fuchert, G.; Geiger, J.; Helander, P.; Hergenhahn, U.; Hirsch, M.; Höfel, U.; Kazakov, Y. O.; Kleiber, R.; Krychowiak, M.; Kwak, S.; Langenberg, A.; Laqua, H. P.; Neuner, U.; Pablant, N. A.; Pasch, E.; Pavone, A.; Pedersen, T. S.; Rahbarnia, K.; Schilling, J.; Scott, E. R.; Stange, T.; Svensson, J.; Thomsen, H.; Turkin, Y.; Warmer, F.; Wolf, R. C.; Zhang, D.; Abramovic, I.; Äkäslompolo, S.; Alcusón, J.; Aleynikov, P.; Aleynikova, K.; Ali, A.; Alonso, A.; Anda, G.; Ascasibar, E.; Bähner, J. P.; Baek, S. G.; Balden, M.; Banduch, M.; Barbui, T.; Behr, W.; Benndorf, A.; Biedermann, C.; Biel, W.; Blackwell, B.; Blanco, E.; Blatzheim, M.; Ballinger, S.; Bluhm, T.; Böckenhoff, D.; Böswirth, B.; Böttger, L.-G.; Borsuk, V.; Boscary, J.; Bosch, H.-S.; Brakel, R.; Brand, H.; Brandt, C.; Bräuer, T.; Braune, H.; Brezinsek, S.; Brunner, K.-J.; Burhenn, R.; Bussiahn, R.; Buttenschön, B.; Bykov, V.; Cai, J.; Calvo, I.; Cannas, B.; Cappa, A.; Carls, A.; Carraro, L.; Carvalho, B.; Castejon, F.; Charl, A.; Chaudhary, N.; Chauvin, D.; Chernyshev, F.; Cianciosa, M.; Citarella, R.; Claps, G.; Coenen, J.; Cole, M.; Cole, M. J.; Cordella, F.; Cseh, G.; Czarnecka, A.; Czerski, K.; Czerwinski, M.; Czymek, G.; Molin, A. da; Silva, A. da; Pena, A. de la; Degenkolbe, S.; Dhard, C. P.; Dibon, M.; Dinklage, A.; Dittmar, T.; Drewelow, P.; Drews, P.; Durodie, F.; Edlund, E.; Effenberg, F.; Ehrke, G.; Elgeti, S.; Endler, M.; Ennis, D.; Esteban, H.; Estrada, T.; Fellinger, J.; Feng, Y.; Flom, E.; Fernandes, H.; Fietz, W. H.; Figacz, W.; Fontdecaba, J.; Fornal, T.; Frerichs, H.; Freund, A.; Funaba, T.; Galkowski, A.; Gantenbein, G.; Gao, Y.; García Regaña, J.; Gates, D.; Geiger, B.; Giannella, V.;

Gogoleva, A.; Goncalves, B.; Goriaev, A.; Gradic, D.; Grahl, M.; Green, J.; Greuner, H.; Grosman, A.; Grote, H.; Gruca, M.; Grulke, O.; Guerard, C.; Hacker, P.; Han, X.; Harris, J. H.; Hartmann, D.; Hathiramani, D.; Hein, B.; Heinemann, B.; Helander, P.; Henneberg, S.; Henkel, M.; Hergenhahn, U.; Hernandez Sanchez, J.; Hidalgo, C.; Hollfeld, K. P.; Hölting, A.; Höschen, D.; Houry, M.; Howard, J.; Huang, X.; Huang, Z.; Hubeny, M.; Huber, M.; Hunger, H.; Ida, K.; Ilkei, T.; Illy, S.; Israeli, B.; Jablonski, S.; Jakubowski, M.; Jelonnek, J.; Jenzsch, H.; Jesche, T.; Jia, M.; Junghanns, P.; Kacmarczyk, J.; Kallmeyer, J.-P.; Kamionka, U.; Kasahara, H.; Kasparek, W.; Kenmochi, N.; Killer, C.; Kirschner, A.; Klinger, T.; Knauer, J.; Knaup, M.; Knieps, A.; Kobarg, T.; Kocsis, G.; Köchl, F.; Kolesnichenko, Y.; Könies, A.; König, R.; Kornejew, P.; Koschinsky, J.-P.; Köster, F.; Krämer, M.; Krampitz, R.; Krämer-Flecken, A.; Krawczyk, N.; Kremeyer, T.; Krom, J.; Ksiazek, I.; Kubkowska, M.; Kühner, G.; Kurki-Suonio, T.; Kurz, P. A.; Landreman, M.; Lang, P.; Lang, R.; Langish, S.; Laqua, H.; Laube, R.; Lazerson, S.; Lechte, C.; Lennartz, M.; Leonhardt, W.; Li, C.; Li, C.; Li, Y.; Liang, Y.; Linsmeier, C.; Liu, S.; Lobsien, J.-F.; Loesser, D.; Loizu Cisquella, J.; Lore, J.; Lorenz, A.; Losert, M.; Lücke, A.; Lumsdaine, A.; Lutsenko, V.; Maaßberg, H.; Marchuk, O.; Matthew, J. H.; Marsen, S.; Marushchenko, M.; Masuzaki, S.; Maurer, D.; Mayer, M.; McCarthy, K.; McNeely, P.; Meier, A.; Mellein, D.; Mendelevitch, B.; Mertens, P.; Mikkelsen, D.; Mishchenko, A.; Missal, B.; Mittelstaedt, J.; Mizuuchi, T.; Mollen, A.; Moncada, V.; Mönnich, T.; Morisaki, T.; Moseev, D.; Murakami, S.; Náfrádi, G.; Nagel, M.; Naujoks, D.; Neilson, H.; Neu, R.; Neubauer, O.; Ngo, T.; Nicolai, D.; Nielsen, S. K.; Niemann, H.; Nishizawa, T.; Nocentini, R.; Nührenberg, C.; Nührenberg, J.; Obermayer, S.; Offermanns, G.; Ogawa, K.; Ölmanns, J.; Ongena, J.; Oosterbeek, J. W.; Orozco, G.; Otte, M.; Pacios Rodriguez, L.; Panadero, N.; Panadero Alvarez, N.; Papenfuß, D.; Paqay, S.; Pawelec, E.; Pedersen, T. S.; Pelka, G.; Perseo, V.; Peterson, B.; Pilopp, D.; Pingel, S.; Pisano, F.; Plaum, B.; Plunk, G.; Pölöskei, P.; Porkolab, M.; Proll, J.; Puiatti, M.-E.; Puig Sitjes, A.; Purps, F.; Rack, M.; Récsei, S.; Reiman, A.; Reimold, F.; Reiter, D.; Remppel, F.; Renard, S.; Riedl, R.; Riemann, J.; Risse, K.; Rohde, V.; Röhlinger, H.; Romé, M.; Rondeshagen, D.; Rong, P.; Roth, B.; Rudischhauser, L.; Rummel, K.; Rummel, T.; Runov, A.; Rust, N.; Ryc, L.; Ryosuke, S.; Sakamoto, R.; Salewski, M.; Samartsev, A.; Sanchez, M.; Sano, F.; Satake, S.; Schacht, J.; Satheeswaran, G.; Schauer, F.; Scherer, T.; Schlaich, A.; Schlisio, G.; Schluck, F.; Schlüter, K.-H.; Schmitt, J.; Schmitz, H.; Schmitz, O.; Schmuck, S.; Schneider, M.; Schneider, W.; Scholz, P.; Schrittwieser, R.; Schröder, M.; Schröder, T.; Schroeder, R.; Schumacher, H.; Schweer, B.; Sereda, S.; Shanahan, B.; Sibilia, M.; Sinha, P.; Sipliä, S.; Slaby, C.; Sleczka, M.; Spiess, W.; Spong, D. A.; Spring, A.; Stadler, R.; Stejner, M.; Stephey, L.; Stridde, U.; Suzuki, C.; Szabó, V.; Szabolics, T.; Szepesi, T.; Szökefalvi-Nagy, Z.; Tamura, N.; Tancetti, A.; Terry, J.; Thomas, J.; Thumm, M.; Travere, J. M.; Traverso, P.; Tretter, J.; Trimino Mora, H.; Tsuchiya, H.; Tsujimura, T.; Tulipán, S.; Unterberg, B.; Vakulchyk, I.; Valet, S.; Vanó, L.; Eeten, P. van; Milligen, B. van; Vuuren, A. J. van; Vela, L.; Velasco, J.-L.; Vergote, M.; Vervier, M.; Vianello, N.; Viebke, H.; Vilbrandt, R.; Stechow, A. von; Vorköper, A.; Wadle, S.; Wagner, F.; Wang, E.; Wang, N.; Wang, Z.; Wauters, T.; Wegener, L.; Weggen, J.; Wegner, T.; Wei, Y.; Weir, G.; Wendorf, J.; Wenzel, U.; Werner, A.; White, A.; Wiegel, B.; Wilde, F.; Windisch, T.; Winkler, M.; Winter, A.; Winters, V.; Wolf, S.; Wolf, R. C.; Wright, A.; Wurden, G.; Xanthopoulos, P.; Yamada, H.; Yamada, I.; Yasuhara, R.; Yokoyama, M.; Zanini, M.; Zarnstorff, M.; Zeitler, A.; Zhang, H.; Zhu, J.; Zilker, M.; Zocco, A.; Zoletnik, S.; Zuin, M. (2021). Demonstration of reduced neoclassical energy transport in Wendelstein 7-X. Nature <London>, 596 (7871), 221–226. doi:10.1038/s41586-021-03687-w

W7-X Team; Carralero, D.; Estrada, T.; Maragkoudakis, E.; Windisch, T.; Alonso, J. A.; Beurskens, M.; Bozhenkov, S.; Calvo, I.; Damm, H.; Ford, O.; Fuchert, G.; García-Regaña, J. M.; Pablant, N.; Sánchez, E.; Pasch, E.; Velasco, J. L.; Gantenbein, G.; Huber, M.; Illy, S.; Jelonnek, J.; Kobarg, T.; Lang, R.; Leonhardt, W.; Mellein, D.; Papenfuß, D.; Scherer, T.; Thumm, M.; Wadle, S.; Weggen, J. (2021). An experimental characterization of core turbulence regimes in Wendelstein 7-X. Nuclear fusion, 61 (9), Art.Nr.: 096015. doi:10.1088/1741-4326/ac112f

W7-X Team; Estrada, T.; Maragkoudakis, E.; Carralero, D.; Windisch, T.; Velasco, J. L.; Killer, C.; Andreeva, T.; Geiger, J.; Dinklage, A.; Krämer-Flecken, A.; Wurden, G. A.; Beurskens, M.; Bozhenkov, S.; Damm, H.; Fuchert, G.; Pasch, E.; Gantenbein, G.; Huber, M.; Illy, S.; Jelonnek, J.; Kobarg, T.; Lang, R.; Leonhardt, W.; Mellein, D.; Papenfuß, D.; Scherer, T.; Thumm, M.; Wadle, S.; Weggen, J. (2021). Impact of magnetic islands on plasma flow and turbulence in W7-X. Nuclear fusion, 61 (9), 096011. doi:10.1088/1741-4326/ac146f

W7-X Team; Lazerson, S. A.; Ford, O.; Äkaslompolö, S.; Bozhenkov, S.; Slaby, C.; Vanó, L.; Spanier, A.; McNeely, P.; Rust, N.; Hartmann, D.; Poloskei, P.; Buttenschoϕ B.; Burhenn, R.; Tamura, N.; Bussiahn, R.; Wegner, T.; Drevlak, M.; Turkin, Y.; Ogawa, K.; Knauer, J.; Brunner, K. J.; Pasch, E.; Beurskens, M.; Damm, H.; Fuchert, G.; Nelde, P.; Scott, E.; Pablant, N.; Langenberg, A.; Traverso, P.; Valson, P.; Hergenhahn, U.; Pavone, A.; Rahbarnia, K.; Andreeva, T.; Schilling, J.; Brandt, C.; Neuner, U.; Thomsen, H.; Chaudhary, N.; Höefel, U.; Stange, T.; Weir, G.; Marushchenko, N.; Jakubowski, M.; Ali, A.; Gao, Y.; Niemann, H.; Puig Sitjes, A.; Koenig, R.; Schroeder, R.; den Harder, N.; Heinemann, B.; Hopf, C.; Riedl, R.; Wolf, R. C.; Gantenbein, G.; Huber, M.; Illy, S.; Jelonnek, J.; Kobarg, T.; Lang, R.; Leonhardt, W.; Mellein, D.; Papenfuß, D.; Scherer, T.; Thumm, M.; Wadle, S.; Weggen, J. (2021). First neutral beam experiments on Wendelstein 7-X. Nuclear fusion, 61 (9), 096008. doi:10.1088/1741-4326/ac121c

W7-X Team; Lazerson, S. A.; Pfefferlé, D.; Drevlak, M.; Smith, H.; Geiger, J.; Äkäslompolo, S.; Xanthopoulos, P.; Dinklage, A.; Ford, O.; McNeely, P.; Rust, N.; Bozhenkov, S.; Hartmann, D.; Rahbarnia, K.; Andreeva, T.; Schilling, J.; Brandt, C.; Neuner, U.; Thomsen, H.; Wolf, R. C.; Gantenbein, G.; Huber, M.; Illy, S.; Jelonnek, J.; Kobarg, T.; Lang, R.; Leonhardt, W.; Mellein, D.; Papenfuß, D.; Scherer, T.; Thumm, M.; Wadle, S.; Weggen, J. (2021). Modeling and measurement of energetic particle slowing down in Wendelstein 7-X. Nuclear fusion, 61 (9), 096005. doi:10.1088/1741-4326/ac0771

W7-X Team; Feng, Y.; Jakubowski, M.; König, R.; Krychowiak, M.; Otte, M.; Reimold, F.; Reiter, D.; Schmitz, O.; Zhang, D.; Beidler, C. D.; Biedermann, C.; Bozhenkov, S.; Brunner, K. J.; Dinklage, A.; Drewelow, P.; Effenberg, F.; Endler, M.; Fuchert, G.; Gao, Y.; Geiger, J.; Hammond, K. C.; Helander, P.; Killer, C.; Knauer, J.; Kremeyer, T.; Pasch, E.; Rudischhauser, L.; Schlisio, G.; Sunn Pedersen, T.; Wenzel, U.; Winters, V.; Gantenbein, G.; Huber, M.; Illy, S.; Jelonnek, J.; Kobarg, T.; Lang, R.; Leonhardt, W.; Mellein, D.; Papenfuß, D.; Scherer, T.; Thumm, M.; Wadle, S.; Weggen, J. (2021). Understanding detachment of the W7-X island divertor. Nuclear fusion, 61 (8), 086012. doi:10.1088/1741-4326/ac0772

Stanculovic, S.; Difonzo, R.; Allio, A.; Avramidis, K. A.; Brücker, P.; Gantenbein, G.; Illy, S.; Jelonnek, J.; Kalaria, P. C.; Misko, M.; Rzesnicki, T.; Savoldi, L. (2021). Calibration of the KIT test setup for the cooling tests of a gyrotron cavity full-size mock-up equipped with mini-channels. Fusion engineering and design, 172, Article no: 112744. doi: 10.1016/j.fusengdes.2021.112744

Killinger, A.; Gantenbein, G.; Illy, S.; Ruess, T.; Weggen, J.; Martinez-Garcia, V. (2021). Plasma Spraying of a Microwave Absorber Coating for an RF Dummy Load. Coatings, 11 (7), Article no: 801. doi:10.3390/coatings11070801

Franke, T.; Aiello, G.; Avramidis, K.; Bachmann, C.; Baiocchi, B.; Baylard, C.; Bruschi, A.; Chauvin, D.; Cufar, A.; Chavan, R.; Gliss, C.; Fanale, F.; Figini, L.; Gantenbein, G.; Garavaglia, S.; Granucci, G.; Jelonnek, J.; López, G. S.; Moro, A.; Moscheni, M.; Rispoli, N.; Siccinio, M.; Spaeh, P.; Strauss, D.; Subba, F.; Tigelis, I.; Tran, M. Q.; Tsironis, C.; Wu, C.; Zohm, H. (2021). Integration concept of an Electron Cyclotron System in DEMO. Fusion Engineering and Design, 168, Art.-Nr.: 112653. doi.org/10.1016/j.fusengdes.2021.112653

Avramidis, K. A.; Ioannidis, Z. C.; Illy, S.; Jin, J.; Ruess, T.; Aiello, G.; Thumm, M.; Jelonnek, J. (2021). Multifaceted Simulations Reproducing Experimental Results from the 1.5-MW 140-GHz Preprototype Gyrotron for W7-X. IEEE Transactions on Electron Devices, 68 (6), 3063–3069. doi:10.1109/TED.2021.3075653

W7-X Team; Dreval, M. B.; Brandt, C.; Schilling, J.; Thomsen, H.; Beletskii, A.; Könies, A.; Gantenbein, G.; Huber, M.; Illy, S.; Jelonnek, J.; Kobarg, T.; Lang, R.; Leonhardt, W.; Mellein, D.; Papenfuß, D.; Scherer, T.; Thumm, M.; Wadle, S.; Weggen, J. (2021). Determination of poloidal mode numbers of MHD modes and their radial location using a soft x-ray camera array in the Wendelstein 7-X stellarator. Plasma physics and controlled fusion, 63 (6), Art.-Nr.: 065006. doi:10.1088/1361-6587/abf449

W7-X Team; Corre, Y.; Gaspar, J.; Marsen, S.; Moseev, D.; Stange, T.; Boscary, J.; Drewelow, P.; Gao, Y.; Jakubowski, M.; Hillairet, J.; Laqua, H. P.; Lechte, C.; Moncada, V.; Niemann, H.; Preynas, M.; Puig Sitjes, A.; Gantenbein, G.; Huber, M.; Illy, S.; Jelonnek, J.; Kobarg, T.; Lang, R.; Leonhardt, W.; Mellein, D.; Papenfuß, D.; Scherer, T.; Thumm, M.; Wadle, S.; Weggen, J. (2021). Thermographic reconstruction of heat load on the first wall of Wendelstein 7-X due to ECRH shine-through power. Nuclear fusion, 61 (6), Art.-Nr.: 066002. doi:10.1088/1741-4326/abebea

W7-X Team; Han, X.; Krämer-Flecken, A.; Xiang, H. M.; Vécsei, M.; Knieps, A.; Windisch, T.; Anda, G.; Andreeva, T.; Bozhenkov, S. A.; Geiger, J.; Dunai, D.; Trier, E.; Rahbarnia, K.; Zoletnik, S.; Liang, Y.; Gantenbein, G.; Huber, M.; Illy, S.; Jelonnek, J.; Kobarg, T.; Lang, R.; Leonhardt, W.; Mellein, D.; Papenfuß, D.; Scherer, T.; Thumm, M.; Wadle, S.; Weggen, J. (2021). Application of the elliptic approximation model for the edge turbulence rotation measurement via the poloidal correlation reflectometer in Wendelstein 7-X. Nuclear fusion, 61 (6), Art.-Nr.: 066029. doi:10.1088/1741-4326/abfb15

Haas, D.; Thumm, M.; Jelonnek, J. (2021). Calculations on Mode Eigenvalues in a Corrugated Waveguide with Varying Diameter and Corrugation Depth. Journal of Infrared, Millimeter, and Terahertz Waves, 42 (5), 493–503. doi:10.1007/s10762-021-00791-w

W7-X Team; Endler, M.; Baldzuhn, J.; Beidler, C. D.; Bosch, H.-S.; Bozhenkov, S.; Buttenschön, B.; Dinklage, A.; Fellinger, J.; Feng, Y.; Fuchert, G.; Gao, Y.; Geiger, J.; Grulke, O.; Hartmann, D.; Jakubowski, M.; König, R.; Laqua, H. P.; Lazerson, S.; McNeely, P.; Naujoks, D.; Neuner, U.; Otte, M.; Pasch, E.; Sunn Pedersen, T.; Perseo, V.; Puig Sitjes, A.; Rahbarnia, K.; Rust, N.; Schmitz, O.; Spring, A.; Stange, T.; Stechow, A. von; Turkin, Y.; Wang, E.; Wolf, R. C.; Gantenbein, G.; Huber, M.; Illy, S.; Jelonnek, J.; Kobarg, T.; Lang, R.; Leonhardt, W.; Mellein, D.; Papenfuß, D.; Scherer, T.; Thumm, M.; Wadle, S.; Weggen, J. (2021). Wendelstein 7-X on the path to long-pulse high-performance operation. Fusion engineering and design, 167, Article: 112381. doi:10.1016/j.fusengdes.2021.112381

Girka, I. O.; Pavlenko, I. V.; Thumm, M. (2021). Zeroth radial modes of azimuthal surface waves in dense plasma-loaded, coaxial helix traveling-wave-tube-like waveguides. Physics of plasmas, 28 (4), 043106. doi:10.1063/5.0045139

Ioannidis, Z. C.; Avramidis, K. A.; Rzesnicki, T.; Chelis, I.; Gantenbein, G.; Illy, S.; Jin, J.; Pagonakis, I. G.; Thumm, M.; Jelonnek, J. (2021). Generation of 1.5MW-140GHz pulses with the modular pre-prototype gyrotron for W7-X. IEEE electron device letters, 42 (6), 939–942. doi:10.1109/LED.2021.3073221

W7-X Team; Winters, V. R.; Reimold, F.; König, R.; Krychowiak, M.; Romba, T.; Biedermann, C.; Bozhenkov, S.; Drewelow, P.; Endler, M.; Feng, Y.; Frerichs, H.; Fuchert, G.; Geiger, J.; Gao, Y.; Harris, J. H.; Jakubowski, M.; Kornejew, P.; Kremeyer, T.; Niemann, H.; Pasch, E.; Puig-Sitjes, A.; Schlisio, G.; Scott, E. R.; Wurden, G. A.; Gantenbein, G.; Huber, M.; Illy, S.; Jelonnek, J.; Kobarg, T.; Lang, R.; Leonhardt, W.; Mellein, D.; Papenfuß, D.; Scherer, T.; Thumm, M.; Wadle, S.; Weggen, J. (2021). EMC3-EIRENE simulation of first wall recycling fluxes in W7-X with relation to H-alpha measurements. Plasma physics and controlled fusion, 63 (4), Art.-Nr. 045016. doi:10.1088/1361-6587/abe39c

W7-X Team; Estrada, T.; Carralero, D.; Windisch, T.; Sánchez, E.; García-Regaña, J. M.; Martínez-Fernández, J.; Peña, A. de la; Velasco, J. L.; Alonso, J. A.; Beurskens, M.; Bozhenkov, S.; Damm, H.; Fuchert, G.; Kleiber, R.; Pablant, N.; Pasch, E.; Gantenbein, G.; Huber, M.; Illy, S.; Jelonnek, J.; Kobarg, T.; Lang, R.; Leonhardt, W.; Mellein, D.; Papenfuß, D.; Scherer, T.; Thumm, M.; Wadle, S.; Weggen, J. (2021). Radial electric field and density fluctuations measured by Doppler reflectometry during the post-pellet enhanced confinement phase in W7-X. Nuclear fusion, 61 (4), 046008. doi:10.1088/1741-4326/abddee

W7-X Team; Moseev, D.; Ochoukov, R.; Bobkov, V.; Dendy, R. O.; Faugel, H.; Hartmann, D.; Kallmeyer, J.-P.; Lansky, J.; Laqua, H. P.; Marsen, S.; McClements, K. G.; Nielsen, S. K.; Reintrog, A.; Salewski, M.; Schmidt, B. S.; Schulz, T.; Stange, T.; Gantenbein, G.; Huber, M.; Illy, S.; Jelonnek, J.; Kobarg, T.; Lang, R.; Leonhardt, W.; Mellein, D.; Papenfuß, D.; Scherer, T.; Thumm, M.; Wadle, S.; Weggen, J. (2021). Development of the ion cyclotron emission diagnostic for the W7-X stellarator. Review of scientific instruments, 92 (3), 033546. doi:10.1063/5.0040944

W7-X Team; Schilling, J.; Thomsen, H.; Brandt, C.; Kwak, S.; Svensson, J.; Gantenbein, G.; Huber, M.; Illy, S.; Jelonnek, J.; Kobarg, T.; Lang, R.; Leonhardt, W.; Mellein, D.; Papenfuß, D.; Scherer, T.; Thumm, M.; Wadle, S.; Weggen, J. (2021). Soft x-ray tomograms are consistent with the magneto-hydrodynamic equilibrium in the Wendelstein 7-X stellarator. Plasma physics and controlled fusion, 63 (5), 055010. doi:10.1088/1361-6587/abe0fa

W7-X Team; Weir, G. M.; Xanthopoulos, P.; Hirsch, M.; Höfel, U.; Stange, T.; Pablant, N.; Grulke, O.; Äkäslompolo, S.; Alcusón, J.; Bozhenkov, S.; Beurskens, M.; Dinklage, A.; Fuchert, G.; Geiger, J.; Landreman, M.; Langenberg, A.; Lazerson, S.; Marushchenko, N.; Pasch, E.; Schilling, J.; Scott, E. R.; Turkin, Y.; Klinger, T.; Gantenbein, G.; Huber, M.; Illy, S.; Jelonnek, J.; Kobarg, T.; Lang, R.; Leonhardt, W.; Mellein, D.; Papenfuß, D.; Scherer, T.; Thumm, M.; Wadle, S.; Weggen, J. (2021). Heat pulse propagation and anomalous electron heat transport measurements on the optimized stellarator W7-X. Nuclear fusion, 61 (5), 056001. doi:10.1088/1741-4326/abea55

W7-X Team; Pablant, N. A.; Langenberg, A.; Alonso, J. A.; Bitter, M.; Bozhenkov, S. A.; Ford, O. P.; Hill, K. W.; Kring, J.; Marchuck, O.; Svensson, J.; Traverso, P.; Windisch, T.; Yakusevitch, Y.; Gantenbein, G.; Huber, M.; Illy, S.; Jelonnek, J.; Kobarg, T.; Lang, R.; Leonhardt, W.; Mellein, D.; Papenfuß, D.; Scherer, T.; Thumm, M.; Wadle, S.; Weggen, J. (2021). Correction and verification of x-ray imaging crystal spectrometer analysis on Wendelstein 7-X through x-ray ray tracing. Review of scientific instruments, 92 (4), Article no: 043530. doi:10.1063/5.0043513

Ruess, T.; Avramidis, K. A.; Gantenbein, G.; Illy, S.; Rzesnicki, T.; Thumm, M.; Jelonnek, J. (2021). Theoretical Study on the Possibility for Stepwise Tuning of the Frequency of the KIT 2 MW 170/204 GHz Coaxial-Cavity Gyrotron. 2020 45th International Conference on Infrared, Millimeter, and Terahertz Waves (IRMMW-THz), 8-13 November 2020, online, 435–436, Institute of Electrical and Electronics Engineers (IEEE). doi:10.1109/IRMMW-THz46771.2020.9370801

Illy, S.; Avramidis, K. A.; Ioannidis, Z. C.; Aiello, G.; Benin, P.; Chelis, I.; Dinklage, A.; Gantenbein, G.; Jelonnek, J.; Jin, J.; Laqua, H. P.; Leggieri, A.; Legrand, F.; Marek, A.; Marsen, S.; Pagonakis, I. G.; Ruess, T.; Rzesnicki, T.; Scherer, T.; Strauss, D.; Thumm, M.; Tigelis, I.; Wagner, D.; Weggen, J.; Wolf, R. C. (2021). Recent Development of a 1.5 MW, 140 GHz Continuous-Wave Gyrotron for the Upgraded ECRH System at W7-X. 2020 45th International Conference on Infrared, Millimeter, and Terahertz Waves (IRMMW-THz), Buffalo, NY, USA, 8-13 Nov. 2020, 1–2, Institute of Electrical and Electronics Engineers (IEEE). doi:10.1109/IRMMW-THz46771.2020.9370666

Ioannidis, Z. C.; Rzesnicki, T.; Avramidis, K. A.; Gantenbein, G.; Illy, S.; Jin, J.; Krier, L.; Pagonakis, I. G.; Ruess, S.; Schmid, M.; Thumm, M.; Jelonnek, J. (2021). Operation of the Modular KIT 170 GHz – 2 MW Longer-Pulse Coaxial-Cavity Gyrotron with Pulses up to 50 ms. 2020 45th International Conference on Infrared, Millimeter, and Terahertz Waves (IRMMW-THz), Buffalo, NY, USA, 8-13 Nov. 2020, 01–02, Institute of Electrical and Electronics Engineers (IEEE). doi:10.1109/IRMMW-THz46771.2020.9370698

Haas, D.; Thumm, M. (2021). Design Procedure for a Broadband TE11/HE11 Mode Converter for High-Power Radar Applications. Journal of Infrared, Millimeter, and Terahertz Waves. doi:10.1007/s10762-021-00773-y

Avramidis, K. A.; Ioannidis, Z. C.; Aiello, G.; Bénin, P.; Chelis, I.; Dinklage, A.; Gantenbein, G.; Illy, S.; Jelonnek, J.; Jin, J.; Laqua, H. P.; Leggieri, A.; Legrand, F.; Marek, A.; Marsen, S.; Pagonakis, I. G.; Ruess, T.; Rzesnicki, T.; Scherer, T.; Strauss, D.; Thumm, M.; Tigelis, I.; Wagner, D.; Weggen, J.; Wolf, R. C. (2021). Towards a 1.5 MW, 140 GHz gyrotron for the upgraded ECRH system at W7-X. Fusion engineering and design, 164, Art.-Nr.: 112173. doi.org/10.1016/j.fusengdes.2020.112173

Tkachova, T. I.; Shcherbinin, V. I.; Tkachenko, V. I.; Ioannidis, Z. C.; Thumm, M.; Jelonnek, J. (2021). Starting currents of modes in cylindrical cavities with mode-converting corrugations for second-harmonic gyrotrons. Journal of infrared, millimeter, and terahertz waves. doi:10.1007/s10762-021-00772-z

Aiello, G.; Avramidis, K. A.; Gantenbein, G.; Jelonnek, J.; Jin, J.; Laqua, H. P.; Meier, A.; Scherer, T.; Strauss, D.; Thumm, M. (2021). Design verification of the gyrotron diamond output window for the upgrade of the ECRH system at W7-X. Fusion engineering and design, 165, Article no: 112262. doi.org/10.1016/j.fusengdes.2021.112262

Shcherbinin, V. I.; Avramidis, K. A.; Thumm, M.; Jelonnek, J. (2021). Mode Discrimination by Lossy Dielectric Rods in Cavities of Second-Harmonic Gyrotrons. Journal of infrared, millimeter, and terahertz waves, 42 (1), 93–105. doi:10.1007/s10762-020-00760-9

Haas, D.; Thumm, M.; Jelonnek, J. (2021). Broadband Rotary Joint Concept for High-Power Radar Applications. Journal of infrared, millimeter, and terahertz waves, 42 (2), 107–116. doi:10.1007/s10762-020-00766-3.

2 Materials and Technologies for the Energy Transition (MTET): - Bioenergy, Concentrated Solar Power and High Temperature Storage -

Contact: Prof. Dr. Georg Müller

The Department for Pulsed Power Technology is focusing on research and development of pulsed power technologies and related applications. The applications involve the electroporation of biological cells for extraction of cell contents (PEF- process), dewatering and drying of green biomass, pre-treatment of micro algae for energetic use and sustainable reduction of bacteria in contaminated effluents. Another key research topic is devoted to the development of corrosion barriers and materials for improved compatibility of structural materials in contact with liquid metal coolants, for use in transmutation systems, in the field of concentrated solar thermal energy, high-temperature storage, liquid metal batteries and methane reforming.

In 2021:

- Basic research to establish cascade processes for extracting valuable substances from microbial biomass has made significant progress. The previously evaluated extraction method using PEF treatment with a subsequent incubation step led to inactivation of cells with a specific treatment energy reduced by a factor of 100. A so-called 'cell death-indicated factor' could be determined, which can be extracted as a reaction to the PEF treatment. Application of this extract to untreated recipient cells increases efficiency in protein extraction from microalgae.
- A modified process chain was introduced envolving PEF treatment, incubation followed by a direct transesterification process to generate fatty acid methyl ester (“biodiesel”). This direct transesterification process step allows to bypass the usual lipid extraction steps as one of the most energy-intensive steps in microalgae downstream processing.
- Material development and characterization with the aim of improving compatibility with the liquid metals Pb, PbBi, Zn and Na were pushed ahead. Initial compatibility tests of nickel-based alloys in sodium at temperatures > 600 °C show the usability of this group of materials in principle. The inductively heated high-temperature cycling test stand with flowing sodium was optimized using COMSOL simulations and should also be able to be used for tests with 3D-printed receivers in the future.
- As part of the third-party funded project LIMELISA, a large number of different industrially relevant materials that can be used for the construction of pumps and valves were tested in lead at temperatures of up to 700 °C in consultation with an industrial partner.
- Surface aluminization using pack cementation and pre-oxidation is a possibility to use commercial materials such as T91 at temperatures above 700 °C in Pb and also in solar salts. The usability of ceramic materials as reactor material for CO2-free hydrogen production from methane in Zn could be confirmed up to 1100 °C (third-party funded project DECAGAS).
- Charging and discharging cycles with sodium-based liquid metal batteries, which are being developed as part of a DFG project, show the high efficiency of this battery type.

2.1 PEF-Processing of Microbial Biomass

Contact: Dr. Wolfgang Frey

2.1.1 SABANA-Project: Adaption of the KEA-facility to Microalgae Processing

Involved Staff: Dr. R. Fetzer, D. Herzog, J. Fleig, K. Leber, PD Dr. M. Sack, Dr. W. Frey

A major objective of the EU-Project SABANA is to demonstrate microalgae processing at large-scale. For PEF-processing, a mass-flow of 500 l/h and higher and a specific treatment energy of 150 kJ/l are required. So far, the KEA-facility operated at a specific treatment energy of 80 kJ/l at maximum.

To identify a potential thermal overload of the treatment chamber, a thermal stress analysis by CFD simulation was performed. For analysis, the simulation software COMSOL Multphysics was applied. For a treatment energy of 1.5 MJ/kg_{dw} and a mass-flow of 500 l/h at 100 g_{dw}/l, the time-dependent heat transfer and the resulting values of von Mises stress in the treatment chamber material were calculated. A maximum value of von Mises stress of 22 MPa was obtained at the biomass outlet channel (marked by an arrow) after 17 min of continuous operation, Fig. 2.1.1. This is close to the maximum allowable value of 23 MPa for Polypropylen.

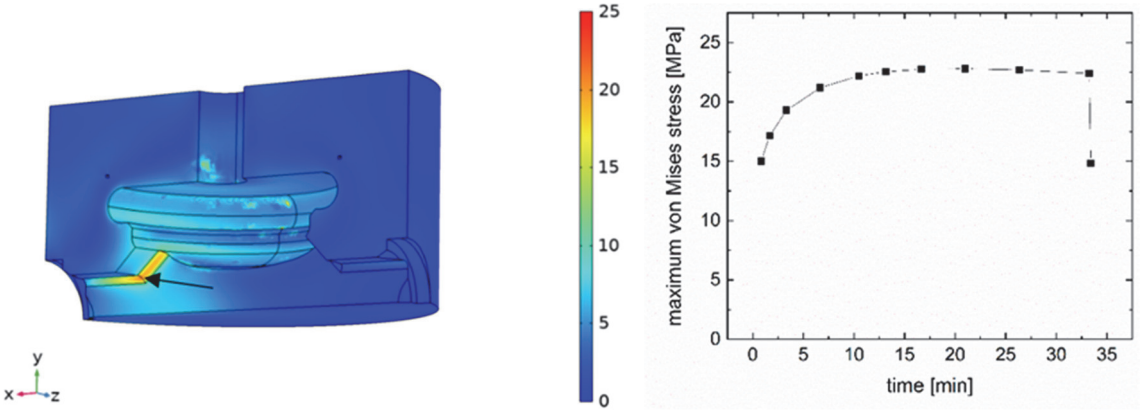

Fig. 2.1.1: Identification of critical thermally induced stress points (arrow, left) in the PP-housing of the KEA treatment chamber. Stationary values can be expected 17 minutes after start of operation, right.

As a solution, the sharp edge along the outlet channel was rounded by a radius of R = 10 mm, which reduced the von Mises stress value at that point to less than 17 MPa. A new treatment chamber with optimized geometry including electrodes and material feed was manufactured and integrated into the KEA- facility.

After assembly, a fatigue test at 110 % of nominal maximum treatment energy (1.1 x 150 kJ/ltr) was performed with model medium at a conductivity of 3 mS/cm and a mass flow of 450 ltr/h. Test duration was 40 min. Stationary temperature conditions were observed after 20 min of operation. As theoretically expected the temperature rise in the treated medium was ΔT = 39 K. The facility passed the fatigue test without any failure.

Fig. 2.1.2: New treatment chamber integrated into the PEF Demo-facility, right, and setup for the fatigue test at the technicum at KIT-IHM, left.

2.1.2 PEF-Assisted Extraction of Valuable Compounds from Chicory

Involved Staff: Dr. Ch. Gusbeth, Dr. W. Frey

Pulsed electrical field technology has been used successfully at the IHM over the past decade to extract valuable compounds such as lipids and proteins from microalgae biomass. The extraction of sugar from sugar beets and the pretreating of wine mash to improve wine production are other well-known applications of the PEF technology that have been demonstrated in our institute. Based on this long-term experience, a new application was proposed within the framework of the collaboration with the Food Pilot Lab at Flanders Research Institute for Agriculture, Fisheries and Food (ILVO) at Melle, Belgium. A collaborative experimental project for the determination of the efficiency of PEF treatment for recovery of ingredients from Belgian Endive roots was started.

The Belgian Endive (genus Cichorium), which is grown in the dark to produce a white lettuce plant, has gained great popularity in Belgium and the Netherlands in recent years, while the roots are industrially processed for inulin extraction. First and foremost, the extraction of antioxidants, phenolic components, sesquiterpene lactones and sugars was investigated. Studies of folk medicines implicate sesquiterpene lactones as the active ingredient in treatments for ailments such as diarrhea, burns, influenza, and neuro-degradation.

The study was carried out at the beginning of summer during harvesting time of chicory. Small slices (0.5 x 1.0 x 2.0 cm) of chicory roots of the variety Flexine and Sweet Lady were PEF treated in a batch chamber with a volume of 80 ml and plane parallel electrode geometry. Extracts from PEF treated chicory showed higher antioxidative capacity in comparison to untreated/control samples. PEF treatment, and longer extraction time considerably improve extraction and result in higher sugar content especially sucrose and fructose in extracts. The total phenol content increases up to 7 times after the PEF treatment. The samples obtained after short incubation time, post PEF treatment, have a higher purity in terms of antioxidative activity. The content of sesquiterpene lactones was lower in the PEF extracts as control samples. Since the results are very promising, discussions about industrial cooperation are currently underway. In addition, a new treatment chamber has been developed that enables larger amounts of biomass (for instance complete chicory roots) to be treated.

2.1.3 PEF Treatment Extracts a Cell-Death Inducing Factor from Chlorella Vulgaris in Stationary Phase

Involved Staff: M.Sc. D. Krust, Dr. Ch. Gusbeth

This year the basic research regarding establishment of cascade processing for the valorization of microalgae biomass has made clear progress. The already evaluated extraction method via PEF treatment followed by an incubation step led to inactivation of cells with a specific treatment energy reduced by a factor of hundred.

The major findings include a thorough phenomenological study of the cell-death inducing factor that can be extracted in response to PEF treatment. The potency of this factor is tested by incubating recipient cells that have not been directly subjected to PEF treatment. The cell-death inducing factor is generated by the microalgae *C. vulgaris* predominantly in stationary phase from 4-7 days post inoculation (dpi, see Fig. 2.1.3) and could be shown to be heat-labile and dose-dependent. Since the responsiveness of recipient cells (as well as the release of this factor by donor cells) depends on the cell cycle stage, the induced cell death must involve a biological process. In the next step the cell-death inducing factor needs to be identified so that the signal pathways can be elucidated. Concerning the signal pathway in the recipient cells, involvement of the MAP kinase cascade is plausible due to the tight link with the cell cycle.

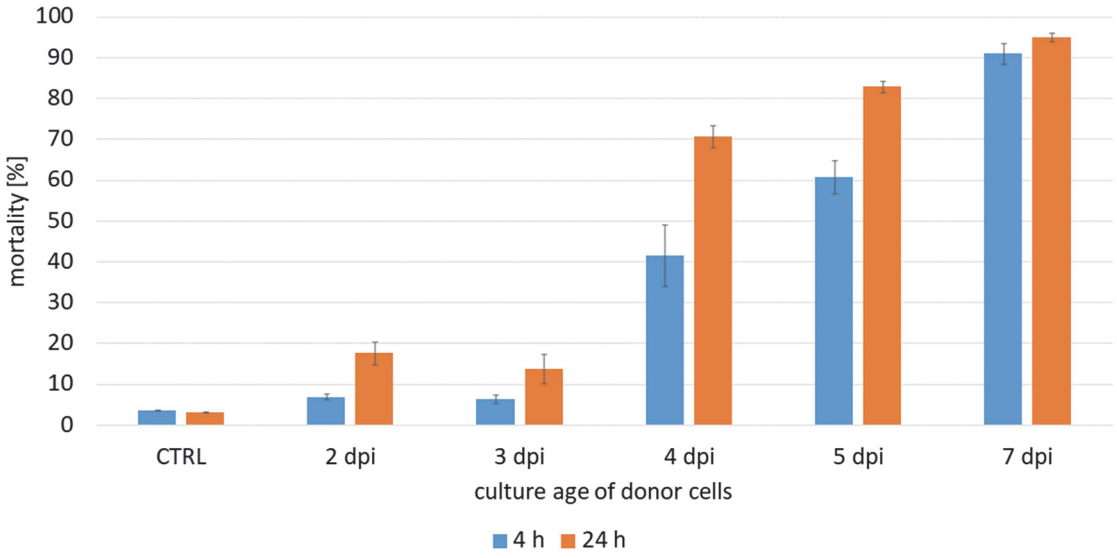

Fig. 2.1.3: Cell mortality of recipient cells after addition of extract from cultures sampled at different time points of the growth curve. Extracts from donor cells were generated by concentration to a high cell density (7 mg·ml^{-1}), PEF treatment with a specific energy of 8.0 J·ml^{-1} and incubation for 24 h. After centrifugation, the water-soluble extracts were added to live recipient cells and viability was monitored at 4 h and 24 h via fluorescence dye (FDA assay). CTRL: control sample with addition of untreated extract, dpi = days post inoculation.

The biotechnological application allows to administer PEF treatment at low energies with already saturated protein recovery efficiency, presenting an energy-efficient and sustainable way of protein extraction possibly connected to contribution of the cell-death inducing factor.

2.1.4 Impact of Incubation Time on Availability of Total Organic Carbon with PEF-Treated Microalgae *Auxenochlorella Protothecoides* for Final Anaerobic Digestion (AD)

Involved Staff: R. Wüstner, N. Nazarova, K. Leber, Dr. A. Silve, Dr. I. Papachristou, DI R. Strässner

Anaerobic digestion of residual microalgal biomass turned out to be a promising final step in complete utilization of microalgal biomass. The extraction of microalgal valuables from microalgae *Auxenochlorella protothecoides* (*A. protothecoides*) and final generation of biogas from different previously exploited microalgae preparations (containing approx. 73-95 % bio methane), was reported earlier (data published in IHM annual report 2019 and 2020). Hereafter the part of organic carbon in the AD-process, with different used microalgae preparations will be presented.

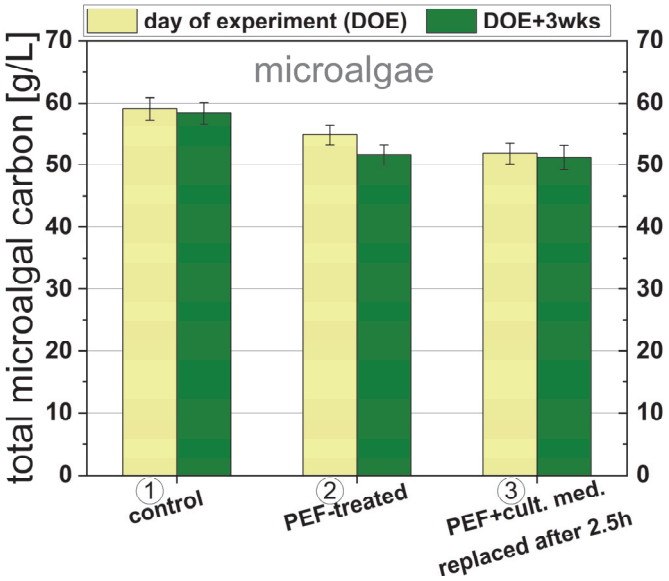

Fig. 2.1.4: Total carbon concentration of microalgae, depending on incubation time (0 d and 3 wks) of microalgae *A. protothecoides*.

For the anaerobic microorganisms, an easy availability of the anaerob digestable components in the substrate, is very important for an effective AD. Organic carbon e.g., representing 24 % of the CDW of the microalgal biomass in our investigations, is available in different modifications, demonstrating significant variations regarding accessability. Carbon is one of the main building blocks for the synthesis of methane (CH4). Using microalgae suspension as substrate for anaerobic digestion, carbon is present inside microalgal cells (solid phase) and in the extracellular medium (liquid phase). These two fractions are different regarding carbon content and accessibility. The easy access to the organic carbon solved in the extracellular medium is granted, due to the lack of shielding by cell membrane and cell wall. Carbon inside microalgal cells is not instantly available for anaerobic microorganisms, because two barriers need to be overcome, cell wall and cell membrane. Additionally, despite the fact that it contains big amounts of carbon, the cell wall of many green microalgae is hard to penetrate and to hydrolyze for anaerobic microorganisms. This is due to the composition of the cell wall, comprising mainly of cellulose, hemicellulose, pectin, other polysaccharides and glycoproteins; therefore, it is rather recalcitrant against hydrolysis in the first step of AD according to previous studies with *Chlorella sp.* and other green microalgae. The cell membrane, as second barrier, is comparatively easy to penetrate and to hydrolyze.

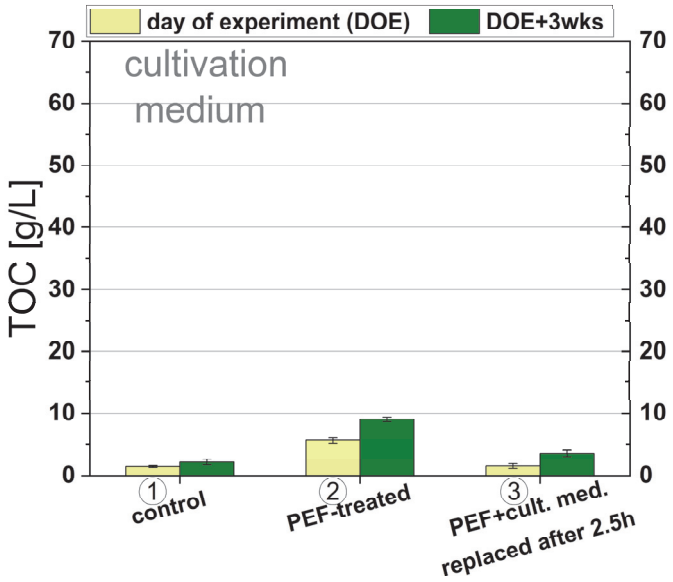

Fig. 2.1.5: Total organic carbon concentration of cultivatrion medium, depending on incubation time (0 d and 3 wks) of microalgae *A. protothecoides*.

Fig. 2.1.4 and Fig. 2.1.5 show the carbon content of the microalgae and of the extracellular medium for samples (1) to (3). It can be seen that PEF-treatment (sample 2) induces a release of about 5 % of organic carbon from microalgal cells, compared to control (sample 1) (Fig. 2.1.4). In the course of the incubation period of three weeks (3 wks) after corresponding day of experiment (DOE), all microalgae samples began to hydrolyze. This effectuates a further reduction of the carbon content inside the microalgal cells (Fig. 2.1.4) and therefore an increase of the total organic carbon (TOC) content in the extracellular medium (Fig. 2.1.5). This effect is more visible on PEF treated samples (2) than on the control samples (1), although some hydrolysis of the biomass is also taking place in the control (1). PEF-treated sample (2) reveals the biggest amount of microalgal carbon available in the extracellular medium on the day of the experiment and after the incubation period of three weeks. Sample (3), with no surprise, has less carbon available in the extracellular medium, since it underwent an aqueous extraction. After PEF-treatment of sample (3), the medium, containing most of the released organic carbon, was removed and replaced by deionized water. Overall, PEF-treatment contributes to a more effective liberation of microalgal ingredients, which is even boosted by the three-weeks incubation period. Quantitatively, the control sample (1) supplies easily accessible TOC at ~ 2 g/L in the extracellular medium. PEF treated sample (2) provides approx. 9 g/L and the PEF treated preparation with subsequent aqueous extraction (3), still 3.5 g/L (Fig. 2.1.5). Located inside microalgal cells and in the cell wall, is a much bigger carbon reservoir, amounting between 50 and 60 g/L (Fig. 2.1.4), with delayed access and even partially inaccessible.

2.1.5 Energetic Valorization of Microalgae by Combination of PEF Treatment and Direct Transesterification

Involved Staff: Dr. I. Papachristou, R. Wüstner, N. Nazarova, Dr. A. Silve, Dr. W. Frey

Because of their ability to produce large quantities of triglycerides, microalgae are a promising source for biodiesel production. Different processes are studied that would allow this energetic use. The most classical way consists in extracting lipids and performing a transesterification reaction subsequently to obtain biodiesel in the form of FAMEs. This approach is hampered by the difficulty to perform the lipid extraction accompanied by high economic and energy costs. One of the major constraints is, that the extraction must be done on wet microalgae to avoid exorbitant costs for drying. Furthermore, the extraction capacity of solvents is generally strongly decreased in aqueous environment. Additionally, the recycling of high volumes of solvents after lipid extraction causes prohibitive costs.

The direct transesterification process avoids the lipid extraction step and allows to obtain FAMEs in a single step. In the framework of our research on renewable energies, we have evaluated this approach on the microalgae *Auxenochlorella protothecoides (A. protothecoides)*, cultivated in our laboratory and processed wet, directly after harvesting. The main objective of this study was to evaluate the efficiency of this approach, without pre-treatment or in combination with PEF-pre-treatment. It was compared to the standard approach i.e. lipid extraction followed by transesterification. The tested processing routesare depicted in Fig. 2.1.6.

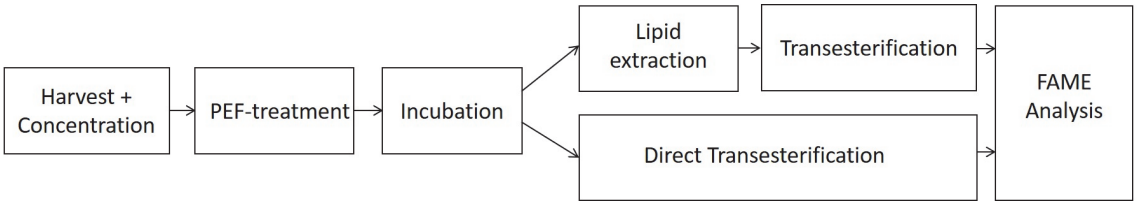

Fig. 2.1.6: Two possible routes to produce FAMEs from microalgae. The direct transestherification process enables to bypass the lipid extraction, one of the most energy intensive step of downstream processing of microalgae.

Results obtained on autotrophic microalgae are displayed on Fig. 2.1.7. Fig. 2.1.7, A, represents the FAME yields obtained after lipid extraction followed by transesterification. Note, that only results obtained with PEF-treated samples are shown, since for control samples the lipid extraction was not efficient enough to perform the subsequent transesterification of the lipids. When this route is applied directly after PEF-treatment, it is not efficient when using a PEF-treatment energy of 0,25 MJ/kg_{DW}, while it enables to achieve FAME yield of 20 $\%_{DW}$ when an energy of 1,5 MJ/kg_{DW} is used i.e. approximately half of the FAME yield obtained with the reference method.

If an incubation period of 24 h is added between PEF treatment and lipid extraction, the FAME yields are increased and achieve 27 $\%_{DW}$ and 32 $\%_{DW}$ for the PEF energies of 0,25 MJ/kg_{DW} and 1,5 MJ/kg_{DW}, respectively. The results of the alternative direct transesterification are displayed in Fig. 2.1.7, B. Immediately after PEF-treatment, the yield obtained after the direct transesterification of microalgae not treated or PEF-treated with 0,25 MJ/kg_{DW} is slightly above 10 $\%_{DW}$ and reaches 23 $\%_{DW}$ when the applied energy is 1,5 MJ/kg_{DW}. If an incubation period of 24h is included into the processing route, the yield remains low for non-treated microalgae but achieves 37 $\%_{DW}$ for PEF treated microalgae for both tested specific energy values. For that case, the FAME yield well matches the values obtained after processing according to the reference method, i.e. transesterification of lyophilized and bead-milled microalgae biomass.

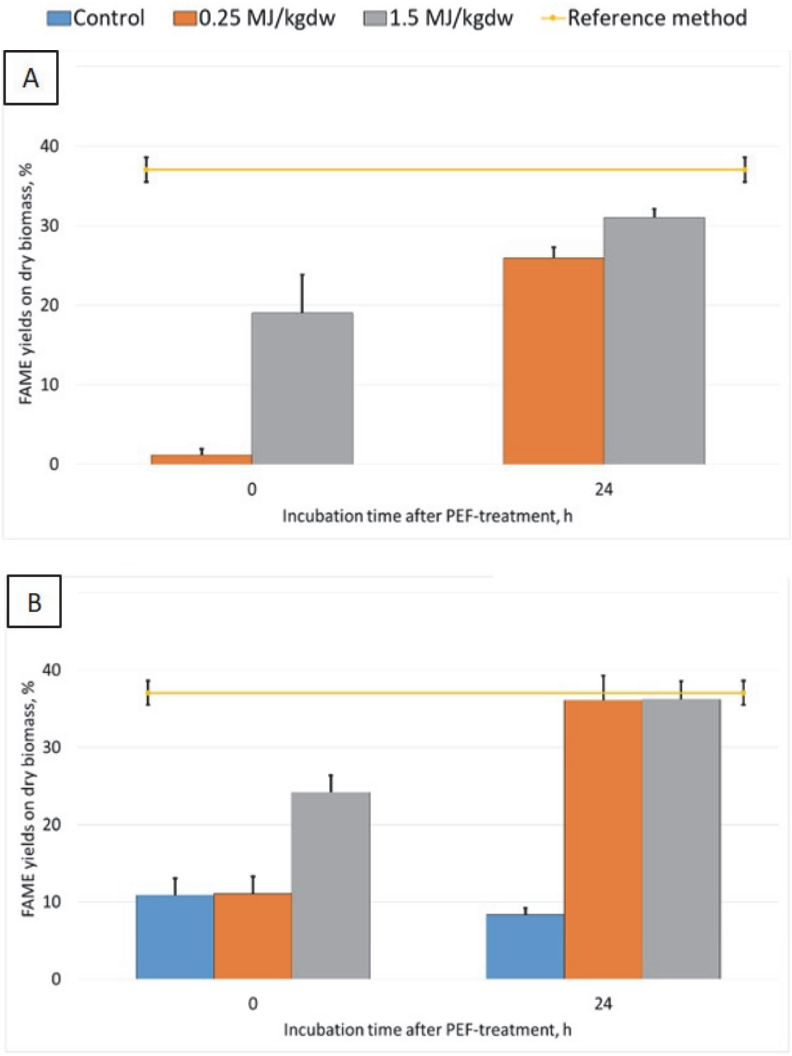

Fig. 2.1.7: Comparison of the efficiency of two routes for FAME production: FAME yields after extraction of lipids followed by transesterification (A). FAME recovery after direct transesterification of the microalgae (B). The lipid extraction and the direct transesterification were performed on freshly harvested microalgae *A. protothecoides* after PEF-treatment with 0.25 MJ/kg_{DW} or 1.5 MJ/kg_{DW}, either directly after PEF-treatment or after an incubation step of 24 h under inert conditions. FAME yields were assessed by gas chromatography. The reference method consisted in applying the transesterification protocol on lyophilized, bead-milled biomass. Results are the average ± std of two independent cultivations.

From the above-mentioned results, it appears, that direct transesterification applied after PEF-treatment and an incubation enables to achieve high FAME yields, which corresponds well with the highest yield detected with the reference method. This approach is therefore very well suited for energetic applications. Avoiding the extraction step completely suppresses the problematic of solvent recycling. Only methanol, used for transesterification, needs to be coped with.

Surprisingly the direct process was extremely successful on *A. protothecoides* cultivated autotrophically, but not when cultivated mixotrophically. Investigating the reasons for these differences will be one of the next objectives. Efforts will also be focused on improving the transesterification process by reducing processing temperature and also the molar ratio of triglycerides to methanol which is currently around 1:300, i.e. 100 times higher than the stochiometric ratio.

2.2 Components and Electroporation Processes

Contact: PD Dr. Martin Sack

2.2.1 Semiconductor-Based Marx-Type Pulse Generator for PEF-treatment of Potatoes

Involved Staff: PD Dr. M. Sack, D. Herzog, J. Fleig

For the PEF-treatment of potatoes in industrial scale a Marx-type pulse generator equipped with IGBT switches is under development. The generator features a stage voltage of up to 1 kV and a peak pulse current of up to 500 A into an RLC pulse circuit. A generator comprising 8 stages has been assembled and is currently being tested. As the generator will be operated in groud-symmetric configuration, it has been split into two stacks, each consisting of four stage modules and grounded at its center terminal. In the course of the continuing tests, the generator has been operated connected to an artificial load at a stage voltage of 1 kV, a pulse repetiton rate of 500 Hz, and a peak current of 540 A, which is slightly above the rated current of the modules. Fig. 2.2.1 shows the output voltages measured versus ground and currents at the terminals of both stacks. The inductance of the pulse circuit and the total discharge of the pulse capacitors during the pulse both enable energy-efficient soft switching during turn-on and turn-off of the switches. Fig. 2.2.2 shows voltages and currents when closing the pulse switches. The output voltage rises within approximately 100 ns. The generator design involves cooling of the power semiconductors by means of natural convection of air. Fig. 2.2.3 shows a photo and a thermographic image of one stack of four stages which has been taken after 4.5 h of continuous operation at a total power of 9.7 kW, i.e. 1.2 kW per stage. The temperatures of the power semiconductors remained within acceptable limits. Further activities will be devoted to the setup of a larger generator stack.

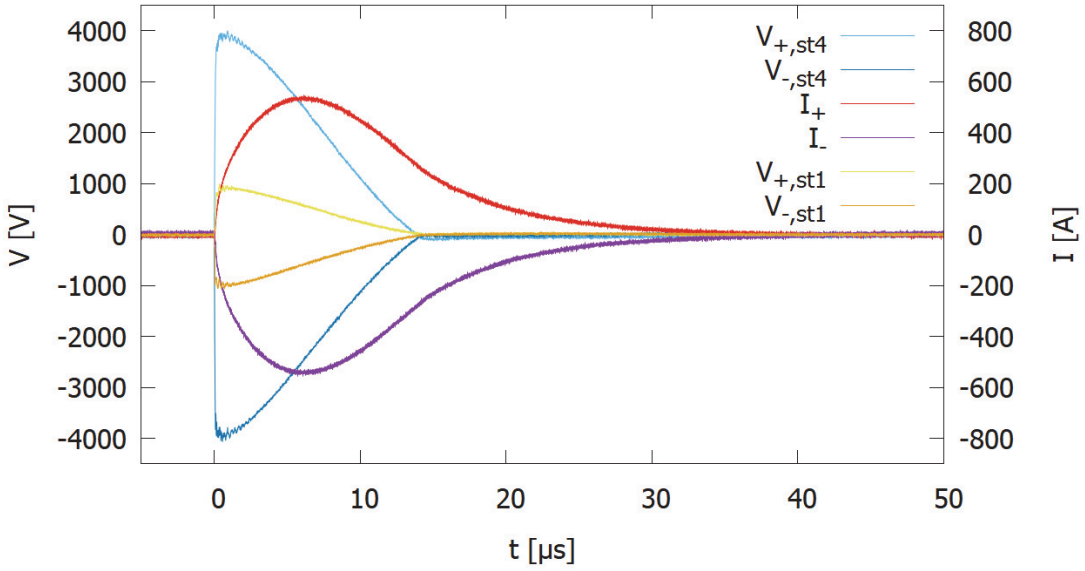

Fig. 2.2.1: Ground-symmetric operation of 8 stages at Vstage = 1 kV and frep = 500 Hz: Voltages and currents at the genertor's positive and negative output terminal and at the outputs of both ground-side stages.

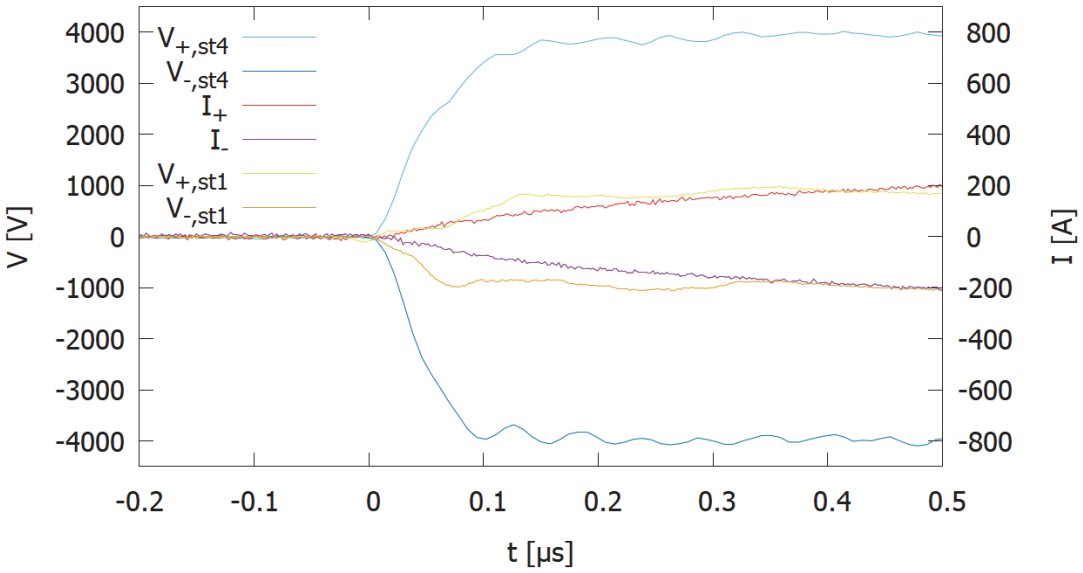

Fig. 2.2.2: Ground-symmetric operation of 8 stages at Vstage = 1 kV and frep = 500 Hz: Closing of the pulse switches under soft-switching conditions.

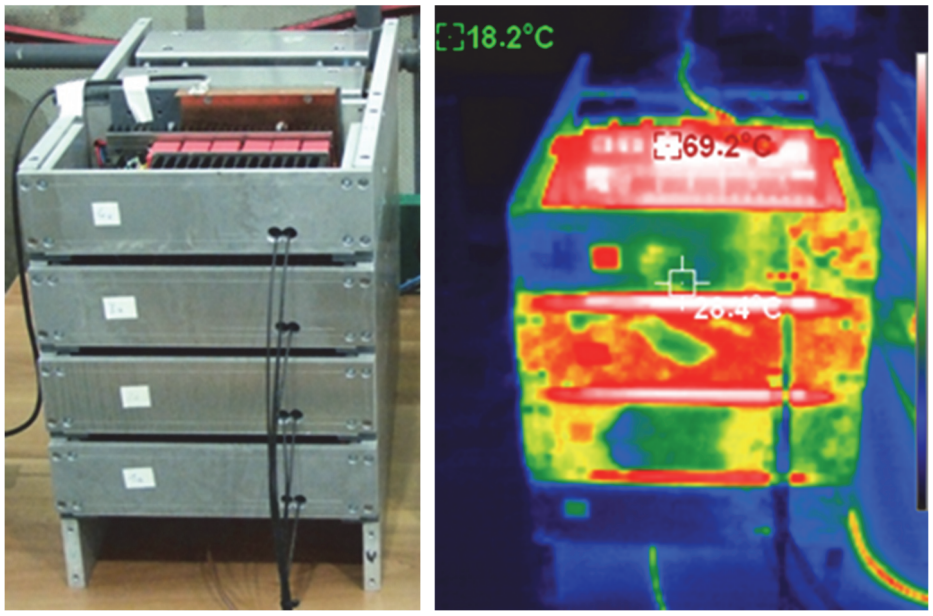

Fig. 2.2.3: Photo and thermographic image of one stack of four stages after 4.5 h of continuous operation at a total power of 9.7 kW, i.e. 1.2 kW per stage.

2.2.2 Fast SiC-MOSFET Switch

Involved Staff: PD Dr. M. Sack, D. Herzog, J. Fleig

Pulse generators featuring a fast rise of the voltage enable energy-efficient switching due to a reduction of the switching losses. In order to study the gate-boosted operation of SiC MOSFETs, a test setup comprising a gate-boosting circuit featuring two GaN-HEMTs in half-bridge configuration driving three paralleled SiC MOSFETs has been designed and operated. Fig. 2.2.4 shows the simplified schematic and a photo of the test setup.

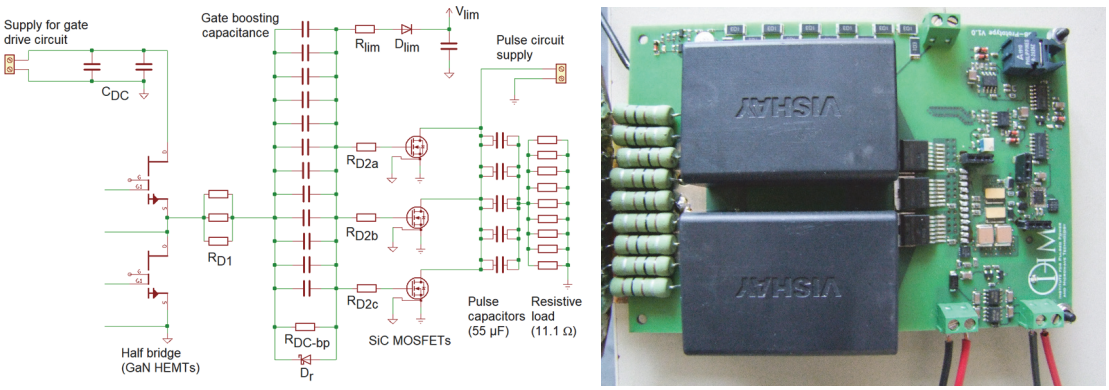

Fig. 2.2.4: Gate-boosting circuit featuring GaN-HEMTs in half-bridge configuration driving three paralleled SiC MOSFETs.

For the shown configuration, with a supply voltage of 150 V to the gate drive circuit and a supply voltage to the pulse circuit of 500 V and 1000 V, the voltage at the resistive load rises within 2.5 ns and 3.3 ns (10 % to 90 %), respectively. Fig. 2.2.5 shows the measured voltages at one SiC MOSFET and across the load.

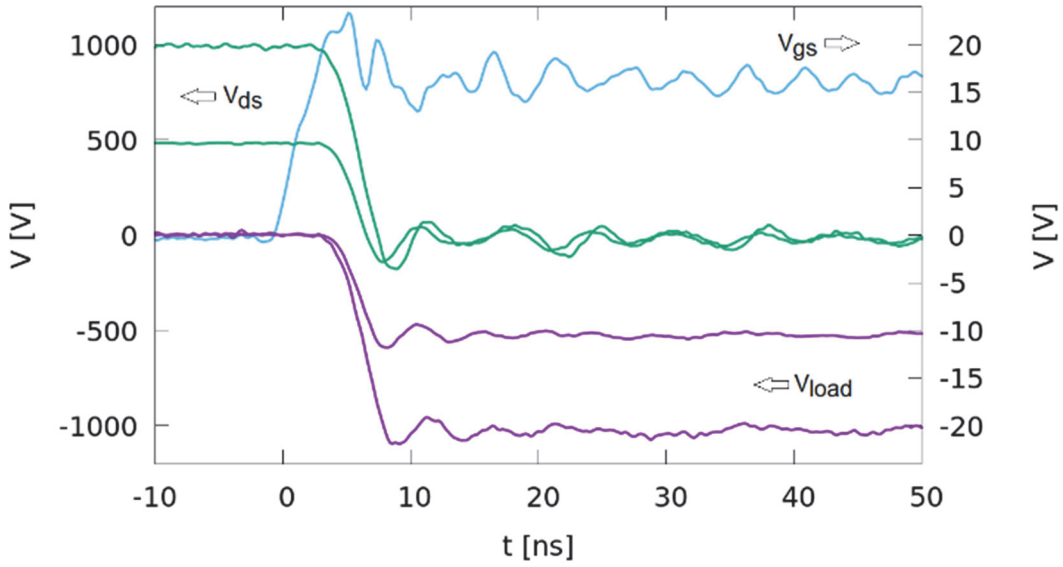

Fig. 2.2.5: Vgs, Vds, and Vload with gate boosting, charging voltage 500 V and 1000 V. (gate-boosting capacitance: 816 pF, driving voltage: 150 V).

2.3 Concentrating Solar Power (CSP) and High Temperature Thermal Storage / Liquid Metal – Material Compatibility

Contact: Dr. Alfons Weisenburger

Liquid metals as advanced heat-transfer (HTM) and storage media for CSP and other high temperature technologies are a promising research area that will result in performance and efficiency increase and reduced costs. Within LIMCKA (Liquid Metal Competence Center KArlsruhe) several institutes and laboratories of the KIT combine their long-standing experience and specific expertise in material research, system engineering, safety and thermal-hydraulics to tackle all relevant aspects of liquid metals as HTM. The IHM focuses on compatibility research by surface optimization of existing materials using GESA and development of new materials that are able to mitigate corrosion in contact with liquid metals and salts. Liquid metal batteries are a further research area where the expertise of the IHM and DLR is combined with the expertise of a Chinese university (HUST) to explore Sb-Bi(Sn)/Na based low cost liquid metal battery concepts in the frame of a German-Chinese DFG project. The technical feasibility and scaling of CO_2-free methane pyrolysis in liquid high-temperature Sn (> 1000 °C) is investigated as part of the DECAGAS project together with ITES and WINTERSHALL-DEA. Components (valves, pumps) for a high temperature storage based on liquid Pb are under investigation in the BMWi funded project LIMELISA together with the ITES, DLR and coordinated by the company KSB. In this project IHM investigates the compatibility of materials in Pb up to 700 °C and propose potential candidates for the manufacturing of pumps and valves to be used in such conditions.

Some of the tasks are embedded in European projects, the EERA-CSP and cooperations like with DLR and HUST via the DFG or with KSB and DLR via the BMWi or in a direct industrial cooperation.

The most relevant results obtained in the reporting period are presented briefly:

2.3.1 CSP – Simulation of Transient Heat Loads

Involved Staff: Dr. Renate Fetzer

An experimental setup was developed and built to investigate material compatibility issues during transient heat loads in a CSP sodium receiver. The setup consists of the high-temperature sodium loop SOLTEC-2, successfully built and tested at the Institute for Neutron Physics and Reactor Technology (INR) at KIT, combined with an inductive heater to generate transient heat loads in a U-shaped test tube. In order to identify the influence of the frequency and of various coil parameters and to optimize the design of the inductive heater, a parametric numerical study using the software COMSOL Multiphysics was performed. Based on the results of the electromagnetic field simulations, the heater design could be optimized under the limitations of the available high-frequency circuit (150 kHz - 400 kHz, maximum active power 6 kW) and an expected heat load density of ~1 MW/m² could be achieved.

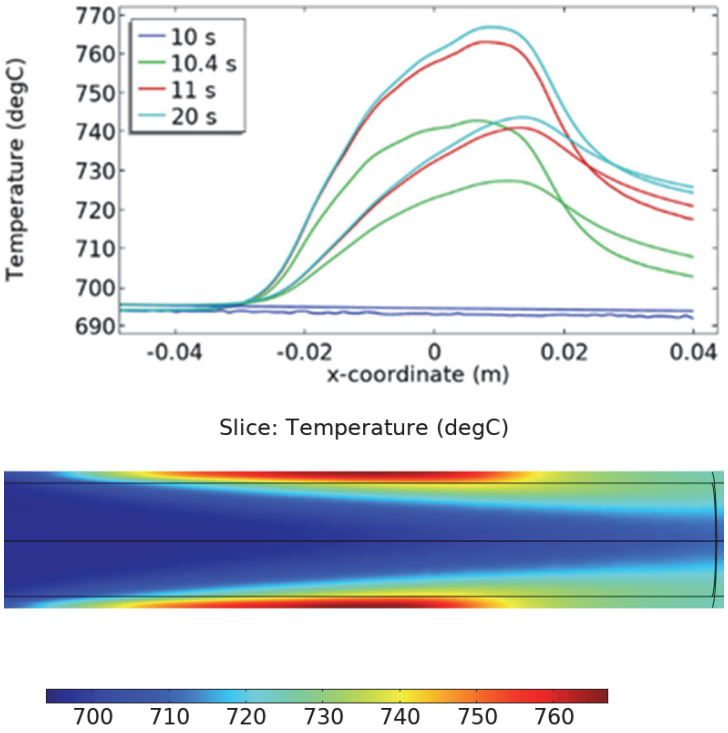

Fig. 2.3.1: Transient temperature distribution. Left column: Temperature profile along outer respectively inner side of lower wall of test tube at different time moments (inductive heating is switched on after 10 s). Right column: Stationary temperature distribution.

The optimized heater design was selected for further numerical studies, where the maximum achievable temperature as well as the expected heating and cooling rates were determined for various sodium flow velocities and inlet temperatures. The turbulent sodium flow was solved in CFD simulations using the Shear Stress Transport (SST) turbulence model with low Re number treatment of near-wall regions. The transient heat transfer Fig. 2.3.1 after switching on respectively off the inductive heating was modelled with the turbulent Prandtl number given by the relation of Kays-Crawford. Maximum heating and cooling rates in the order of 150 K/s were obtained. The optimized experimental setup is suitable for material tests under conditions relevant to the field of CSP.

2.3.2 Material Development

Involved Staff: Dr. A. Heinzel, Dr. C. Oskay, Dr. A. Weisenburger, Dr. H.Shi

First corrosion tests in liquid Na at 600 °C of 9Cr-steel and Ni-base alloy proved that corrosion at these conditions is only relevant if the impurity control (mainly oxygen) does not operate in the requested mode (the oxygen content needs to stay below 5 ppm). Tests at 700 °C or higher and thermal cycling tests are planned.

The corrosion behaviour of additive manufactured (AM, 3D-prinitng) 316 steel and IN718 in $MgCl_2$-KCl-NaCl molten salts at 700 °C were compared with that of commercial produced 316 steel and IN718 materials. The AM 316 steel exhibits an inferior corrosion behaviour mainly associated with segregated δ-ferrite at grain boundaries. The AM IN718 instead has a very similar corrosion resistance like the commercial produced counterpart.

Three Al-Cr-Fe-Ni-X (X: Cu, Ti or Nb) HEAs have been exposed to Pb-alloys to investigate the effect of the additional element X targeting for improved mechanical properties. The experimental results indicate that the fifth principle elements (Cu, Ti or Nb) not only modify the microstructure of Al-Cr-Fe-Ni model alloy, but also have significant influences on the hardness, corrosion behaviour and microstructure stability (after thermal aging).

Several ceramic materials that have shown their compatibility with liquid Sn at 1000 °C for 5000 h (the 10.000 h test at 950 °C is still ongoing) were exposed to 1150 °C hot Sn. The 1000 h test at 1150 °C confirmed the applicability of the tested materials. These plus pre-oxidized Kanthal APM (ferritic alumina former) are at time exposed for 5000 h at 1150 °C. Joining and assembling methods for scale up will be one of the further objectives in the work program.

The BMWi funded research project LIMELISA (LIquid MEtal and LIquid SAlt Heat Storage System) aims to explore the usability of materials for components (pumps and valves) in contact with molten Pb and molten solar salt at the temperature range between 600 °C-700 °C for their utilization as a heat transfer and storage medium in next generation energy generation methods. The task of IHM for this project is to investigate the corrosion mechanisms and their mitigation in molten Pb at 700 °C. For this purpose, a wide spectrum of materials (including almost all technical material groups) has been exposed in the COSTA facility in stagnant Pb at 600 °C and 700 °C under flowing Ar/H_2 cover gas ensuring a constant O_2-content of 2×10^{-7} wt.%. The table below Table 2.3.1 provides an overview on the tested materials and the test durations and temperature. Please note that the 5000 h tests are currently ongoing.

Material Group	Alloy	Exposure		
Martensitic Steels	**P91 (10CrMoVNb9-1)**	1000 h at 600°C and 700°C	2000 h at 600°C and 700°C	5000 h at 600°C and 700°C
	VV85 1.4748 (X85CrMoV18-2)	1000 h at 600°C and 700°C	2000 h at 600°C and 700°C	5000 h at 600°C and 700°C
Cast Steels	**1.4931 (GX23CrMoV12-1)** **1.4059 (GX22CrNi17-2)** **1.4408 (GX5CrNiMo19-11-2)**	1000 h at 600°C and 700°C	2000 h at 600°C and 700°C	**1.4408** **1.4552** **1.4136** 5000 h at 600°C and 700°C
	1.4136 (GX70CrMo29-2) **1.4552 (GX5CrNiNb19-11)**	1000 h at 600°C and 700°C	2000 h at 600°C and 700°C	
	1.4581 (GX5CrNiMoNb19-11-2) **9.4306 Noricid (GX3CrNiSiN20-13)**	1000 h at 600°C and 700°C	2000 h at 600°C and 700°C	No further exposure
Ferritic Steels	**Kanthal APM (Fe22Cr6Al)**	1000 h at 600°C and 700°C	2000 h at 600°C and 700°C	**Kanthal APM** 5000 h at 600°C and 700°C
	Kanthal APMT (Fe21Cr5Al3Mo)			
Austenitic Steels	**1.4571 (316Ti)**	1000 h at 600°C and 700°C	2000 h at 600°C and 700°C	**As-received and pre-oxidized (1000°C-4h)** 5000 h at 600°C and 700°C
	VV56 1.4875 (X55CrMnNiN20-8)	1000 h at 600°C and 700°C	2000 h at 600°C and 700°C	5000 h at 600°C and 700°C
	Alloy 800	No prior exposure		**As-received and pre-oxidized (1000°C-4h)** 5000 h at 600°C and 700°C
Ni-Based Alloys	**Alloy 625 (NiCr22Mo9Nb)**	1000 h at 600°C and 700°C	2000 h at 600°C and 700°C	No further exposure
	Alloy 617B (NiCr23Co12Mo)	1000 h at 600°C and 700°C	2000 h at 600°C and 700°C	
	Alloy 718 (NiCr19Fe19Nb5Mo3)	1000 h at 600°C and 700°C	2000 h at 600°C and 700°C	
	HR6W (23Cr-45Ni-7W)	1000 h at 600°C and 700°C	2000 h at 600°C and 700°C	
	Alloy 713C (NiCr12Al6Mo4Nb)	1000 h at 600°C and 700°C	2000 h at 600°C and 700°C	
	Alloy 602CA (NiCr25FeAlY)	1000 h at 600°C and 700°C	2000 h at 600°C and 700°C	
	Alloy 699XA (NiCr30Al)	1000 h at 600°C and 700°C	2000 h at 600°C and 700°C	
Additive Manufactured Ni-Based Alloys	**NADEA (Ni37Fe35Cr17Al8)**	1000 h at 600°C and 700°C	2000 h at 600°C and 700°C	
Ti-Alloys	**Ti-6Al-4V**	1000 h at 600°C and 700°C	2000 h at 600°C and 700°C	
	TNM-B1 (TiAl44Nb4Mo1)	1000 h at 600°C and 700°C	2000 h at 600°C and 700°C	
	GE48-2-2 (TiAl48Cr2Nb2)	1000 h at 600°C and 700°C	2000 h at 600°C and 700°C	
Co-Alloys	**Stellit 6** **Stellit 21**	1000 h at 600°C and 700°C	2000 h at 600°C and 700°C	**Stellit 6** 5000 h at 600°C and 700°C
Technical Ceramics	**Si_3N_4**	1000 h at 600°C and 700°C	2000 h at 600°C and 700°C	No further exposure
	WC (Co-bound) → KMS und GTD	1000 h at 600°C and 700°C	2000 h at 600°C and 700°C	5000 h at 600°C and 700°C
Pack Aluminized Alloys	**Al/P91** **Al/316Ti** **Al/718**	1000 h at 600°C and 700°C	2000 h at 600°C and 700°C	**Al/P91, Al/316Ti (As-received and pre-oxidized at 1000°C for 4h)** 5000 h at 600°C and 700°C **Al/718** 5000 h at 600°C and 700°C

Table 2.3.1: An overview on the tested materials in stagnant Pb at 600 °C and 700 °C.

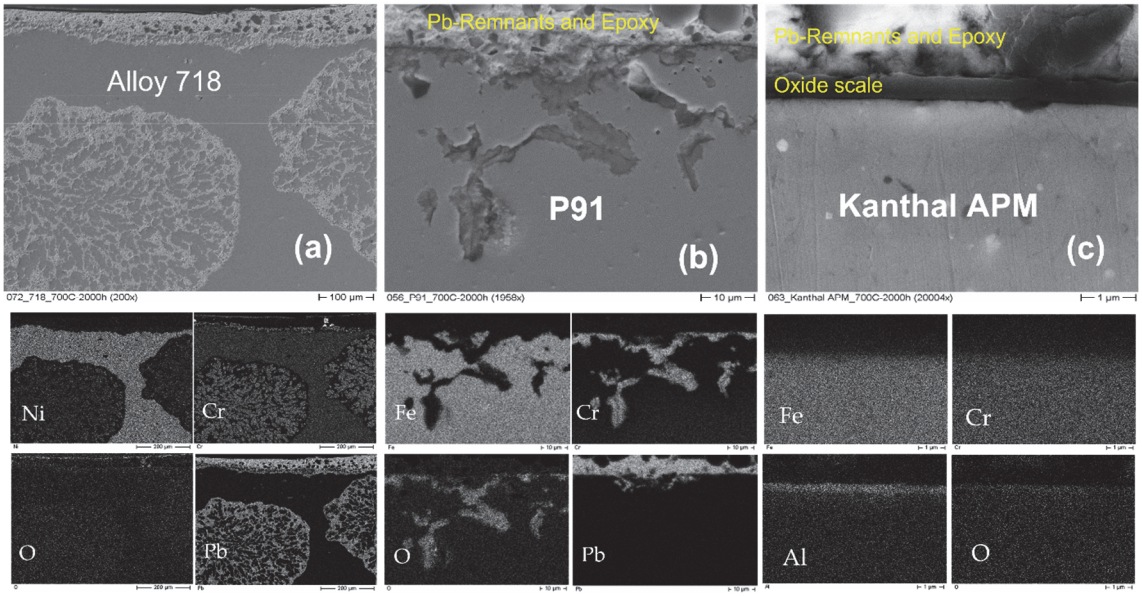

Fig. 2.3.2: Cross-sectional images and element distribution maps of (a) Alloy 718, (b) P91 and (c) Kanthal APM after 2000 h in stagnant Pb at 700 °C. Please note the different magnification in respective images.

The cross-sectional analyses (Fig. 2.3.2) have revealed the significantly higher corrosion resistance of alumina formers and of some ferritic steels compared to other tested alloys. While Ni-based alloys have suffered under a significant dissolution attack, alumina containing ferritic steels have formed a thin and highly protective alumina scale. This is exemplarily shown in the figure below, which depicts the cross-sectional images and element distribution maps of Alloy 718, P91 and Kanthal APM after 2000 h in stagnant Pb at 700 °C. Regarding Alloy 718 as the representative material for all the tested Ni-based alloys, it can be clearly seen that, the dissolution rate is higher than the growth kinetics of the oxide scale, thereby leading to a catastrophic dissolution attack which locally exceeds a thickness of 1 mm. Due to its higher solubility in Pb, Ni has been selectively dissolved from the alloy to the melt. On the other hand, the aluminium free 9 % Cr steel, P91, has formed a Cr-rich oxide scale; however also shown the internal oxidation of Cr. As the representative of the alloys, which has shown high corrosion resistance in Pb, Kanthal APM has formed a thin (submicron), highly adherent and Al-rich oxide scale thereby hindering the Pb infiltration to the alloy sub-surface and the consequential dissolution of the alloying elements to the melt.

2.3.3 Liquid metal battery

Involved Staff: M.Sc. T. Zhang, Dr. A. Heinzel, Dr. A. Weisenburger

A liquid metal battery consists of three different liquids, which stay separated due to density differences and mutual immiscibility. The negative electrode is made of a low-density liquid metal, in our case sodium, a medium-density molten salt serves as electrolyte, and a high-density liquid metal builds the positive electrode. For the latter Sb-Bi alloys are selected.

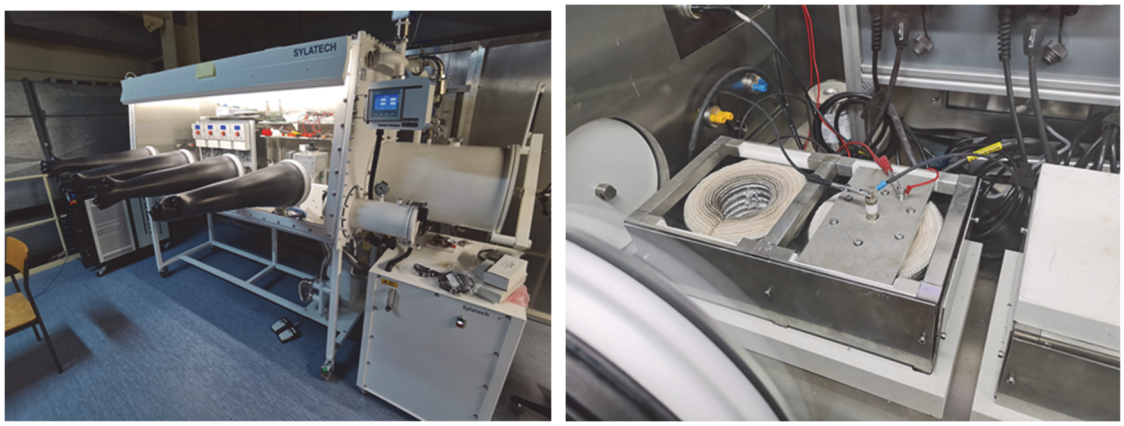

Fig. 2.3.3: Glove box with the test facility and a battery under testing.

For battery tests, a test facility (Fig. 2.3.3) was designed and built up. First tests were conducted on a battery cell design using a foam to hold the sodium. Parameters and assembling procedures such as temperature, electrolyte amount, and pre-treatment of the foam were adjusted. Furthermore, another cell design without foam was built up to achieve higher cell capacities and to make the battery more stable.

Besides, corrosion tests of various ceramics and steels in sodium and electrolyte vapor were performed. Test samples are under examination.

Involved Staff:

DP W. An, K. Baumann, Frau Dr. R. Fetzer, J. Fleig, **Dr. W. Frey**, Dr. Ch. Gusbeth, Frau Dr. A. Heinzel, D. Herzog, Dr. M. Hochberg, Dr. A. Jianu (Guest), D. Krust, DI (Fh) F. Lang, K. Leber, F. Lindner, L. Müller, **Prof. G. Müller**, Frau N. Nazarova, Dr. Ceyhun Oskay, Dr. I. Papachristou, **PD Dr. M. Sack**, Dr. H. Shi, Frau Dr. A. Silve, A. Sivkovich, DI R. Sträßner, **Dr. A. Weisenburger**, R. Wüstner, R. Yu (Guest), Y. Zhang, T. Zhang (DFG-PhD student), W. Zhen (CSC-PhD student)

Journal Publications

Sack, M.; Ruf, J.; Herzog, D.; Mueller, G. (2021). Auxiliary Power Supply for a Semiconductor-based Marx Generator. 2021 International Aegean Conference on Electrical Machines and Power Electronics (ACEMP) & 2021 International Conference on Optimization of Electrical and Electronic Equipment (OPTIM): 2-3 September 2021, Brasov, Romania, 220–224, Institute of Electrical and Electronics Engineers (IEEE). doi:10.1109/OPTIM-ACEMP50812.2021.9590076

Sack, M.; Hochberg, M.; Herzog, D.; Mueller, G. (2021). Fast sic-mosfet switch with gate boosting technology. PCIM Europe digital days 2021: International Exhibition and Conference for Power Electronics, Intelligent Motion, Renewable Energy and Energy Management Proceedings, 3 - 7 May 2021, 40–46, VDE Verlag.

Schlundt, J.; Soldatov, S.; Frey, W.; Link, G.; Baumann, K.; Jelonnek, J.; Sack, M.; Hochberg, M.; Silve, A. (2021). Conception and Development of a Pulsed Microwave Applicator for Exposure of Fresh Microalgae Biomass. IEEE Transactions on Plasma Science, 49 (9). doi:10.1109/TPS.2021.3101943

Shi, H.; Jianu, A.; Fetzer, R.; Szabó, D. V.; Schlabach, S.; Weisenburger, A.; Tang, C.; Heinzel, A.; Lang, F.; Müller, G. (2021). Compatibility and microstructure evolution of Al-Cr-Fe-Ni high entropy model alloys exposed to oxygen-containing molten lead. Corrosion Science, 189, Art.-Nr.: 109593. doi.org/10.1016/j.corsci.2021.109593

Arcena, M. R.; Leong, S. Y.; Then, S.; Hochberg, M.; Sack, M.; Mueller, G.; Sigler, J.; Kebede, B.; Silcock, P.; Oey, I. (2021). The effect of pulsed electric fields pre-treatment on the volatile and phenolic profiles of Merlot grape musts at different winemaking stages and the sensory characteristics of the finished wines. Innovative Food Science and Emerging Technologies, 70, Art.-Nr.: 102698. doi.org/10.1016/j.ifset.2021.102698

Zhang, T.; Heinzel, A.; Jianu, A.; Weisenburger, A.; Müller, G. (2021). Corrosion Investigations of Materials in Antimony–Tin and Antimony–Bismuth Alloys for Liquid Metal Batteries. TMS 2021 150th Annual Meeting & Exhibition Supplemental Proceedings. Ed.: The Minerals, Metals & Materials Society, 605–614, Springer. doi:10.1007/978-3-030-65261-6_55

Shi, H.; Fetzer, R.; Tang, C.; Szabó, D. V.; Schlabach, S.; Heinzel, A.; Weisenburger, A.; Jianu, A.; Müller, G. (2021). The influence of Y and Nb addition on the corrosion resistance of Fe-Cr-Al-Ni model alloys exposed to oxygen-containing molten Pb. Corrosion science, 179, Art.-Nr.: 109152. doi.org/10.1016/j.corsci.2020.109152

Papachristou, I.; Akaberi, S.; Silve, A.; Navarro-López, E.; Wüstner, R.; Leber, K.; Nazarova, N.; Müller, G.; Frey, W. (2021). Analysis of the lipid extraction performance in a cascade process for Scenedesmus almeriensis biorefinery. Biotechnology for biofuels, 14 (1), Article: 20. doi:10.1186/s13068-020-01870-1

3 Safety Research for Nuclear Reactors (NUSAFE): Transmutation - Liquid Metal Technology -

Contact: Prof. Georg Müller

Long-living high-level radioactive waste from existing nuclear power reactors should be transmuted in short-living radio nuclides using fast neutrons provided by a spallation target in an accelerator driven subcritical system or by a fast nuclear reactor. The objective is to reduce the final disposal time of high-level radioactive waste (plutonium, minor actinides) from some 10^6 years down to about 1000 years. Lead (Pb) and lead-bismuth (PbBi) are foreseen as spallation-target and coolant of such devices.

The aim of the institute's contribution is to develop advanced corrosion mitigation processes based on in-situ formation of protective alumina scales especially for parts under high loads like fuel claddings or pump materials in contact with liquid Pb or PbBi. Pulsed large area electron beams (GESA) are used to create aluminum containing surface alloys on steels. In addition, bulk alumina formers like FeCrAl, AFA (alumina forming austenitic steels) and HEA (high entropy alloys) are developed.

All tasks are embedded in European funded international projects and cooperations e.g., ILTROVATORE, GEMMA, ORIENT-NM and EERA-JPNM.

The most relevant results obtained in the reporting period are presented briefly:

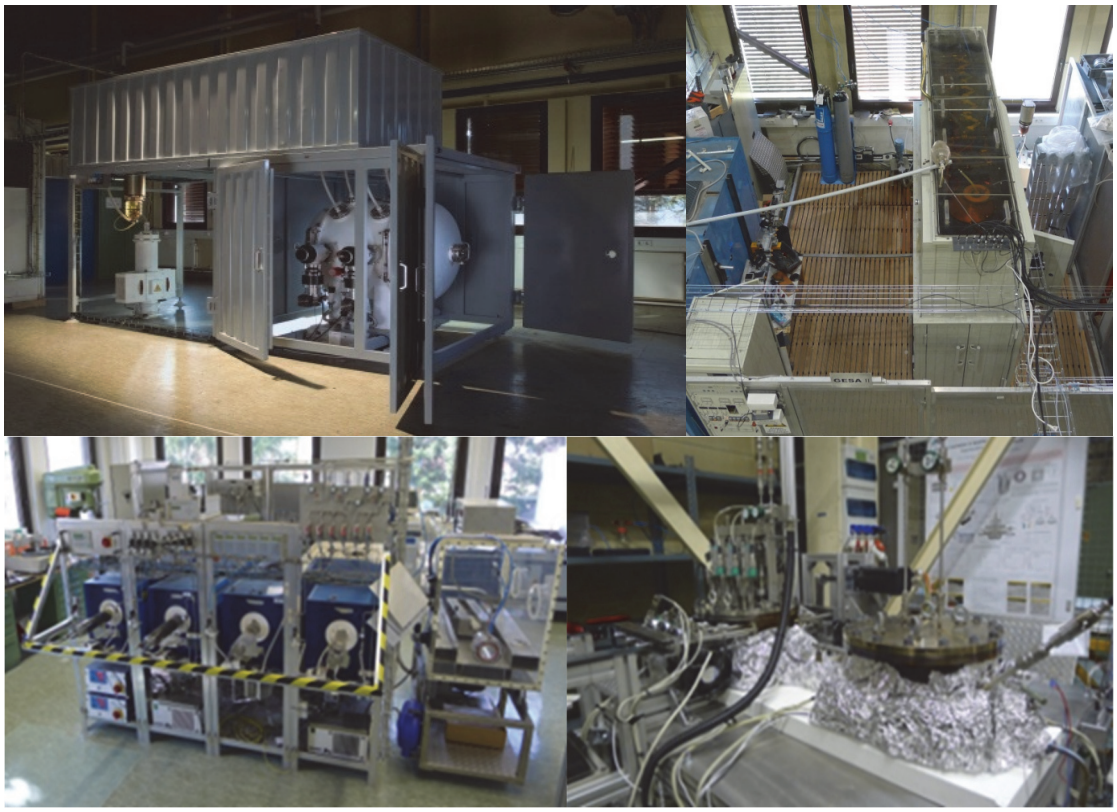

3.1 Material development and advanced corrosion mitigation strategies for heavy liquid metal-cooled nuclear systems

Contact: Dr. Alfons Weisenburger

3.1.1 GESA

Involved Staff: DP Wladimir An

Heat loads with power densities of several MW/cm² are an important area in many application-oriented processes of material treatment. The peculiarity of such power densities is that the intensity of the energy input must on the one hand be sufficiently high to achieve a defined treatment volume (energy densities up to some tens of kJ/g), but on the other hand should still be below the level at which intensive plasma generation takes place at the surface. Most of the processes that are important for the stability of the melt-metal vapor interface are almost identical regardless of the type of energy carrier (laser beam during welding or thermal treatment of surfaces; plasma jet in fusion reactors; high current ion and electron beams); namely: ablation pressure of the expanding gas or plasma of several bar; intense steam flow along the surface of the melt. This means that the conditions for the development of known instabilities such as Rayleigh-Taylor, Kelvin-Helmholtz, Capillary-wave are fulfilled or not regardless of the type of energy input.

Electron beams as energy carrier differ from the others in one respect. The penetration depths of the high-energy electrons are comparable to the thermal diffusion lengths of the target material. This property of electron beams leads to a special mechanism of droplet formation through the formation (Fig. 3.1.1) and explosive expansion (Fig. 3.1.2) of vapor bubbles on the surface of the melt. The character of the 1D space-time trajectories of the droplets and the velocity distribution with respect to the weight or volume of the droplet show typical features of a bubble explosion. One possible mechanism of bubble formation may be the inversion of the temperature of the near-surface melt layer. This brings deeper layers of the melt to the evaporation temperature more quickly. One reason for the temperature inversion is the back reflection of a part of the beam electrons, as this is limited to an area close to the surface, which is also significantly smaller than the penetration depth of the primary electrons.

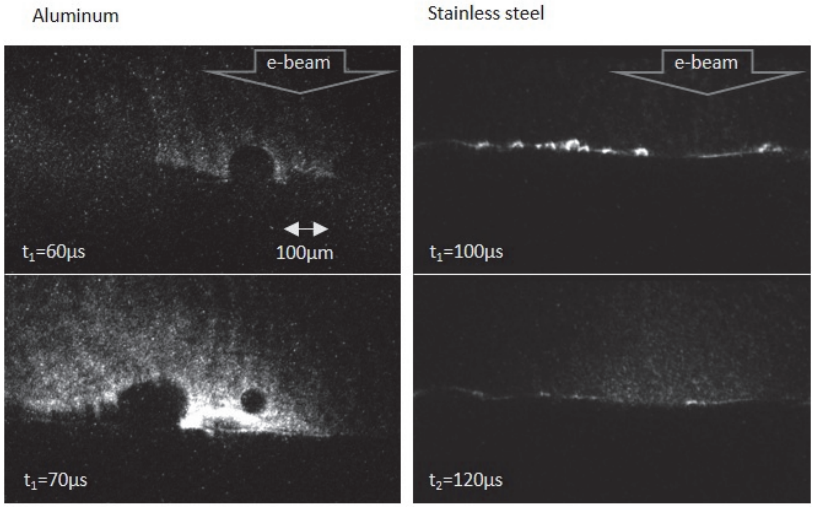

Fig. 3.1.1: 2D Schlieren imaging of droblets formation at the melt layers of aluminum and stainless steel.

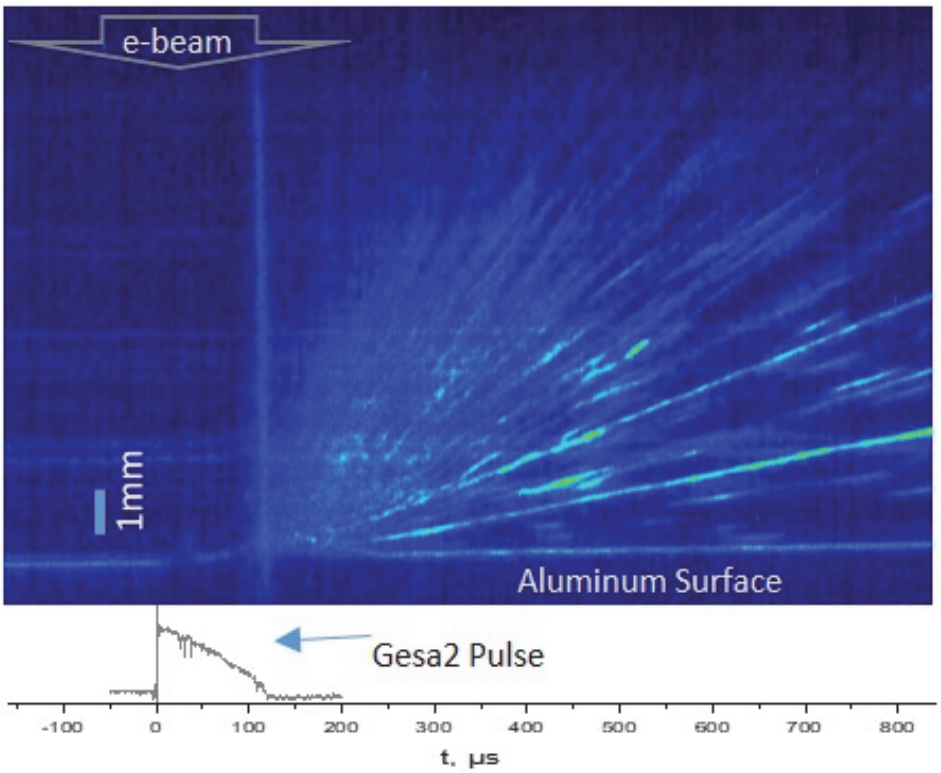

Fig. 3.1.2: 1D Schlieren imaging of droblets splashing from melt layer of aluminum, recorded with Streak-Camera.

3.1.2 Erosion corrosion experiments in the CORELLA facility

Involved Staff: Dr. R. Fetzer, Dr. A. Heinzel, DI F. Lang, Dr. A. Weisenburger

Within the GEMMA project, erosion corrosion experiments were performed in the CORELLA facility in liquid lead bismuth eutectic (LBE) with an oxygen content between 10^{-9} and 10^{-8} wt% at 489 °C and a test duration of 500 h. According to numerical simulations the average speed along the lateral surface was between 0.3 m/s (200 rpm) and 1.6 m/s (1200 rpm). Because of the low oxygen concentration, the tested austenitic steels 316L and 15-15Ti showed dissolution at the surfaces and the formation of an Fe rich surface layer, which tents to spall off and erode already at flow velocities above 0.8 m/s. The erosion of material generally increases for increasing velocity, with the highest erosion rates near the corners of the edges. No signs of corrosion or erosion were observed on Al_2O_3 coated surfaces produced by pulsed laser deposition (PLD) and detonation gun (DG) on the lateral flat surfaces.

In the case of alumina-forming austenitic (AFA) steels, the steel should be protected by forming protective Al_2O_3 in situ. The low oxygen concentration in the exposure experiments made this more difficult. Nevertheless, tempering colours hint on a very thin oxide layer at the AFA steels with 3 wt% Al, 15.7-15.9 wt% Cr, and 22.6-22.8 wt% Ni. However, defects such as impurities or precipitates led to local dissolution attack with heavy metal inclusion. The AFA steel with a higher amount of Ni (25.5 wt%) and Al (4.5 wt%) shows a corrosion attack at the entire surface. However, an erosion attack was not observed on any of the flat surfaces. The edges were more sensitive to erosion and here the higher amount of Ni and Al seems to improve the mechanical resistance against erosion as long as the material is intact.

3.1.3 Material development to mitigate corrosion

Involved Staff: Dr. R. Fetzer, Dr. A. Heinzel, Dr. A. Weisenburger

In the frame of the EU project GEMMA, three different alumina / alumina forming coatings were tested in liquid Pb with 10^{-7} wt% oxygen at 480 °C and 550 °C for up to 10000 h. For the alumina coating two different methods were chosen: pulsed laser deposition (PLD) and detonation gun (DG). At 480 °C the PLD sample showed no corrosion but a slight reaction with Pb at the surface. At the higher temperature this coating failed. The DG sample showed a much better behaviour, but the coating seems to be in a thermodynamic metastable condition, which leads to a phase transition form γ-Al_2O_3 to α-Al_2O_3 and a preferred rearrangement to a denser α-Al_2O_3 during exposure at 550 °C. However, it seems that this transition has no negative influence on the corrosion behaviour up to 10000 h.

Additionally, an alumina forming coating produced by pack cementation was tested at 48 °C. After 10000 h no dissolution attack is visible. The outer part of the surface layer has a higher amount of Al and Ni, the surface is oxidized and protects the steel.

In the frame of the GEMMA project, four different AFA steels manufactured by SANDIVK based on IHM design were exposed to Pb at 550 and 600 °C. Two of these steels were in addition send to ENEA for exposure and to NCBJ for Nanoindentation before and after ion irradiation. The processed 3rd generation AFA steels with the general chemical composition: Fe-16Cr-(23; 25.5)Ni-(3; 4.5)Al-C(N)-(Y), showed corrosion resistance at 600 °C, while at 650 °C the alloy with N instead of C showed some dissolution attack. The passivating scale was based on $(AlCr)_2O_3$ at both temperatures. Irradiation with 12 MeV Fe ions revealed no increase in hardness and resulted in a reduced number of dislocation loops.

Involved Staff

DP W. An, Dr. R. Fetzer, Dr. A. Heinzel (Guest), Dr. A. Jianu, DI (Fh) F. Lang, F. Lindner, L. Müller, **Prof. G. Müller**, Dr. H. Shi, A. Sivkovich, **Dr. A. Weisenburger**, W. Zhen (SCS-PhD student)

Journal Publications

Shi, H.; Wang, H.; Fetzer, R.; Heinzel, A.; Weisenburger, A.; Wang, K.; Jianu, A.; Müller, G. (2021). Influence of Si addition on the corrosion behaviour of 9 wt% Cr ferritic/martensitic steels exposed to oxygen-controlled molten Pb-Bi eutectic at 550 and 600 °C. Corrosion Science, 193, Art.-Nr.: 109871. https://doi.org/10.1016/j.corsci.2021.109871

Balbaud, F.; Cabet, C.; Cornet, S.; Dai, Y.; Gan, J.; Hernández Mayoral, M.; Hernández, R.; Jianu, A.; Malerba, L.; Maloy, S. A.; Marrow, J.; Ohtsuka, S.; Okubo, N.; Pouchon, M. A.; Puype, A.; Stergar, E.; Serrano, M.; Terentyev, D.; Wang, Y. G.; Weisenburger, A. (2021). A NEA review on innovative structural materials solutions, including advanced manufacturing processes for nuclear applications based on technology readiness assessment. Nuclear materials and energy, 27, Article no: 101006. doi.org/10.1016/j.nme.2021.101006

Shi, H.; Fetzer, R.; Jianu, A.; Weisenburger, A.; Heinzel, A.; Lang, F.; Müller, G. (2021). Influence of alloying elements (Cu, Ti, Nb) on the microstructure and corrosion behaviour of AlCrFeNi-based high entropy alloys exposed to oxygen-containing molten Pb. Corrosion science, 190, Article no: 109659. doi.org/10.1016/j.corsci.2021.109659

Fetzer, R.; Weisenburger, A.; Müller, G. (2021). Turbulent flow of liquid lead alloy in oxygen-controlled corrosion erosion test facility. AIP Advances, 11 (7), Article no: 075303. doi:10.1063/5.0057380.

4 Materials and Technologies for the Energy Transition (MTET): Power-based Fuels and Chemicals - Microwave Process Technology -

Contact: Dr. Guido Link

Besides the activities on development of technologies and systems for the plasma heating in the FUSION Program, IHM is also in charge of research and development in the Power-based Fuels and Chemicals part of the MTET Program.

The main focus of IHM in this field of research is in plasma chemistry such as CO_2 dissociation or H_2 production by use of atmospheric plasmas sustained by high power microwaves, generated by innovative solid-state amplifiers. For this purpose, the power of plasma sources has been increased and further efforts were undertaken regarding plasma diagnostic and multiphysics modelling

The expertise on microwave engineering and the existing industrial scale high power microwave infrastructure faces growing interest from industry and research. As a consequence, the research group is involved in several national and international joint research projects with objectives in various fields of applications. In the frame of the H2020 Marie Curie international training network TOMOCON a microwave tomographic sensor has been developed and tested in a close to industrial environment for improved control in a microwave drying process. Based on the German-Korean project REINFORCE the potential of microwave dielectric heating has been investigated with respect to energy efficient carbon fiber production. Further activities investigated the microwave assisted intermittent pultrusion of CFRP profiles (IMPULS), microwave assisted additive manufacturing with continuous carbon fiber reinforce thermoplastic filaments and well as lamination of synthetic textiles for automotive industries by energy efficient selective microwave heating (e-KOMFORT).

In 2021 the highly multidisciplinary Helmholtz IVF project CORAERO (Airborn Transmission of SARS Coronavirus) started, which brings together scientists from virus biology, medicine, applied physics, chemistry, and engineering to understand virus spreading through aerosols and designing technical and administrative measures for mitigation and virus control. IHM is involved in design and investigation of microwave-based concepts for inactivation of coronavirus.

4.1 Plasma Chemistry

Contact: Dr. Sergey Soldatov

Energy efficient conversion of CO_2 molecules into fuels is an attractive option for renewable energy storage as well as for mitigation of greenhouse gases emissions (e.g. closing the carbon cycle). Among different plasma discharges microwave sustained plasmas have shown to be most efficient for CO_2 splitting into CO and Oxygen. The efficiency of the process can potentially be promoted by pulsed supply of microwave energy into the plasma discharge in short pulses with a modulation time shorter than characteristic vibrational-to-translational energy transfer times. In atmospheric pressure plasmas, the demand on the speed of energy pulsations is much higher than at vacuum conditions because of the higher collisional frequencies.

The main efforts in 2021 were undertaken towards the understanding of plasma fluid dynamics and further development of plasma diagnostics. The CFD computation of gas flow in a surfaguide plasma reactor at temperatures relevant to ones measured in experiment have advanced the understanding of flow and temperature patterns for a tangential gas supply.

Additionally, the first operation of FT-IR spectrometer in pulsed registration mode for the pulsed microwave plasma experiment enables the estimation of the evolution of IR spectra on the ns-time scale.

The fast imaging was utilized to follow the emission light pattern in pulsed CO_2 and air plasmas in a coaxial plasma torch with a time resolution of about one hundred nanoseconds.

At the end of 2021 the development of a microwave interferometer system was started, which is aimed for measurement of plasma electron density in the surfaguide plasma reactor at the beginning 2022.

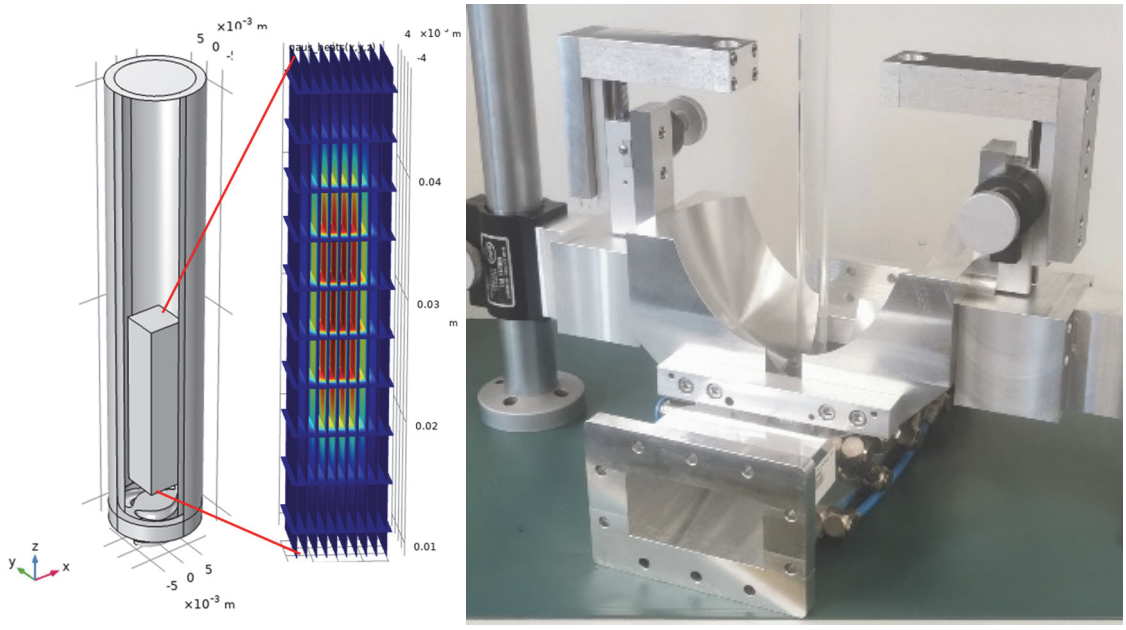

Fig. 4.1.1: CFD model of the surfaguide including heat source and helical gas flow (left) self-developed interferometer system mounted on the surfaguide plasma reactor (right).

4.2 Energy-Efficient Laminating Technology with Optimized, Innovative Microwave Technology for 3-Dimensional Form Parts (e-KOMFORT)

Contact: M.Sc. Dominik Neumaier

Comfort is increasingly becoming an important decision criterion for buying a car. High-quality materials and comfort are the interface to the user and help to implement the new vehicle concepts more quickly. Up to 9 m^2 of technical textiles are nowadays installed in cars, making them more attractive both visually and haptically. The laminating process of decorative materials is a very energy and time intensive process. By using a new microwave technology, the energy requirement can be reduced by more than 70 % and the process can be accelerated. The main objective of this project is to develop an innovative process and tool technology for the energy-efficient lamination of decorative materials by using microwaves.

An important task at the beginning of the project was to develop a new type of adhesive which, compared with the decorative materials, can be heated much better in the microwave oven. For this purpose, a measuring system was developed that can measure the dielectric properties of the adhesive. In cooperation with a project partner a new type of adhesive was designed that met the requirements for selective microwave heating in the oven. Furthermore, a microwave resonator with four loop antennas was designed and built up. To ensure a good homogeneous heating, the patented Hephaistos technology was used and four 1 kW solid-state microwave generators, which operate in the frequency range from 2.4 GHz to 2.5 GHz, were installed (see Fig. 4.2.1 (left)). In order to fully exploit the degrees of freedom of the microwave sources, a control system was developed which can adjust phase, frequency and power of the individual sources in the millisecond range. In initial studies, flat components were laminated to optimize and validate the process. In a second step a real component such as the cover of a glove locker (Fig. 4.2.1 (right)) was laminated using microwave heating. Therefore, a microwave-compatible tool was developed to press the decorative material onto the workpiece.

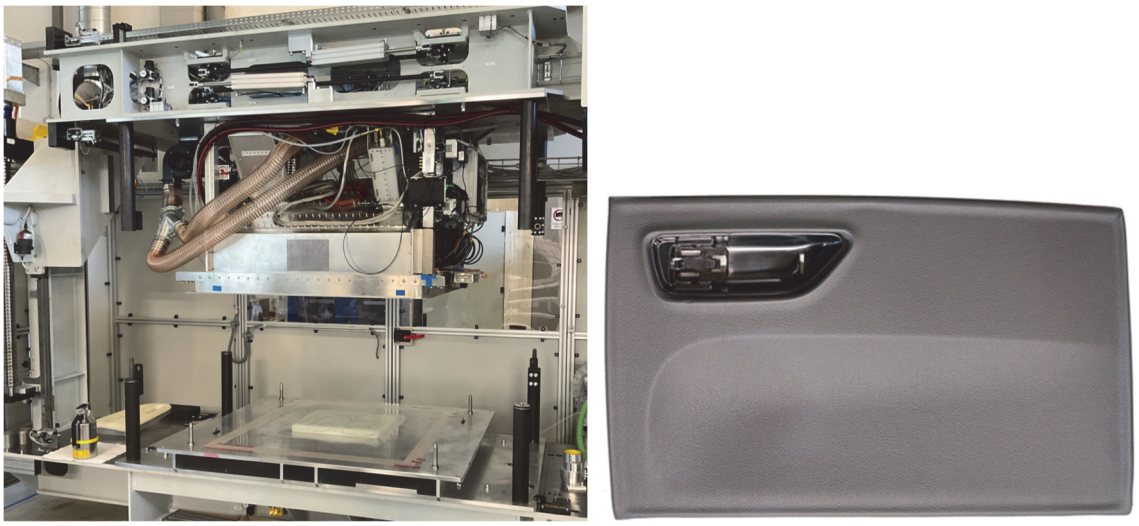

Fig. 4.2.1: e-KOMFORT microwave system (left); cover of a glove locker laminated with synthetic leather (right).

Funding: 6th Energy Research Programme of the Federal Government, support code 03ET1576A

4.3 Energy-Efficient Production of Robust Carbon Fibers (REINFORCE)

Contact: M.Sc. Julia Hofele

Carbon fibers are widely used in lightweight applications, but the carbon fiber production is rather expensive and energy intensive compared to the production of aluminium and steel. Microwave heating has the benefit of heating in the volume, which leads to cold ovens and may lead to faster heating rates. For this reason, the goal of the project is to research the production of carbon fibers with dielectric heating. Multiple exothermic reactions take place in the stabilization stage of the production, which can lead, especially in combination with microwave heating, to a thermal runaway effect. In order to completely model the heating process mathematically, the link between the degree of conversion due to the chemical reactions and the dielectric properties is needed. For this reason, temperature dependent measurements with a holding time of 300 minutes were conducted with conventional heating through a hot air flow. A mathematical model for the connection between the degree of conversion α and the dielectric loss ε_r'' was setup and fitted to the measurements. The result, see Fig. 4.3.1, shows a good agreement. However, the strong influence of the air flow temperature becomes visible, when comparing measurement runs of different days, see Fig. 4.3.2 a), with the same process parameters. Through the model, it could be determined, that the actual temperature was higher by 7.7 °C. The next step is to find process parameter combinations with the help of the process model that will lead to the desired temperature and validate it experimentally.

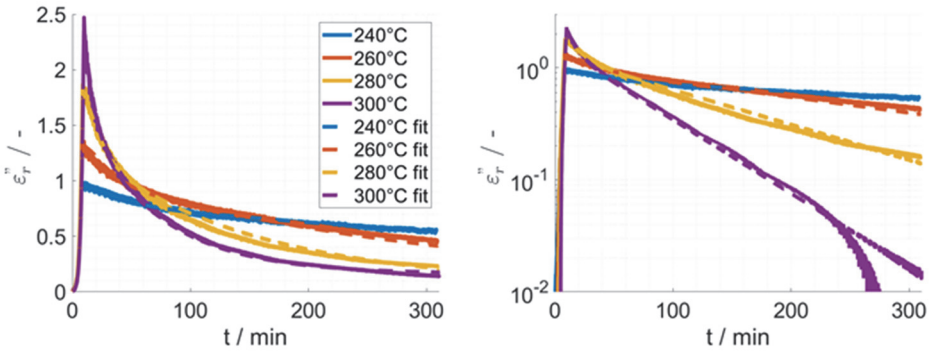

Fig. 4.3.1: Linear (left) and logarithmic (right) graphical presentation of the measured dielectric loss and the fitted curves.

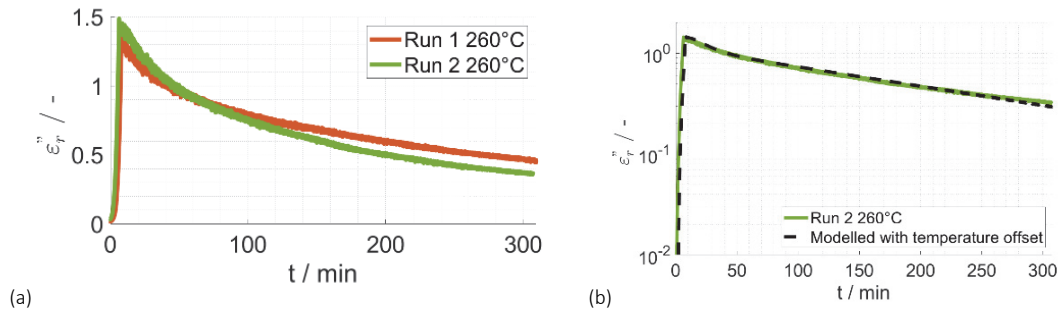

Fig. 4.3.2: First result of microwave heated PAN fiber. (a) Dielectric loss of the same process parameters measured at different runs. (b) Logarithmical comparison between measured dielectric loss and fitted values using a temperature offset.

Funding: ZIM cooperation project; support code ZF4204603SY7

4.4 Smart Tomographic Sensors for Advanced Industrial Process Control (TOMOCON)

Contact: M.Sc. Adel Omrani Hamzekalaei

The European Marie Skłodowska-Curie Training Network TOMOCON joins 12 international academic institutions and 15 industry partners, who work together in the emerging field of industrial process control using smart tomographic sensors. In close collaboration with Chalmers University of Technology and the University of Eastern Finland KIT is engaged in the development of a microwave tomography (MWT) and its application in microwave drying of porous materials.

This microwave tomography (MWT) system was integrated in a high-power microwave drying system to determine the moisture distribution inside wet polymer foam. The microwave drying system is equipped with a conveyor belt that enables a continuous drying process. The objective is to dry the foam uniformly. Intelligent control of distributed microwave sources is a possibility that might efficiently address any non-uniform moisture distribution. This requires the in-situ and non-invasive measurements of the unknown moisture distribution inside the foam. The MWT setup consists of a total of 11 open-ended waveguide (WR90) antennas connected to an Agilent N5224A VNA with a P9164C 2×16 USB solid-state switch matrix has been designed and installed next to the HEPHAISTOS oven (see Fig. 4.4.1 left). Various models and algorithms to solve the inverse problem have been developed and investigated. The 1D moisture distribution using convolutional neural network (CNN) is shown in Fig. 4.4.1 (right).

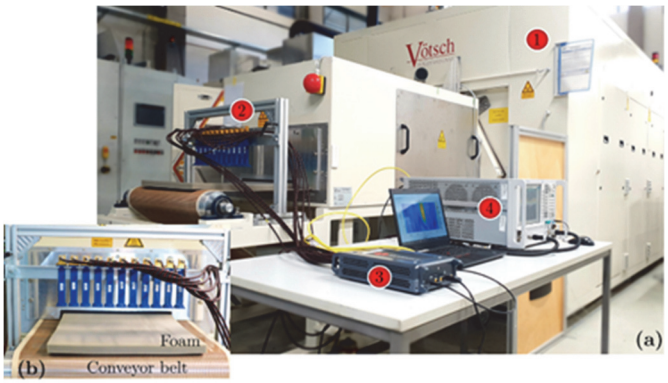

Fig. 4.4.1: (a) MWT system and its integration with the HEPHAISTOS (number Tag 1) is shown. The number Tags 2, 3, and 4 shows the MWT system, Solid state switch, and VNA respectively. (b) shows the enlarged view of the MWT sensor array of X-band open-ended waveguide antennas.

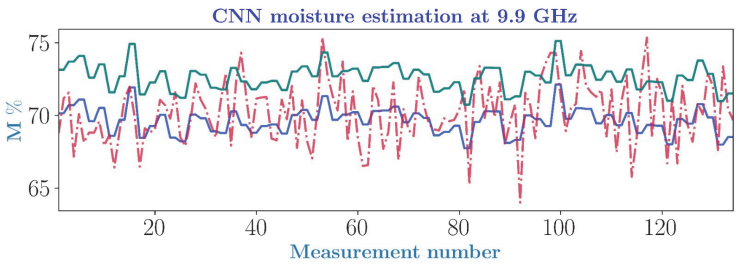

Fig. 4.4.2: Reconstructed image using CNN method, where blue lines are true moisture, green lines are true moisture uncertainty due to the weight, and red dash lines are reconstructed moisture value.

Funding: H2020-MSCA-ITN-2017; Grant agreement 764902 www.tomocon.eu

4.5 Innovative Microwave Pultrusion for the Cycle Controlled Sequential Curing of Fiber Reinforced Plastics for Modular Automated Manufacture of Complex Components (IMPULS)

Contact: M.Sc. Moritz Engler

Pultrusion is a manufacturing process for the continuous production of fiber-reinforced polymer profiles, where reinforcing fibers are impregnated with a thermoset resin and then pulled though a heated die, which forces the material into the desired cross section and simultaneously cures the resin. Due to the continuous nature of the process it is significantly more economical than other manufacturing methods for fiber-reinforced composites. However the nature of the process limits it to constant cross section profiles which are straight or of constant radius.

The IMPULS Project aims to develop a microwave powered pultrusion process for the production of carbon fiber-reinforced composite profiles. As the microwave powered pultrusion tool allows to selectively heat the profile in the otherwise cold tool, the degree of cure of the profile can be changed instantaneously by changing the microwave power. By alternating between fully cured and uncured segments, the profile can be locally deformed, opening the process to a variety of new applications. The focus of the IMPULS project lies in developing an applicator with a heating zone that is as focused as possible to allow short transition regions between fully cured and uncured segments. The concept of intermittent pultrusion was demonstrated successfully and transition regions below 1 cm length could be acchieved.

After the general concept was proven the applicator design was further optimized to improve the temperature surveilance and reduce the risk of the matrix material sticking to the ceramic dies. The control system of the microwave source was adapted to allow integration in the programmable logic controller of the pultrusion line. This improved experimental setup is now used for paramter studies regarding the process parameters and to evaluate the performance of different resin systems and tool surface coatings.

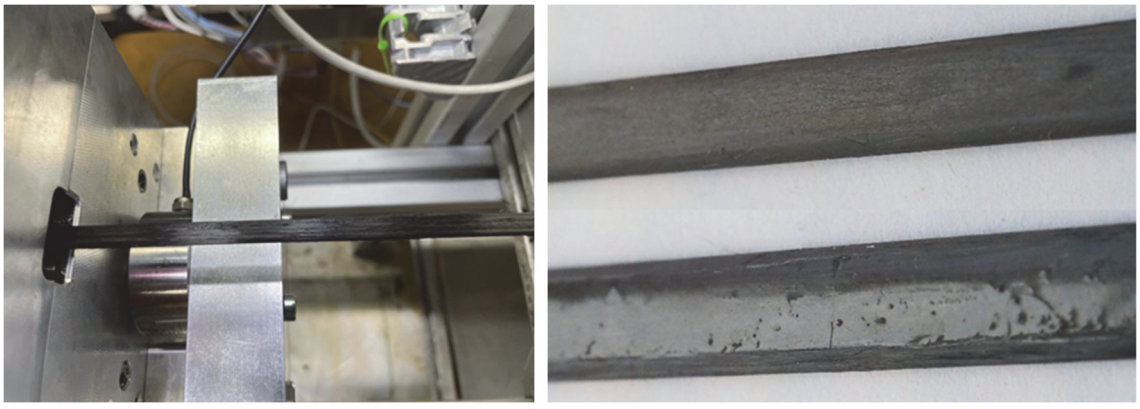

Fig. 4.5.1: Left: Fully cured profile exiting the microwave applicator; Right: Comparison of a profile of good quality with homogeneous cure (top) and a profile pultruded at insufficient microwave power (bottom) resulting in cured edges but wet resin on the flat surface of the profile.

Funding: ZIM cooperation project, support code: ZF4204604BL8

4.6 3D Microwave Printing of Composites

Contact: Dr. Nanya Li

Many industrial sectors, such as the automotive and aviation industries, rely on fiber reinforced composites as a high-tech material. Using additive manufacturing (known as 3D printing) techniques and their freedom of design, a plastic matrix with continuous fiber reinforcement are used to create lightweight components with high strength. However, the known 3D printing processes in terms of continuous reinforcements are very limited regarding filament diameter, printing speed and structure complexity due to the bottlenecks of the heating source and printing control technologies. Here, a pre-impregnated filament - a string-shaped polymer that encloses the continuous fibers - is fed into a coaxial microwave resonator where it is heated instantaneously and volumetrically. This allows uniform and rapid heating of even large diameter filaments made of continuous carbon fiber reinforced Polylactic Acid (PLA), Polyamide (PA) and Polyetheretherketone (PEEK). A model-based microwave power control system was developed to reach a predefined filament temperature during the printing process. The relationship between printing speed and microwave power is established for printing process control. Based on these efforts, the printing temperature has been tuned in real-time to fabricate self-supported lattice structures. The large-scale and support-free lattice structures reinforced by continuous fibers have been printed and shown in Fig. 4.6.1.

The digital twins based multi-robot cooperation strategy for 3D microwave printing has been researched. The developed path planning system can generate optimized and continuous printing paths that follow the load transmission flow and avoid collisions, which is transferred to the control system of the robots. By employing the digital twins, the cooperation strategy according to the complexity of the lattice structures can be defined beforehand. Furthermore, a high-fidelity digital model of the printing platform can be established to run with the printing process at the same time, which provides the advantages to optimize printing path, predict potential risks and cut down the manufacturing cycle. This technology solves the key problems and is the next-generation manufacturing approach for high-performance, lightweight and complex industrial applications.

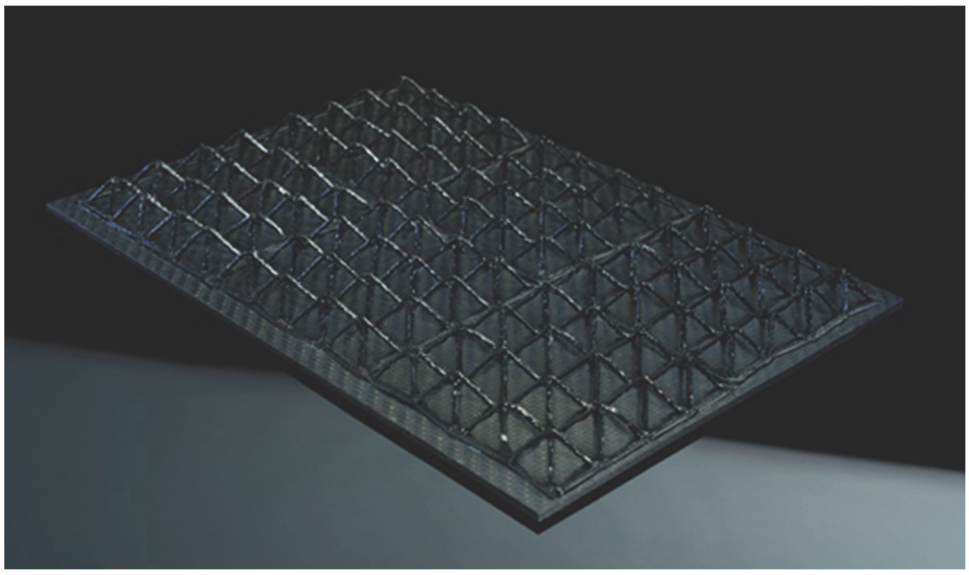

Fig. 4.6.1: 3D microwave printed lattice sandwich structure reinforced by continuous carbon fibers.

Funding: Alexander von Humboldt Research Project, YIG Prep Pro

4.7 Airborne Transmission of SARS Coronavirus (CORAERO)

Contact: Dr. Jesus Nain Camacho Hernandez

The COVID-19 pandemic, is an ongoing global pandemic caused by the respiratory syndrome coronavirus (SARS-CoV-2). Accordance to the World Health Organization (WHO) by December 2021 there have been around 300 million confirmed cases of COVID-19, including 5 million deaths. There is a clear need to develop novel and efficient technologies to prevent transmission and thus keep this and future pandemics under control. The Helmholtz IVF project CORAERO brings together a multidisciplinary group of scientists from virus biology, medicine, applied physics, chemistry, and engineering to understand virus spreading through aerosols and designing technical and administrative measures for mitigation and virus control.

The IHM group "Materials-Processing with Microwaves" participates in the CORAERO project, by researching on air purification systems that use microwave radiation to reduce virus load in closed spaces, such as public and private rooms. Extracorporeal inactivation of the virus addresses treatment of airborne virus from droplets and aerosols. Among the physical inactivation strategies, structural damage of the virus by heat and electric fields (E-field) of moderate strength are currently the methods of choice as they can be achieved within the microwave frequency spectrum.

For this purpose, two microwave applicator concepts are being considered. The first applicator is based on a resonant cavity that achieves an electric field of moderate strength (E-field > 10^5 V/m) in its interior with the purpose of destabilizing proteins (i.e. spike protein) of the virus, inducing long-lasting structural damage. To achieve the desired E-field strength and to allow an airflow through the cavity, the cavity incorporates an inner-holed low loss dielectric disk as shown in Fig. 4.7.1 (left). According to numerical calculations obtained by electromagnetic simulations, the cavity offers a fairly uniform electric field in the direction of the airflow (see Fig. 4.7.1 right). A second applicator based on using selective and energy-efficient filter media heated by microwaves, is currently being design. The applicator is intended for addressing filter sterilization of pathogenic aerosols, which is necessary to prevent virus re-entrainment into the exhaust air and protect people during maintenance. Surface and depth filtration are the aerosol and droplet capture methods which will be implemented in this microwave applicator, by using membranes and filters. The applicator aims to improve filter technologies such that inherent virus inactivation is possible and air purification is less energy intensive, especially when operated in large spaces.

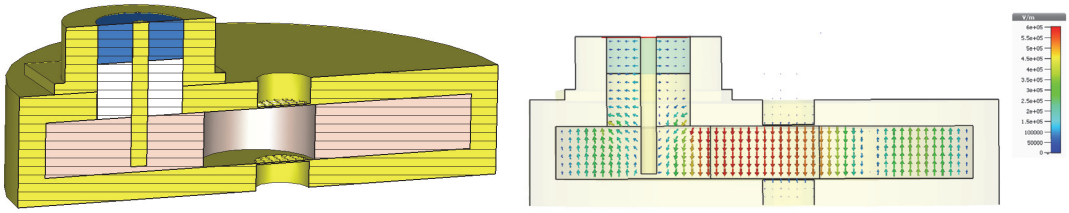

Fig. 4.7.1: (left) Cross-sectional view of the microwave applicator intended for virus inactivation using E-fields, and (right) its E-field profile.

Funding: HGF Initiative and Networking Fund Project CORAERO www.coraero.de

Involved Staff

M. Blekhshtein, J. N. Camacho Hernandez, M. Engler, Frau J. Hofele, Prof. J. Jelonnek, Dr. N. Li, **Dr. G. Link**, D. Neumaier, V. Nuss, A. Omrani Hamzekalaei, V. Ramopoulos, T. Seitz, S. Soldatov

Journal Publications

Zhang, Y.; Yadav, R.; Omrani, A.; Fjeld, M. (2021). A novel augmented reality system to support volumetric visualization in industrial process tomography. IHCI GET 2021 Proceedings. Proceedings of the IADIS International Conference Interfaces and Human Computer Interaction Proceedings of the IADIS International Conference Game and Entertainment Technologies. Hrsg.: K. Blashki, 3–9, IADIS Press.

Hofele, J.; Gandert, J.; Link, G.; Jelonnek, J. (2021). Modelling the thermal runaway during the stabilization phase of the carbon fiber production using microwave heating. AMPERE 2021: 18th International Conference on Microwave and High-Frequency Applications: 13th -16th September 2021, Gothenburg, Sweden, 234, Chalmers University of Technology (Chalmers).

Neumaier, D.; Link, G.; Jelonnek, J. (2021). Influence of cavity size and material properties on the uniformity of dielectric heating using distributed sources and novel solid-state microwave amplifiers. AMPERE 2021: 18th International Conference on Microwave and High-Frequency Applications: 13th -16th September 2021, Gothenburg, Sweden, 155, Chalmers University of Technology (Chalmers).

Togashi, M. M.; Perdomo, C. P. F.; Link, G.; Kiminami, R. H. G. A. (2021). Effect of initial particle size of the hematite on microwave sintering kinetics at 30 GHz. AMPERE 2021 Proceedings, 8th International Conference on Microwave and High - Frequency Applications, 13th - 16th September 2021, Chalmers University of Technology (Chalmers).

Yadav, R.; Omrani, A.; Vauhkonen, M.; Link, G.; Lähivaara, T. (2021). Complex-permittivity estimation of a polymer foam using microwave tomography for the application of microwave drying. AMPERE 2021 Proceedings, 8th International Conference on Microwave and High - Frequency Applications, 13th - 16th September 2021, 42, Chalmers University of Technology (Chalmers).

Li, N.; Link, G.; Jelonnek, J. (2021). A compact quarter wavelenght filter for 3D microwave printing of continuous fiber reinforced polymers. AMPERE 2021: 18th International Conference on Microwave and High-Frequency Applications: 13th -16th September 2021, Gothenburg, Sweden, 1, Chalmers University of Technology (Chalmers).

Omrani, A.; Yadav, R.; Link, G.; Jelonnek, J. (2021). A time-reversal imaging algorithm for localization and moisture level detection in the polymer foam in an industrial microwave drying system. AMPERE 2021 Proceedings, Chalmers University of Technology (Chalmers).

Camacho, J. N. Hernandez; Link, G.; Schubert, M.; Hampel, U. (2021). Modeling of the Effective Permittivity of Open-Cell Ceramic Foams Inspired by Platonic Solids. Materials, 14 (23), Article no: 7446. doi:10.3390/ma14237446

Omrani, A.; Yadav, R.; Link, G.; Lähivaara, T.; Vauhkonen, M.; Jelonnek, J. (2021). An electromagnetic time-reversal imaging algorithm for moisture detection in polymer foam in an industrial microwave drying system. Sensors, 21 (21), Art.Nr. 7409. doi:10.3390/s21217409

Li, N.; Link, G.; Ma, J.; Jelonnek, J. (2021). LiDAR Based Multi-Robot Cooperation for the 3D Printing of Continuous Carbon Fiber Reinforced Composite Structures. Advances in Manufacturing Techno – Proceedings of the 18th International Conference on Manufacturing Research, incorporating the 35th National Conference on Manufacturing Research, 7–10 September 2021, University of Derby, Derby, UK. Ed.: M. Shafik, 125–132, IOS Press. doi:10.3233/ATDE210024

Hosseini, M.; Kaasinen, A.; Shoorehdeli, M. A.; Link, G.; Lähivaara, T.; Vauhkonen, M. (2021). System identification of conveyor belt microwave drying process of polymer foams using electrical capacitance tomography. Sensors, 21 (21), 7170. doi:10.3390/s21217170

Yadav, R.; Omrani, A.; Link, G.; Vauhkonen, M.; Lähivaara, T. (2021). Microwave tomography using neural networks for its application in an industrial microwave drying system. Sensors, 21 (20), 6919. doi:10.3390/s21206919

Zhang, Y.; Omrani, A.; Yadav, R.; Fjeld, M. (2021). Supporting visualization analysis in industrial process tomography by using augmented reality—A case study of an industrial microwave drying system. Sensors, 21 (19), 6515. doi:10.3390/s21196515

Li, N.; Link, G.; Engler, M.; Jelonnek, J. (2021). Small-Size Coaxial Resonant Applicator for Microwave Heating Assisted Additive Manufacturing. IEEE transactions on microwave theory and techniques, 69 (11), 4631–4638. doi:10.1109/TMTT.2021.3105431

Li, N.; Link, G.; Jelonnek, J.; Morais, M. V. C.; Henning, F. (2021). Microwave additive manufacturing of continuous carbon fibers reinforced thermoplastic composites: Characterization, analysis, and properties. Additive Manufacturing, 44, Art.-Nr.: 102035. doi:10.1016/j.addma.2021.102035

Hosseini, M.; Kaasinen, A.; Link, G.; Lahivaara, T.; Vauhkonen, M. (2021). Electrical Capacitance Tomography to Measure Moisture Distribution of Polymer Foam in a Microwave Drying Process. IEEE Sensors Journal, 21 (16), 18101–18114. doi:10.1109/JSEN.2021.3085762

Omrani, A.; Yadav, R.; Link, G.; Vauhkonen, M.; Lahivaara, T.; Jelonnek, J. (2021). A Combined Microwave Imaging Algorithm for Localization and Moisture Level Estimation in Multilayered Media. 2021 15th European Conference on Antennas and Propagation (EuCAP), 22-26 March 2021, Düsseldorf, Germany, Institute of Electrical and Electronics Engineers (IEEE). doi:10.23919/EuCAP51087.2021.9411327

Yadav, R.; Omrani, A.; Vauhkonen, M.; Link, G.; Lähivaara, T. (2021). Microwave Tomography for Moisture Level Estimation Using Bayesian Framework. 2021 15th European Conference on Antennas and Propagation (EuCAP), Düsseldorf, 22. - 26. März 2021, Düsseldorf, Institute of Electrical and Electronics Engineers (IEEE). doi:10.23919/EuCAP51087.2021.9411109

Omrani, A.; Link, G.; Jelonnek, J. (2021). A Multistatic Uniform Diffraction Tomographic Algorithm for Real-Time Moisture Detection. 2020 IEEE Asia-Pacific Microwave Conference (APMC), 437–439, Institute of Electrical and Electronics Engineers (IEEE). doi:10.1109/APMC47863.2020.9331603

Appendix

Equipment, Teaching Activities and Staff

IHM is equipped with a workstation cluster and a large number of experimental installations: KEA, KEA-ZAR, three GESA machines, eight COSTA devices, one abrasion and one erosion teststand, a gyrotron test facility including a microwave-tight measurement chamber and two teststands for gyrotrons, one compact technology gyrotron (30 GHz, 15 kW CW), several 2.45 GHz applicators of the HEPHAISTOS series, one 0,915 GHz, 60 kW magnetron system, one 5.8 GHz, 3 kW klystron installation and a low power microwave laboratory with several vectorial network analysers, a plasma laboratory with 2,45 GHz atmospheric plasma sources up to 6 kW and a laboratory for microwave assisted 3D printing of continuous fibre reinforced filaments.

The project FULGOR, targeting for a renewal of the KIT gyrotron teststand is progressing. In 2013, an agreement on the project structure including the involvement of the KIT project and quality management has been achieved. The final start of the procurement of the equipment was in 2014. The start of operation is expected by end of 2021.

Prof. John Jelonnek has continued to teach the lecture course entitled “High Power Microwave Technologies (Hochleistungsmikrowellentechnik)” for Master students at KIT. Prof. Georg Müller has continued to teach the lecture on “Pulsed Power Technologies and Applications” at KIT. Dr. Gerd Gantenbein has been teaching the part “heating and current drive” of the lecture “Fusionstechnologie B” by Prof. R. Stieglitz, IFRT. Dr.-Ing. Martin Sack hold the lecture course “Elektronische Systeme und EMV” at KIT.

At the turn of the year 2021/2022 the total staff with regular positions amounted to 39 (20 academic staff members, 10 engineers and 8 technical staff member and others).

In addition 13 academic staff members, 2 engineer and 1 technical staff members (and others) were financed by acquired third party budget.

In course of 2021, 4 guest scientists, 13 PhD students (1 of KIT-Campus South, 11 of KIT-Campus North, 1 Scholarship), 3 DHBW students, 4 trainees in the mechanical and electronics workshops worked in the IHM. 4 Master students, 3 Bachelor students, 14 student assistants and 3 Research internships were supervised at IHM during 2021.

Strategical Events, Scientific Honors and Awards

M.SC. Damaris Krust won 2nd place with her thesis "Microalgae on the Electric Chair" at the Energy Campus 2021.

Longlasting Co-operations with Industries, Universities and Research Institutes

- Basics of the interaction between electrical fields and cells (Bioelectrics) in the frame of the International Bioelectrics Consortium with Old Dominion University Norfolk, USA; Kumamoto University, Japan; University of Missouri Columbia, USA; Institute Gustave-Roussy and University of Paris XI, Villejuif, France; University of Toulouse, Toulouse, France, Leibniz Institute for Plasma Science and Technology, Greifswald, Germany.

- Cooperation on the technological development of a sodium liquid metal battery as an electrical storage device with DLR and the Huazhong University of Science and Technology – HUST in Wuhan (China).

- Development of protection against corrosion in liquid metal cooled reactor systems in the following EU-Projectes: GETMAT, IL TROVATORE (Partner: CEA, ENEA, SCK-CEN, CIEMAT).

- Development of large area pulsed electron beam devices in collaboration with the Efremov Institute, St. Petersburg, Russia.

- Development of advanced 1.5 MW gyrotrons, gyrotron for multi-purpose operation and new gyrotron control techniques for the ECRH System at the stellarator Wendelstein W7-X in collaboration with the Max-Planck-Institute for Plasmaphysics (IPP) Greifswald.

- Development of the European gyrotrons for ITER in the frame of the European GYrotron Consortium (EGYC) and coordinated by Fusion for Energy (F4E). The other members of the Consortium are EPFL Lausanne, Switzerland, CNR Milano, Italy, ENEA, Frascati, Italy, HELLAS-Assoc. EURATOM (NTUA/NKUA Athens), Greece. The industrial partner is the microwave tube company Thales Electron Devices (TED) in Paris, France.

- Development of 105 GHz 1 MW gyrotrons for WEST in collaboration with EPFL, Lausanne, Switzerland and CEA, Cadarache, France.

- In frame of EUROfusion, collaboration with EPFL Lausanne, Switzerland, CNR Milano, Italy, ENEA, Frascati, Italy, HELLAS-Assoc. EURATOM (NTUA/NKUA Athens), Greece and the industrial partner Thales Electron Devices (TED), Paris, France to develop gyrotrons for future European DEMOstration fusion power plant. EUROfusion is a consortium of national fusion research institutes located in the European Union, the UK, Switzerland and Ukraine.

- Development of Microwave Systems of the HEPHAISTOS Series for materials processing with microwaves with the Company Vötsch Industrietechnik GmbH, Reiskirchen.